

Development and Application of Mixed Quantum-Classical Non-adiabatic Molecular Dynamics Techniques for Charge Transport in Organic Semiconductors

Matt Ellis

A dissertation submitted in partial fulfillment
of the requirements for the degree of
Doctor of Philosophy
of
University College London.

Department of Physics and Astronomy
University College London

April 15, 2021

I, Matt Ellis, confirm that the work presented in this thesis is my own. Where information has been derived from other sources, I confirm that this has been indicated in the work.

Abstract

My research is about stuff.

It begins with a study of some stuff, and then some other stuff and things.

There is a 300-word limit on your abstract.

Acknowledgements

Acknowledge all the things!

Contents

1	Introduction	15
1.1	Charge Transport in Organic Semiconductors	15
1.1.1	Organic Semiconductors	15
1.2	Atomistic Simulations of Nonadiabatic Processes	16
1.2.1	Surface Hopping and Ehrenfest Dynamics	17
1.3	Exact Factorisation	20
1.4	Approximations leading to CTMQC	21
1.4.1	Classical Nuclei	22
1.4.2	Neglect the ENCO in the TDPES	22
1.4.3	Derivative of the Adiabatic Coefficients	22
1.4.4	Gaussian Nuclear Wavepackets	23
1.4.5	Separating the Effects of Decoherence and NACVs	23
1.5	The CTMQC equations	23
1.5.1	Adiabatic Basis	23
1.6	Calculating the Quantum Momentum	25
2	CTMQC applied to the Tully Models	27
2.1	Testing My Implementation	29
2.1.1	Comparisons To Literature	30
2.1.2	Ehrenfest	30
2.1.3	CTMQC	32
2.1.4	Norm Conservation	34
2.1.5	Mathematical Tests	38

Contents	6
2.1.6 Energy Conservation	40
2.2 Calculation of $\mathcal{Q}_{lk,v}^{(I)}$	41
2.2.1 Constant Values of σ	42
2.2.2 Dynamic $\sigma_v^{(I)}(t)$ calculation	43
 3 CTMQC applied to molecular systems	 44
3.1 Basis Transformation	45
3.1.1 Coefficients	46
3.1.2 Forces	48
3.2 Testing the diabatic propagator	48
3.3 Simulating Molecular Systems	49
3.3.1 Varying the number of replicas	51
3.3.2 Varying the timestep	51
3.3.3 Removing Center of Mass Motion	52
3.3.4 Varying the gaussian width (σ) parameter	52
3.3.5 Turning off the quantum momentum addition to the force term . .	52
3.3.6 Renormalisation	52
3.4 Conclusions	52
 4 Extending surface hopping for larger systems	 55
4.1 Code Optimisations	55
 5 Charge transfer in amorphous systems	 56
5.1 Creating Amorphous Pentacene	57
5.2 Structure of the quenched simulations	58
5.2.1 Final Structure Snapshots	58
5.2.2 Molecular Packing	59
5.2.3 Mass Density	61
5.2.4 Angular Distribution	62
5.2.5 Radial Distribution Function	63
5.2.6 Orientational Order Parameter	64
5.3 Charge Transfer Properties	66

Contents	7
5.3.1 Global Couplings	66
5.3.2 Coupling Graphs	67
5.3.3 Hole Mobilities	69
5.3.4 Simulation Set up	69
5.3.5 100ns System	71
5.3.6 10ns System	73
5.4 Mobilities	73
5.4.1 Molecular Dynamics without Partial Charges	74
 6 Extending surface hopping with electrostatics	 75
6.1 Electrostatics interaction within FOB-SH	75
 7 General conclusions	 77
 Appendices	 78
A Tully Model Paramters	78
A.1 Model 1 -Single Avoided Crossing	78
A.2 Model 2 -Dual Avoided Crossing	79
A.3 Model 3 -Extended Coupling	79
A.4 Model 4 -Dual Arch	80
 B Wigner Distribution Derivation	 81
C $\mathbf{R}_{lk,v}$ Alternatives	83
C.1 $\mathbf{R}_{lk,v}$ Extrapolation	83
C.2 Alternative Quantum Momentum Intercept	83
 D Rabi Oscillation	 85
E Norm Conservation in CTMQC and Ehrenfest	87
F Dynamic σ Calculation	89

Contents	8
G Basis Transformation	90
G.1 Forces	91
H Adiabatic State Initialisation	93
I Analytic Overlap Method	95
J Colophon	96
Bibliography	97

List of Figures

1.1	An example of a typical Ehrenfest simulation near an avoided crossing. The black lines represent the adiabatic potential energy surface due to the ground (PES 1) and excited (PES 2) state. The red line represents the population weighted average potential the nuclei travel on.	17
1.2	An example of a typical Surface Hopping simulation near an avoided crossing. The black lines represent the adiabatic potential energy surface due to the ground (PES 1) and excited (PES 2) state. The red line represents the discontinuous effective potential the nuclei travel on.	19
1.3	A demonstration of how the TDPES can cause the splitting of the nuclear wavepacket in non-adiabatic regions. The red line represents the TDPES and the blue is the nuclear density. Figure adapted from Agostini, 15 ¹ . .	21
2.1	Adiabatic potential energy surfaces (orange and blue) and element 1, 2 of the nonadiabatic coupling vector (black) for the 4 model systems. For parameters see appendix A.	28
2.2	A comparison of my implementation of Ehrenfest (for 4 model Hamiltonians) and results from the literature. The black dashed lines show my data (ground state ad pops), the orange dashed lines are data from Agostini, 16 ² and the blue solid lines are from Gossel, 18 ³ . The figures are labelled with their model number, whether the initial momentum was high or low and whether the populations or coherence indicator was plotted.	31

2.3	Comparison of transmission probabilities through the region of high nonadiabatic coupling on the ground state. Tully model 1 is shown in the top-left, Tully model 2 is shown in the top-right and Tully model 3 is shown in the bottom-left.	32
2.4	A comparison of my implementation of full CTMQC (for 4 model Hamiltonians) and results from the literature. The black dashed lines show my CTMQC data (ground state ad pops), the orange dashed lines are data from Agostini, 16 ² and the blue solid lines are from Gossel, 18 ³ . The solid green line shows data from exact quantum mechanical simulations given in Gossel, 18. The figures are labelled with their model number, whether the initial momentum was high or low and whether the populations or coherence indicator was plotted.	33
2.5	The norm conservation averaged over all replicas for Ehrenfest simulations with various electronic timesteps for each Tully model using a initial high momenta.	34
2.6	The norm conservation when using standard CTMQC as outlined in the literature for each of the Tully models. These simulations were ran with a high initial momentum. The red markers show data points and vertical bars show error bars associated with each point.	35
2.7	As the denominator of the $\mathbf{R}_{lk,v}$ term approaches zero (bottom panel) the full $\mathbf{R}_{lk,v}$ term (2 nd to bottom panel) can approach infinity which propagates through the $\mathcal{Q}_{lk,v}^{(I)}$ term (2 nd to top panel) causing discontinuities and norm drift in the populations (top panel). The grey vertical bar denotes the region the denominator approaches 0. The thin solid red lines in the top panel show the norm drift for individual replicas.	36
2.8	Norm conservation in CTMQC after applying a divergence correction to the $\mathbf{R}_{lk,v}$ term. RI0 refers to method 3, Extrap DC refers to method 2 and Ehren DC refers to method 1. No DC Corr shows the population norm without any corrections applied.	37

2.9	The conserved quantity given in equation (2.5). Each color represents data outputted by a simulation using a different model (specified in the legend). Each time-series is plotted with a translucent color meaning each model's data can be seen at once.	39
2.10	Energy conservation values for various nuclear timesteps for the high momentum case of each Tully model.	41
2.11	4 high momenta cases of the Tully models with a varying σ parameter used in the calculation of the quantum momentum.	43
3.1	The 4 Tully models simulated using propagating the equations within a diabatic and adiabatic basis. The green line shows results from the diabatic propagator and the red line shows results from the adiabatic propagator. .	49
3.2	An example Ethylene dimer used to test the CTMQC implementation. The right panel shows the positions of just 1 replica. The left panel shows the positions of all replica with the replica shown on the right highlighted in red.	50
3.3	The norm of the adiabatic expansion coefficients. Thin red lines show the norm for each trajectory and the thick green line shows the average over all trajectories.	51
5.1	An example of the herringbone packing typically found in Pentacene crystals	56
5.2	The melt-quench scheme used to create amorphous pentacene systems. Blue boxes indicate steps using an NPT ensemble, orange boxes indicate use of a NVT ensemble.	57
5.3	The final snapshot of each quenching simulation visualised in VMD ⁴ and rendered with Tachyon ⁵ . Snapshots are ordered by quenching time i.e. a) is the 0ns quench, b) is the 1ns quench and so on.	59

5.4	The 100ns quenched structure with different clusters shown with different colours. A bird's eye view of the green cluster has been shown on the left to demonstrate the herringbone packing within each cluster/layer. The far-right image labelled 'Crystal' is a snapshot of a crystal plane after a short MD equilibration.	60
5.5	A slice from the 0ns quenched structure with selected clusters of herringbone-like packing highlighted.	60
5.6	A time series of the density of the quenched structures. The black line shows the experimental mass density of crystal pentacene.	61
5.7	The angular distribution for the 4 different quench times is shown above. The brown and purple lines are from a perfect crystal before and after a short MD run. The others are after the various melt-quench simulations. On the right is a schematic showing which angles are referenced in each plot.	62
5.8	The carbon-carbon radial distribution function for 4 different quenching times and a crystal before and after 50ps of MD. The quenches (0, 1, 10 and 100ns) are shown in blue, orange, green and red respectively. The crystal data are shown in purple and brown.	63
5.9	The change in the orientational order parameter (OOP) with respect to the quenching time. The blue data represents the values for the long axis and the orange data represents the short axis values. The horizontal lines show the theoretical value for a perfect crystal.	64
5.10	The global coupling distribution for each of the quenched structures (in blue, orange, green and red) and 1 structure after a 10ns quench without using electrostatics (purple line). The black dashed lines represent the maximum coupling within a perfect pentacene crystal.	66

5.11 A representative network of electronic coupling that each quenched structure has formed. Each structure is labelled by the quench time (e.g. 0ns, 1ns, 10ns, 100ns) or Crystal for a crystal after a short MD equilibration. Coupling strengths are categorised as high (red), medium (green) and low (blue). The definitions of the categories are given in the legend in the bottom right corner.	67
5.12 The restraint set up for 1 molecule. Each coloured zig-zag shows the atoms that are restrained.	69
5.13 Panel a) shows a system chosen to run surface hopping on, molecules in gray are fixed in place blue molecules show the active region. Panel b) shows every substructure chosen in the 0ns quenched structure.	71
5.14 The 100ns quenched structure clustered by layer. Each different colour represents a different cluster, labelled with the numbers around the edge of the structure.	72
5.15 The clusters chosen to run surface hopping simulations on. The coloured clusters each represent a different structure on which surface hopping was ran.	73
C.1 A crude demonstration of the principle behind the smoothing procedure in switching between intercepts. The black line shows an intercept begin to diverge and the alternative intercept is shown in purple. As the step is incremented the amount of the alternative intercept that makes up the effective intercept is increased until only 1 intercept is used.	84
D.1 Rabi oscillation occurring within a Ethylene trimer system. Dotted lines were calculated using equation (D.2), solid lines were calculated using the RK4 propagator within the CTMQC section of the CP2K code. The norm is shown on the top as a cyan line and the x axis shows the timestep in seconds.	86

List of Tables

5.1 The change in the number of high coupling fragments, and the mean and standard deviation of their size, found in each structure as the quenching time was varied.	68
---	----

Chapter 1

Introduction

1.1 Charge Transport in Organic Semiconductors

1.1.1 Organic Semiconductors

Conductive polymers were first discovered in 1977 by Shirakawa et al^{6,7} for which they were awarded the Nobel prize in Chemistry. Recently these materials have become ubiquitous in many technologies, such as in organic photovoltaic cells⁸, organic field-effect transistors (OFET)⁹ and organic light-emitting diodes (OLED)¹⁰. While the other two technologies lag behind their inorganic counterparts, uptake of OLED screens is becoming ubiquitous -especially in the smartphone and television market due to their flexibility, better colour representation and lower energy consumption than standard backlit LCD displays. OLEDs have also found uses in lighting with their efficiency rivalling that of fluorescent tubes^{11,12}. Although, industry has made large strides in fabricating and using these materials the exact nature of the charge transport is still poorly understood. Traditional theories (such as hopping and band transport) aren't applicable to many relevant materials^{13–17} as charge transfer dynamics lies in an intermediate region where the polaron is neither fully localised or delocalised. This is due to crystals typically being formed of organic molecules weakly held together by Van der Waals (VDW) forces rather than strong covalent bonds. This allows molecules to fluctuate about their lattice sites and introduces a disorder that doesn't appear in inorganic crystals.

In order to properly quantify the performance of organic semiconductors a key prop-

erty is the charge carrier mobility. Typically, charge carrier mobilities in ‘good’ organic semiconductors (OSCs) fall between $1\text{-}10 \text{ cm}^2\text{V}^{-1}\text{s}^{-1}$ ¹⁸. Though higher mobilities, in pure crystals such as Rubrene, have been recorded in the range $15\text{-}20+ \text{ cm}^2\text{V}^{-1}\text{s}^{-1}$ ^{19,20}. This is beyond the range of hopping model validity ($\sim 1 \text{ cm}^2\text{V}^{-1}\text{s}^{-1}$) and below that of band theory ($> 50 \text{ cm}^2\text{V}^{-1}\text{s}^{-1}$)¹⁷. In this intermediate regime the charge carriers are typically not completely delocalised at the valence band edges (band regime) or localised to a single site/molecule (hopping regime) but delocalised over a few/tens of molecules²¹. Without any analytic approaches currently being valid in this regime many atomistic computational approaches have been developed to investigate the underlying charge transport mechanisms²².

1.2 Atomistic Simulations of Nonadiabatic Processes

In simulating processes involving electronic transfers a key approximation used in conventional molecular dynamics (MD) breaks down. That is the Born-Oppenheimer or adiabatic approximation²³. This approximation, relied upon for almost a century²⁴, hinges on the fact that nuclei are much more massive than electrons and are approximately stationary with respect to electron movement²⁵. This results in nuclear evolution that is governed by a single, adiabatic, potential energy surface. However, in many interesting processes, such as the proton coupled electron transfer in photosynthesis and respiration^{26–28}, non-radiative decay and photochemical processes, electronic transitions between adiabatic potential energy surfaces occur²⁹. Simulating these processes requires non-adiabatic molecular dynamics (NAMD) techniques to be developed, to correctly capture dynamical properties.

There have been many techniques proposed for use in NAMD such as the quantum classical Louiville equation³⁰, multiple spawning³¹ or nonadiabatic Bohmian dynamics³². However, two of the most popular are trajectory surface hopping³³ and mean-field approaches³⁴. This is probably due to their relative simplicity to implement, efficiency for

large systems and proven efficacy in a wide variety of situations³⁵. In these approaches the general aim is to treat as much of the system as possible with (computationally cheaper) classical mechanics. While handling all necessary parts with quantum mechanics³⁶. In Surface Hopping, Ehrenfest and Coupled-Trajectory Mixed Quantum-Classical molecular dynamics (CTMQC) one treats the nuclear subsystem classically and the electronic one quantum mechanically. The nuclei are normally propagated using a velocity verlet algorithm according to Newton's laws and electrons using a fourth order Runge Kutta algorithm according to the time-dependent Schrödinger equation. The wavefunction is normally expanded as a linear combination of adiabatic or diabatic states. The nuclei and electrons can also interact. Taking account of this interaction is where these techniques differ. No one technique is perfect, the issues for surface hopping and Ehrenfest are well documented and have been discussed in detail³⁷⁻⁴¹. CTMQC is a fairly new technique and its issues are still mostly unknown. In this document I will discuss CTMQC in depth and present results from my own implementation of it as well as presenting its drawbacks. I will also compare these results to Ehrenfest and Trajectory Surface Hopping (TSH).

1.2.1 Surface Hopping and Ehrenfest Dynamics

An important technique in the field of mixed quantum classical nonadiabatic molecular dynamics is Ehrenfest dynamics. Assuming we treat the nuclei classically the Ehrenfest equations can be rigorously derived from the electronic Schrödinger equation. This is done by assuming that the nuclei's motion is provided by a single population weighted average potential energy surface. This average is taken from the adiabatic potential energy surfaces (eigenvalues of the Hamiltonian) where weights are provided by the populations of each adiabatic state. This effective potential energy surface is shown in fig 1.1. In this way the electronic

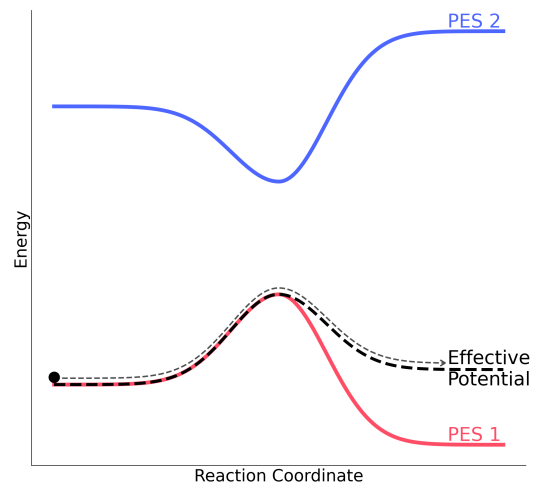


Figure 1.1: An example of a typical Ehrenfest simulation near an avoided crossing. The black lines represent the adiabatic potential energy surface due to the ground (PES 1) and excited (PES 2) state. The red line represents the population weighted average potential the nuclei travel on.

subsystem influences the propagation of the nuclei. The propagation of the forces and the electrons are controlled by equations (1.1) and (1.2).

$$F_v^{Ehren} = \sum_i^{N_{st}} |C_i|^2 \nabla_v E_i + \sum_{i,j}^{N_{st}} C_i^* C_j (E_j - E_i) \mathbf{d}_{i,j,v} \quad (1.1)$$

$$\hbar \vec{C}_m = C_m E_m - i \hbar \sum_n^{N_{st}} C_n d_{mn}^{ad} \quad (1.2)$$

In the above equations C_i is the adiabatic expansion coefficient for state i , E_m is the energy of adiabatic state m , $\mathbf{d}_{mn,v}^{ad}$ is the nonadiabatic coupling (in the adiabatic basis) between states m and n for atom v . The d_{mn}^{ad} are the nonadiabatic coupling elements expressed in the adiabatic basis. Although the Ehrenfest method has been applied with success in many systems^{42–44} it has a number of key shortcomings. Namely, its inability to capture the branching of the nuclear wavefunction as propagation occurs on only a single potential energy surface and its poor account of the decoherence of the electronic and nuclear subsystem after an avoided crossing. Ehrenfest also violates detailed balance by populating all adiabatic states evenly^{23,45}. In the limit of infinite states this results in infinite electronic temperature⁴⁶. Possibly the most popular technique in NAMD is trajectory surface hopping. In trajectory surface hopping the shape of the potential energy surface is determined by a series of discrete stochastic hops between adiabatic potential energy surfaces⁴⁵. See fig 1.2. The probability of these hops is determined by the non-adiabatic coupling between states. A swarm of trajectories are used and the probability a hop (non-adiabatic coupling) determines how many of these change state. The nuclear dynamics are dictated by the shape of the energy surface they are travelling on. This method can capture the branching of nuclear wavepacket unlike Ehrenfest. However, it still suffers from a number of issues. The original ‘fewest switches surface hopping’ proposed by John Tully suffered from bad overcoherence of the nuclear and electronic subsystems. That is the electronic and nuclear motion was coupled long after the region of high non-adiabatic coupling (crossing region). The fact that the hops are instant leads to discontinuities and methods need

to be implemented to fix these such as velocity re-scaling. Finally, perhaps the most important shortcoming is that this technique has not been derived from first principles and cannot be guaranteed to work generally. These problems have lead to a number of other techniques being developed. One of these, CTMQC, will be studied in this thesis and is the semi-classical limit of the exact factorisation of the time-dependent Schrödinger equation.

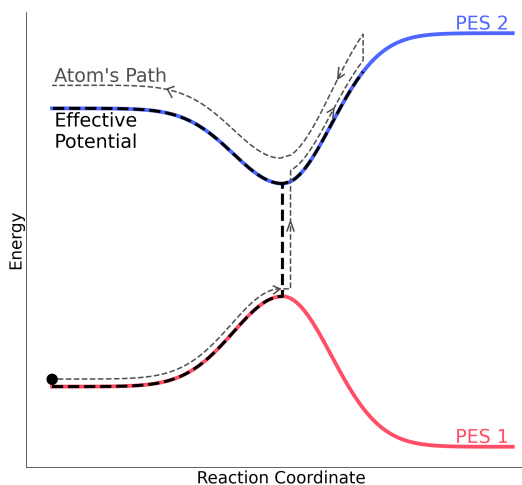


Figure 1.2: An example of a typical Surface Hopping simulation near an avoided crossing. The black lines represent the adiabatic potential energy surface due to the ground (PES 1) and excited (PES 2) state. The red line represents the discontinuous effective potential the nuclei travel on.

1.3 Exact Factorisation

Exact factorisation⁴⁷ involves separating the total molecular wavefunction into a nuclear component and electronic component. Where the electronic component is parametrically dependent on the nuclear coordinates, \mathbf{R} . This is shown below in eq (1.3) where χ is the nuclear wavefunction and Φ is the electronic one.

$$\Psi(\mathbf{R}, \mathbf{r}, t) = \Phi_{\mathbf{R}}(\mathbf{r}, t)\chi(\mathbf{R}, t) \quad (1.3)$$

In the above equation (and throughout this report) I will denote nuclear coordinates and electronic coordinates R and r respectively. The nuclear and electronic wavefunctions then obey separate, but coupled, time-dependent Schrödinger equations for spatial and temporal evolution. In this report, I will be focussing on the semi-classical limit of these equations, named Coupled-Trajectory Mixed Quantum-Classical Molecular Dynamics (CTMQC), and give results of a combination of this and the AOM method explained in section ??.

The equations for the evolution of the electronic and nuclear wavefunctions in the exact factorisation⁴⁷ are given below:

$$\hbar \frac{\delta}{\delta t} \Phi_{\mathbf{R}}(\mathbf{r}, t) = (\hat{H}_{BO} + \hat{U}_{en}[\Phi_{\mathbf{R}}, \chi] - \varepsilon(\mathbf{R}, t)) \Phi_{\mathbf{R}}(\mathbf{r}, t) \quad (1.4)$$

$$\hbar \frac{\delta}{\delta t} \chi(\mathbf{R}, t) = \left(\sum_{v=1}^{N_n} \frac{[-\hbar \nabla_v + \mathbf{A}_v(\mathbf{R}, t)]^2}{2M_v} + \varepsilon(\mathbf{R}, t) \right) \chi(\mathbf{R}, t) \quad (1.5)$$

Where \hat{H}_{BO} is the Born-Oppenheimer Hamiltonian, that is $\hat{T}_e + \hat{W}_{ee} + \hat{W}_{nn} + \hat{V}_{en}$. Where \hat{T}_e is the electronic kinetic energy operator, $\hat{W}_{ee/nn}$ is the electron-electron/nuclei-nuclei interaction and V_{en} is the electronic-nuclear potential.

The \hat{U}_{en} is an electronic-nuclear coupling operator (ENCO). This is defined as

$$\hat{U}_{en}[\Phi_{\mathbf{R}}, \chi] = \sum_{v=1}^{N_{nuc}} \frac{1}{M_v} \left[\frac{[-\hbar \nabla_v - \mathbf{A}_v(\mathbf{R}, t)]^2}{2} + \left(\frac{-\hbar \nabla_v \chi}{\chi} + \mathbf{A}_v(\mathbf{R}, t) \right) \left(-\hbar \nabla_v - \mathbf{A}_v(\mathbf{R}, t) \right) \right] \quad (1.6)$$

Where the \mathbf{A}_v is a time-dependent vector potential (TDVP), given by $\langle \Phi_{\mathbf{R}}(t) | -\hbar \nabla_v \Phi_{\mathbf{R}} \rangle_{\mathbf{r}}$ and M_v is the mass of nuclei v . Finally $\epsilon(\mathbf{R}, t)$ is a time-dependent scalar potential energy surface (TDPES), given by $\langle \Phi_{\mathbf{R}}(t) | \hat{H}_{BO} + \hat{U}_{en}^{coup} - \hbar \frac{\delta}{\delta t} | \Phi_{\mathbf{R}}(t) \rangle_{\mathbf{r}}$.

The effects of the TDPES, TDVP and the ENCO have been investigated in multiple works^{1,48–51}. The TDPES and TDVP are both responsible for the evolution of the system⁴⁸. The TDPES provides exact classical forces on the nuclei. In fact, an alternative independent-trajectory semi-classical scheme has been investigated using these exact forces¹. This found the TDPES is responsible for the splitting of the nuclear wavepacket in regions of high non-adiabaticity by taking the shape of a step function between the 2 adiabatic potentials. This is demonstrated in figure 1.3, which was adapted from an image in Agostini, 15⁴⁸.

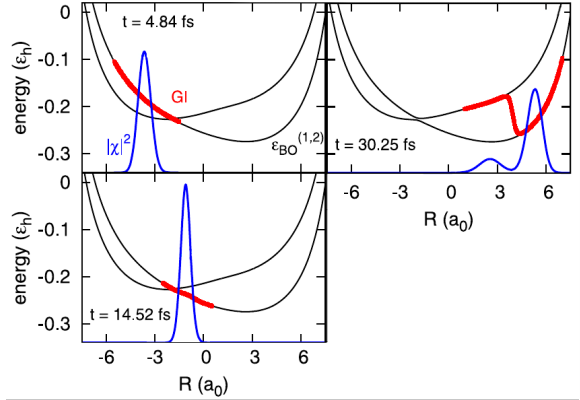


Figure 1.3: A demonstration of how the TDPES can cause the splitting of the nuclear wavepacket in non-adiabatic regions. The red line represents the TDPES and the blue is the nuclear density. Figure adapted from Agostini, 15¹

Finally the electronic-nuclear coupling operator (ENCO) is responsible for other non-adiabatic effects in the system such as electronic nonadiabatic transitions and decoherence⁴⁸.

1.4 Approximations leading to CTMQC

Starting from the exact factorisation equations, 6 approximations have been made to derive the CTMQC equations. These are discussed in detail in Ref.². In the interest of completeness I have summarised them below.

1.4.1 Classical Nuclei

Techniques that include nuclear quantum effects (NQEs); such as multiple spawning³¹, ring-polymer surface hopping⁵² and nonadiabatic Bohmian dynamics^{53,54} although extremely accurate, cannot be applied to hundreds or thousands of molecules, due to their high computational cost. Further, in many systems of interest NQEs are negligible, especially at room temperature. For this reason the classical limit of the nuclear Schrödinger equation (1.5) is taken when deriving the CTMQC equations.

1.4.2 Neglect the ENCO in the TDPES

The electron-nuclei coupling operator is omitted in the expression for the time-dependent potential energy surface. This is justified as the first term ($(-\hbar\nabla_{\mathbf{v}} - \mathbf{A}_{\mathbf{v}}(\mathbf{R}, t))^2$) contains a second order derivative which is expensive to calculate and has a negligible effect compared to the second term in the ENCO⁵⁵. However, the rest of the ENCO is equal to zero when averaged over $\Phi_{\mathbf{R}}(\mathbf{r}, t)$ so it does not contribute to the TDPES.

1.4.3 Derivative of the Adiabatic Coefficients

The derivative of the adiabatic coefficients appears in the electronic evolution equations. However, we can re-write the derivative of the adiabatic coefficients in terms of their modulus and phase:

$$\nabla_{\mathbf{v}} C_l^{(I)}(t) = \left[\underbrace{\frac{\nabla_{\mathbf{v}} |C_l^{(I)}(t)|}{|C_l^{(I)}(t)|}}_{\text{(Term 1)}} + \underbrace{\frac{i}{\hbar} \nabla_{\mathbf{v}} \gamma_l^{(I)}(t)}_{\text{(Term 2)}} \right] C_l^{(I)}(t) \quad (1.7)$$

It has been found that the first term is negligible compared to the second^{1,49,50} so it doesn't need to be calculated and we can remove it. It was also assumed that the NACVs are localised in space meaning that, after some algebra, the spatial derivative of the adiabatic coefficient can be written as:

$$\nabla_{\mathbf{v}} C_l^{(I)}(t) = \frac{i}{\hbar} \nabla_{\mathbf{v}} \gamma_l^{(I)}(t) C_l^{(I)}(t) = -\frac{i}{\hbar} \int^t dt' \nabla_{\mathbf{v}} \epsilon_l^{(I)} C_l^{(I)}(t') = -\frac{i}{\hbar} \mathbf{f}_l^{(I)} C_l^{(I)}(t) \quad (1.8)$$

Where $\epsilon_l^{(I)}$ is the energy of the l^{th} adiabatic potential energy surface for trajectory I, $C_l^{(I)}$ is the adiabatic expansion coefficient for state l and trajectory I. The $\mathbf{f}_l^{(I)}$ is the time-integrated adiabatic force (adiabatic momentum).

1.4.4 Gaussian Nuclear Wavepackets

In order to calculate the quantum momentum -the new term in CTMQC. Knowledge of the nuclear distribution is needed. However, as we treat the nuclei as point particles we need to re-construct the nuclear density from the atomic positions. This is done by smoothing out the atomic positions by placing a gaussian of width σ centered on each atomic position and combining these gaussians to produce the final nuclear density. This introduces an empirical parameter (σ) which will be discussed later in this thesis. It should be noted, the nuclei are still propagated classically, the width parameter is only used in the calculation of the quantum momentum.

1.4.5 Separating the Effects of Decoherence and NACVs

So as to not introduce any population transfer (due to the quantum momentum) when the NACV is zero a fifth approximation has been introduced. Namely the quantum momentum depends on pairs of states -l,k. This enables the separation of the ‘competing’ effects of the NACV and the Quantum Momentum.

1.5 The CTMQC equations

1.5.1 Adiabatic Basis

The equations for the propagation of the classical nuclei and the expansion coefficients in the CTMQC framework in the adiabatic basis are given below:

$$\dot{\mathbf{P}}_v^{(I)} = \underbrace{-\sum_k |C_k^{(I)}|^2 \nabla_v \epsilon_k^{(I)} - \sum_{k,l} C_l^{(I)} C_k^{*(I)} (\epsilon_k^{(I)} - \epsilon_l^{(I)})}_{\text{Ehrenfest}} - \underbrace{\sum_{l,k} |C_l^{(I)}|^2 \left(\sum_{v'=1}^{N_n} \frac{2}{\hbar M_{v'}} \mathcal{Q}_{lk,v'}^{(I)} \cdot \mathbf{f}_{l,v'}^{(I)} \right) \left[|C_k^{(I)}|^2 \mathbf{f}_{k,v}^{(I)} - \mathbf{f}_{l,v}^{(I)} \right]}_{\text{Quantum Momentum}} \quad (1.9)$$

$$\dot{C}_l^{(I)} = \underbrace{-\frac{i}{\hbar} \epsilon_l^{(I)} C_l - \sum_k C_k^{(I)} d_{lk}^{ad(I)}}_{\text{Ehrenfest}} - \underbrace{\sum_{v=1}^{N_n} \sum_k \frac{\mathcal{Q}_{lk,v}^{(I)}}{\hbar M_v} \cdot [\mathbf{f}_{k,v}^{(I)} - \mathbf{f}_{l,v}^{(I)}] |C_k^{(I)}|^2 C_l^{(I)}}_{\text{Quantum Momentum}} \quad (1.10)$$

Where the ϵ_k term is the potential energy on the k^{th} potential energy surface. C_l is the adiabatic expansion coefficient corresponding to the l^{th} state. The sum over k and l indicates a sum over all states, the (I) superscript is a replica index and the v is an atom index. M_v is the nuclear mass and $d_{lk}^{ad(I)}$ represents the non-adiabatic coupling element (in the adiabatic basis) between adiabatic states l and k . The 2 new terms in this scheme not seen in other NAMD methods are the $\mathcal{Q}_{lk,v}^{(I)}$ and the $\mathbf{f}_{k,v}^{(I)}$. These are the quantum momentum and the adiabatic momentum. The adiabatic momentum term is defined in equation (1.8) this keeps a record of the previous forces on each adiabatic state in the system. The quantum momentum term couples the trajectories together (making this a coupled-trajectory scheme). Together the history dependent force and quantum momentum are responsible for the decoherence in the ‘Quantum Momentum’ parts of the above equations³. Notably, although these equations have been derived from the exact factorisation equations separately from Ehrenfest they do contain the Ehrenfest equations within them (marked ‘Ehrenfest’). This scheme can therefore be seen as an Ehrenfest scheme with a correction that captures branching of the nuclear wavefunction and decoherence within it.

We can also see in equation (1.10) if we are in a pure adiabatic state i.e. all population on a single adiabatic state, there is no contribution from the quantum momentum part of the equations. In this scenario the evolution equations become simply Ehrenfest equations. For example, if all the population is localised on a single adiabatic state then the term $|C_k^{(I)}|^2 C_l$ is only non-zero when $l = k$. However, when $l = k$, the term $[\mathbf{f}_{k,v}^{(I)} - \mathbf{f}_{l,v}^{(I)}]$ is zero as $\mathbf{f}_{k,v}^{(I)} = \mathbf{f}_{l,v}^{(I)}$. Therefore, the quantum momentum term can be seen to only kick in when there is a mixing of adiabatic states. In the adiabatic formulation of these equations it is the adiabatic NACV $\mathbf{d}_{lk,v}^{ad,(I)}$ that is responsible for the initial mixing of the

populations from pure adiabatic states.

1.6 Calculating the Quantum Momentum

The technique for calculating the quantum momentum term is outlined in detail in the SI of min, 17⁵⁶. The original equations given in Agostini, 16² present a quantum momentum term without state indices (l,k). This, due to approximations made in the derivation of CTMQC, results in population transfer even when the non-adiabatic couplings between states are zero. Therefore, Agostini et al enforced this condition with the pair-wise state dependence on the quantum momentum. The quantum momentum is defined in equation (1.11) as:

$$\mathcal{Q}_v^{(I)} = \frac{-\hbar \nabla_v |\chi^{(I)}|}{|\chi^{(I)}|} \frac{-\hbar \nabla_v |\chi^{(I)}|^2}{2|\chi^{(I)}|^2} \quad (1.11)$$

In order to reconstruct the nuclear density, Gaussian distributions are used as in equation (1.12) below:

$$|\chi^{(I)}(t)|^2 = \frac{1}{N_{tr}} \sum_{J=1}^{N_{tr}} \prod_{v=1}^{N_n} g_{\sigma_v^{(J)}(t)} \left(\mathbf{R}_v^{(I)}(t) - \mathbf{R}_v^{(J)}(t) \right) \quad (1.12)$$

Where, N_{tr} is the number of trajectories, N_n is the number of atoms, $\sigma_v^{(J)}(t)$ is a time-dependent width parameter for each gaussian g and $\mathbf{R}_v^{(J)}$ represents the atomic position of atom v on trajectory J .

This results in a linear expression for the quantum momentum. The full details of the derivation are given in the supplementary information of Min, 17⁵⁶. The resulting linear expression for the quantum momentum is given below:

$$\mathcal{Q}_{lk,v}^{(I)} = \alpha_v^{(I)} \mathbf{R}_v^{(I)} - \mathbf{R}_{lk,v} \quad (1.13)$$

Where $\mathbf{R}_v^{(I)}$ are the nuclear coordinates on trajectory I on atom v . The $\alpha_v^{(I)}$ term is a weighted average over trajectories of the product of the gaussian's assigned to each atomic

coordinate, i.e:

$$\alpha_v^{(I)} = \sum_J^{N_{tr}} \frac{\hbar \prod_{v'} g_{\sigma_{v'}^{(J)}(t)} \left(\mathbf{R}_{v'}^{(I)}(t) - \mathbf{R}_{v'}^{(J)}(t) \right)}{2\sigma_v^{(J)}(t)^2 \sum_K^{N_{tr}} \prod_{v'} g_{\sigma_{v'}^{(K)}(t)} \left(\mathbf{R}_{v'}^{(I)}(t) - \mathbf{R}_{v'}^{(K)}(t) \right)} \quad (1.14)$$

Along with the $\mathbf{R}_{lk,v}$ term the $\alpha_v^{(I)}$ performs the job of coupling the trajectories together. The $\mathbf{R}_{lk,v}$ term also given in the SI of Min, 17⁵⁶ is defined for each Cartesian dimension as:

$$R_{lk,v} = \sum_I^{N_{tr}} R_v^{(I)}(t) \alpha_v^{(I)}(t) \frac{|C_k^{(I)}(t)|^2 |C_l^{(I)}(t)|^2 (f_{k,v}^{(I)}(t) - f_{l,v}^{(I)}(t))}{\sum_J |C_k^{(J)}(t)|^2 |C_l^{(J)}(t)|^2 (f_{k,v}^{(J)}(t) - f_{l,v}^{(J)}(t))} \quad (1.15)$$

Where the bold notation for vectors has been replaced by normal font. This means that this equation applies to each Cartesian dimension independently. Further, in this expression $R_{lk,v}$ is symmetric, $R_{lk} = R_{kl}$ meaning that $Q_{lk} = Q_{kl}$. It is also undefined on the diagonals as the denominator is 0, diagonal values are therefore set to 0. At first sight, the R_{lk} term seems to be another weighted average. However, this isn't quite the case as the denominator can be negative. This causes equation (1.15) to be very sensitive to errors in the calculation of the denominator of this fraction. Any inaccuracies can lead to the denominator approaching zero faster than the numerator causing large spikes in the quantum momentum term. This will be discussed in greater detail in the following chapters.

Chapter 2

CTMQC applied to the Tully Models

The Tully models, first proposed by John Tully in 1990⁵⁷, are a collection of simple 1 dimensional model systems. They were designed to be simple enough to obtain accurate quantum results to benchmark new nonadiabatic molecular dynamics (NAMD) methods against. Originally there were 3, 1 dimensional, 1 atom models. However, in this work an extra model has been introduced with parameters taken from Gossel, 18³. This is to allow a full comparison of my implementation of CTMQC with the literature. In this chapter my implementation of CTMQC will be tested using these model systems and by comparing my results with those in the literature.

In each of the Tully models the (diabatic) Hamiltonian is a function of nuclear positions and is a 2×2 matrix that takes the form:

$$\hat{H} = \frac{\hat{P}^2}{2M} + \begin{pmatrix} H_{11}(\mathbf{R}) & H_{12}(\mathbf{R}) \\ H_{21}(\mathbf{R}) & H_{22}(\mathbf{R}) \end{pmatrix} \quad (2.1)$$

The nuclear mass has been set to 2000 a.u.. This was set to be very close to the proton's mass of 1836 a.u. so we can expect significant quantum effects that classical theory couldn't replicate. The values of the Hamiltonian matrix elements are set to produce systems that resemble common features in a typical nonadiabatic simulation such as avoided crossings and regions of extended coupling. The parameters used in each systems' Hamiltonian where taken from Gossel, 18³ in order to compare the 2 implementations. These can be found in appendix A.

In order to propagate dynamics in the adiabatic basis we need to calculate various quantities from the hamiltonian at each timestep. These are, for Ehrenfest, the (adiabatic) nonadiabatic coupling vector ($\mathbf{d}_{lk}^{(I)}$) and the adiabatic energies ($E_l^{(I)}$). In the full CTMQC simulations we must also calculate the adiabatic momentum term $\mathbf{f}_l^{(I)}$ from the Hamiltonian. The adiabatic energies are the eigenvalues of the Hamiltonian. The adiabatic NACV can be calculated via a finite difference method and equation (2.2) below.

$$\mathbf{d}_{lk}^{(I)} = \langle \psi_l^{(I)} | \nabla \psi_k^{(I)} \rangle \quad (2.2)$$

Where $\psi_l^{(I)}$ is the adiabatic electronic basis function for adiabatic state l. This is given by the eigenvector of the Hamiltonian, on replica I, corresponding to state l. Illustrations of these 2 properties can be found below in fig 2.1 for each of the 4 models systems.

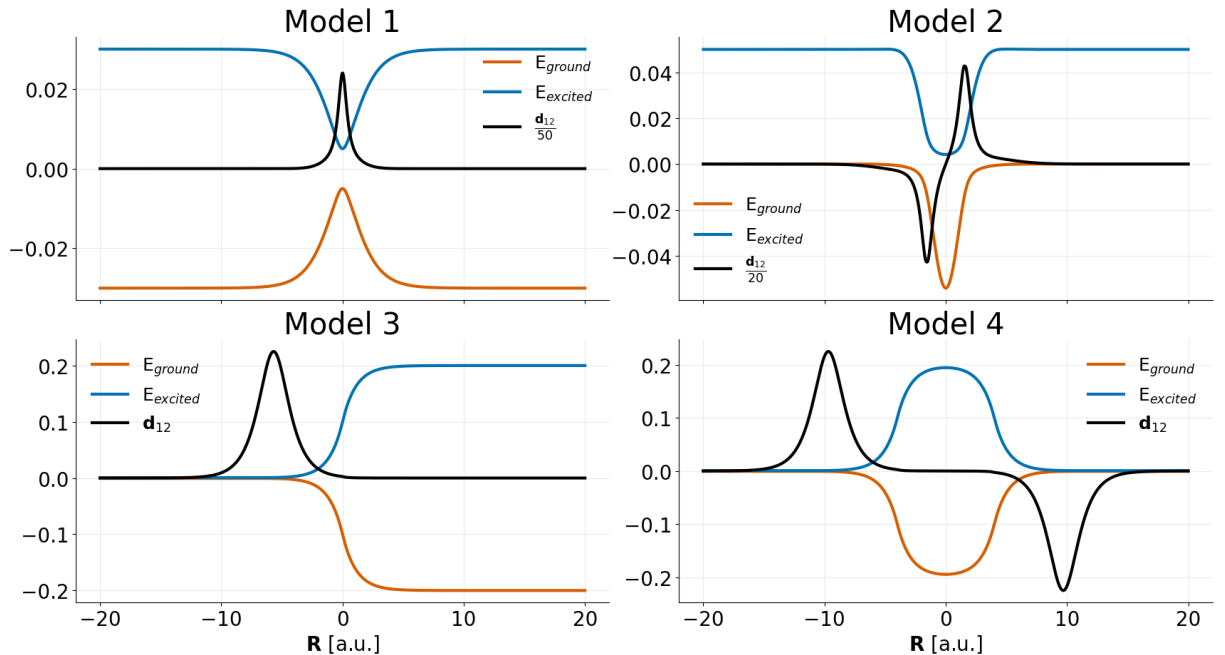


Figure 2.1: Adiabatic potential energy surfaces (orange and blue) and element 1, 2 of the nonadiabatic coupling vector (black) for the 4 model systems. For parameters see appendix A.

In order to initialise the simulations coordinates and velocities were sampled from the Wigner phase-space distribution of a gaussian nuclear wavepackets given by equation (2.3). A derivation of this can be found in appendix B. The nuclear positions/velocities were then propagated using a velocity verlet algorithm and the adiabatic expansion coefficients were propagated using a 4th order Runge-Kutta method.

$$\chi(R, 0) = \frac{1}{(\pi\mu^2)^{\frac{1}{4}}} e^{-\frac{(R-R_0)^2}{2\mu^2} + ik_0(R-R_0)} \quad (2.3)$$

The adiabatic coefficients were initialised purely on the ground state and the initial width of the nuclear wavepacket was set to $\mu = \sqrt{2}$ bohr. 2 values of initial momenta k_0 were chosen for each model, 1 low value and another higher one. Full details of all input parameters can be found in appendix A. I have implemented a serial version of CTMQC acting on Tully's toy model systems and real molecular systems using couplings derived from the analytic overlap method⁵⁸ within the software package CP2K⁵⁹ and for Tully's model systems as standalone python code. These are accessible publicly via github repositories at: github.com/95ellismle. This work will only focus on results from the CP2K implementation as we will later see this code extended and applied to systems of real Ethylene molecules.

2.1 Testing My Implementation

The motivation behind implementing CTMQC for the Tully models was to serve as a verifiable base for later extensions, such as integrating CTMQC within the fragment-orbital based (FOB)⁶⁰ framework which will be discussed in a later chapter⁷. Using such simple systems will also help to clarify how each new parameter works and make testing and debugging easier. As well as many numerical tests on individual terms in the equations, I have implemented some physical tests on the overall system dynamics. In this section, I will outline the key tests I have performed on both the Ehrenfest and full CTMQC parts of the equations. These are: ...

2.1.1 Comparisons To Literature

There have been 2 papers published applying CTMQC to the Tully models^{2,3} and both contain results for the 4 Tully models shown in fig 2.1. The results contain data on the (ground state) adiabatic populations and a coherence indicator as shown in equation (2.4) for 16 different simulations (a low and high initial momentum simulation of Models 1, 2, 3 and 4).

$$|\rho_{12}(t)|^2 = \frac{1}{N_{tr}} \sum_{I=1}^{N_{tr}} |C_1^{(I)}(t)|^2 |C_2^{(I)}(t)|^2 \quad (2.4)$$

In order to compare to results in the literature the same setup had to be used. In this case this meant sampling individual replicas' initial conditions (positions and momenta) from a Wigner distribution with a mean position and momenta given in appendix A. The wavefunction was initialised purely on the ground state and the same integrator was used for the nuclear and electronic propagation (velocity verlet and RK4 respectively).

2.1.2 Ehrenfest

My results as well as the relevant data taken from Agostini, 16 and Gossel, 18^{2,3} are shown in figure 2.2 for Ehrenfest dynamics. This is equivalent to full CTMQC dynamics where the quantum momentum term is set to 0. Hence, we can test most parts of the code (i.e. Runge-Kutta propagation, velocity verlet, inputs, force calculations etc...) while ignoring the new quantum momentum and accumulated adiabatic force terms.

The results in figure 2.2 show that both the adiabatic populations and coherence indicator give exactly the same results as in the literature, within reasonable error. Any deviations of results come from either a slightly different initial sampling of positions (sampled from a Wigner distribution) or small errors in retrieving data from the graphs in each paper. For example, in the case of the high initial momentum simulation of model 4 all 3 results show some differences though the trend is very similar. This is true also in the Model 2 results where the Agostini, 16 populations show some transient oscillations before settling onto the same equilibrium population. This may be due to a smaller

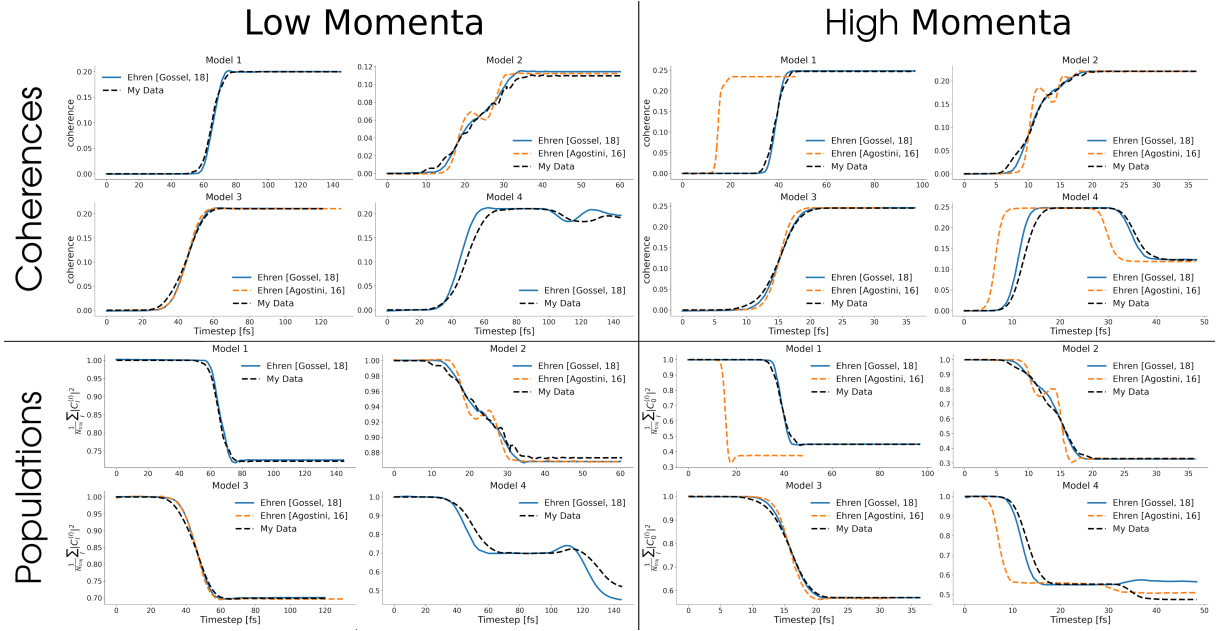


Figure 2.2: A comparison of my implementation of Ehrenfest (for 4 model Hamiltonians) and results from the literature. The black dashed lines show my data (ground state ad pops), the orange dashed lines are data from Agostini, 16² and the blue solid lines are from Gossel, 18³. The figures are labelled with their model number, whether the initial momentum was high or low and whether the populations or coherence indicator was plotted.

spread of positions being used in the initial sample leading to similar oscillations that aren't smoothed out in the averaging over all replicas. There are also a couple of models that start at a slightly different initial mean position in Frederica, 16 thus they hit the nonadiabatic crossing region sooner. These are model 1 and 4 for the high momentum case.

Although not all results are exactly the same, I believe the populations agree well enough within a reasonable error to serve as a confirmation of my implementation.

2.1.2.1 Comparisons of Ehrenfest to Other Data

In a Subotnik, 2010⁶¹, results were published for Ehrenfest simulations carried out on the 3 original Tully Models. In that work, the author presented the probabilities of the population being found transmitted through the region of nonadiabatic coupling on the ground or excited state and the probability of being reflected on the ground or upper state. In the results below, I will show comparisons of just the transmission probability

onto the ground state. That is, the population that travels on the ground state beyond the region of high nonadiabatic coupling. Other probabilities will not be shown in the interest of brevity, though they agree with the published results as well as the ground state transmission in figure 2.3.

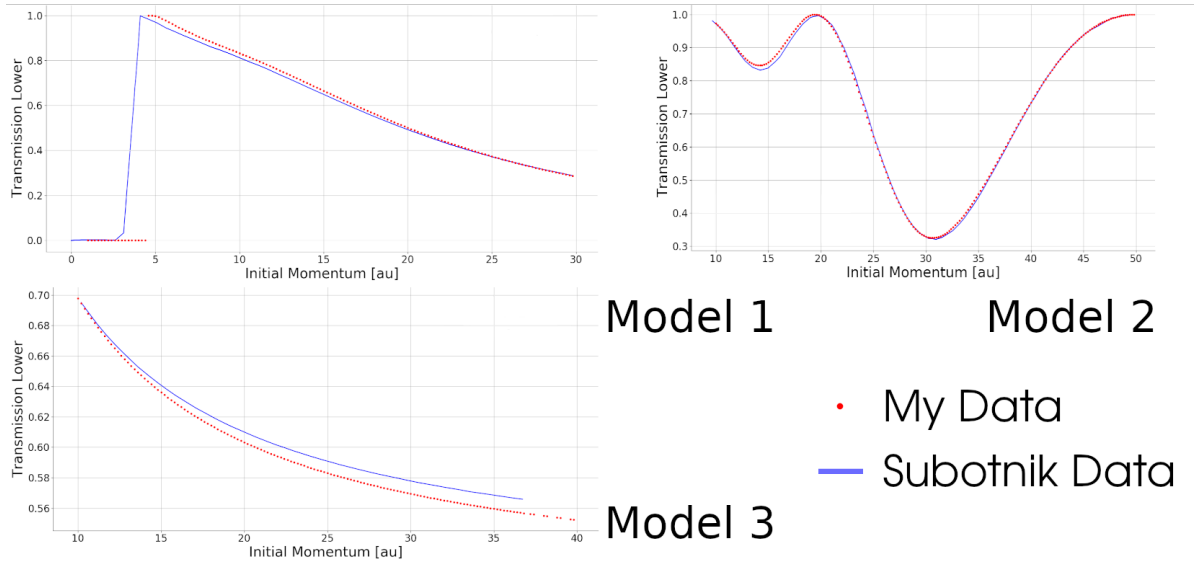


Figure 2.3: Comparison of transmission probabilities through the region of high nonadiabatic coupling on the ground state. Tully model 1 is shown in the top-left, Tully model 2 is shown in the top-right and Tully model 3 is shown in the bottom-left.

As can be seen in figure 2.3 my implementation of the Ehrenfest simulation code for the Tully models agrees very well with those in Subotnik, 2010⁶¹. The small deviation (less than 1% disagreement) within each model is due to errors in retrieving data from images in original paper.

2.1.3 CTMQC

To test the full CTMQC equations I now turn on the quantum momentum ($\mathcal{Q}_{l,k,v}^{(I)}$) and accumulated adiabatic force ($\mathbf{f}_{l,v}^{(I)}$) terms. These provide the extra decoherence that is missing in the standard Ehrenfest representation and allow populations of individual replicas to collapse onto a single adiabatic state. Without these terms (e.g. in Ehrenfest dynamics) all replica follow the same mean potential energy surface and detailed balance is not conserved.

The results for my implementation are given in figure 2.4. This time, unlike in the

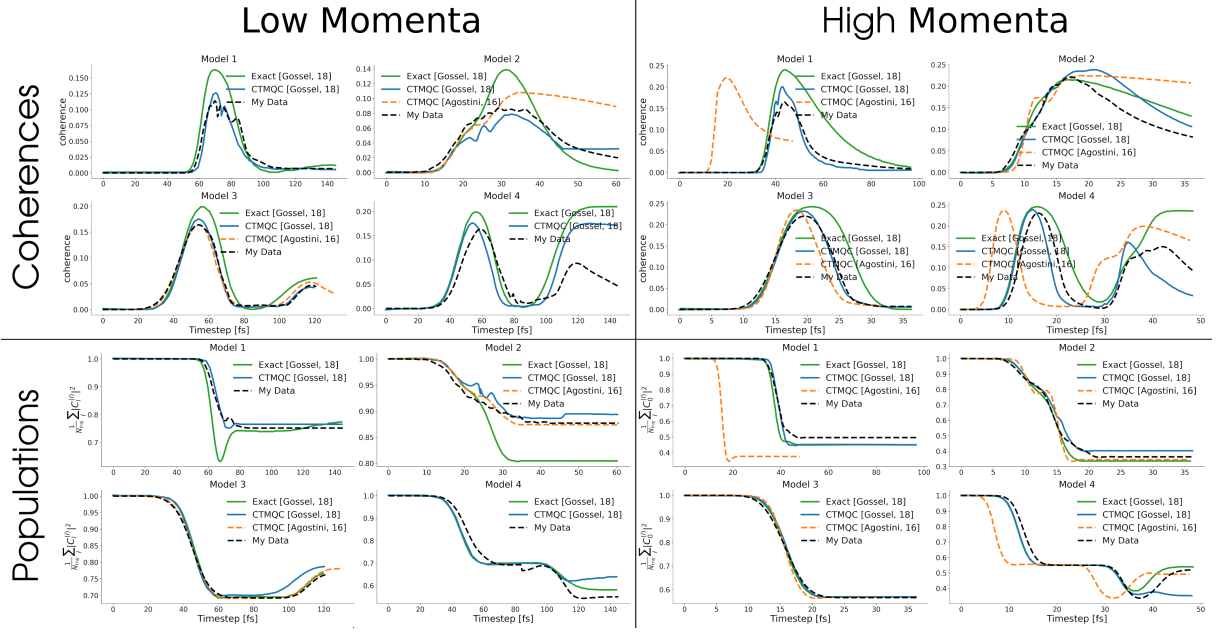


Figure 2.4: A comparison of my implementation of full CTMQC (for 4 model Hamiltonians) and results from the literature. The black dashed lines show my CTMQC data (ground state ad pops), the orange dashed lines are data from Agostini, 16² and the blue solid lines are from Gossel, 18³. The solid green line shows data from exact quantum mechanical simulations given in Gossel, 18. The figures are labelled with their model number, whether the initial momentum was high or low and whether the populations or coherence indicator was plotted.

Ehrenfest code, we see some major discrepancies between the 3 results. These cannot solely be explained as small errors from slightly different sampling of initial positions. We can see that the errors mainly appear in the coherence indicator, looking at the bottom row in figure 2.4 it appears that both the Agostini and Gossel results match mine (in dashed black line) very closely. The largest difference is seen in model 4, high momentum where the Gossel data and mine follow a similar trend and the Agostini data follows the exact curve more closely. However, looking at the coherence indicators in the above row we see a different story. My data tends to follow the Gossel data fairly closely, while the Agostini data follows a different pattern. This is due to differing parameters being used to calculate the quantum momentum term.

To calculate the quantum momentum one must take the spatial derivative of the nuclear density. However, the nuclei are classical and represented by a point. In order to calculate the nuclear density the procedure outlined in the supplementary information of

Min, 17⁵⁶ was to smear out the nuclear density by describing each classical atom with a gaussian distribution of width σ and mean $\mathbf{R}_v^{(I)}(t)$ (i.e. the atomic position). The method for determining the parameter σ has not been outlined therefore it is very hard to develop a method to exactly reproduce the results found in the 2 CTMQC papers. In figure 2.4 a constant sigma of $\sigma = 0.35$ bohr was taken to closely match the Gossel, 18 data. The fact that the curves match in many cases almost exactly makes me think this was the method employed in Gossel, 18 too. It also serves as a confirmation of the full implementation of CTMQC.

2.1.4 Norm Conservation

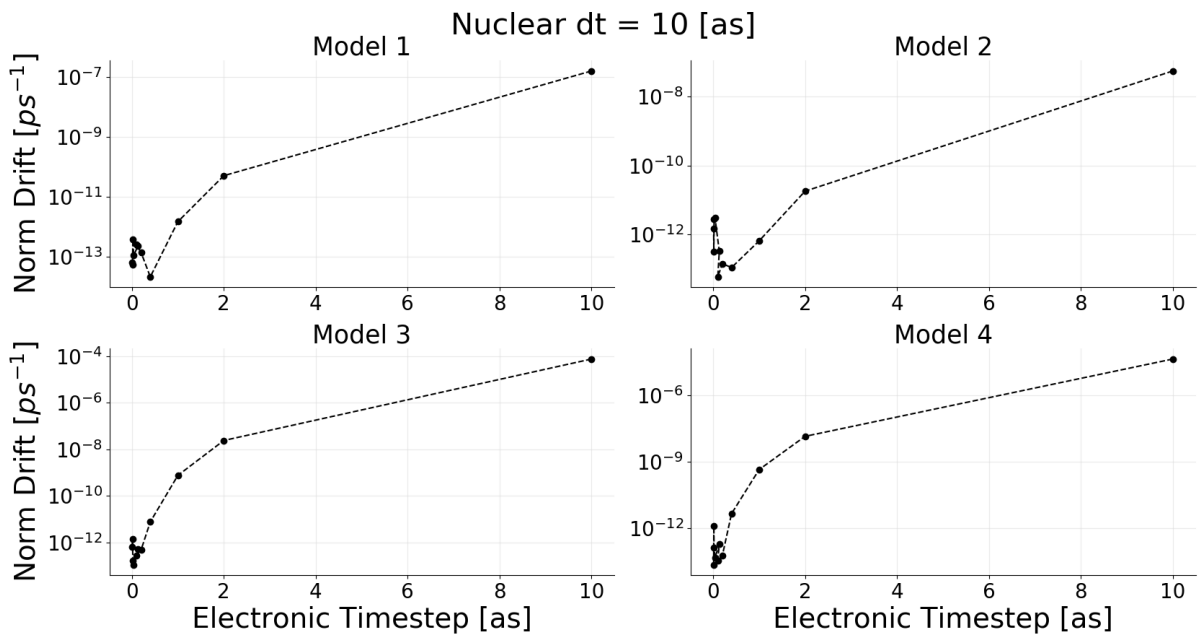


Figure 2.5: The norm conservation averaged over all replicas for Ehrenfest simulations with various electronic timesteps for each Tully model using a initial high momenta.

In appendix E, it is shown that the norm of the adiabatic expansion coefficients should be conserved throughout the simulation. In order to test this simulations were carried out using the parameters from the high momentum cases given in appendix A with various size electronic timesteps (i.e. the timestep used to propagate the electronic subsystem). The nuclear timestep was held constant. As can be seen in figure 2.5, the norm of the wavefunction is conserved within numerical error (10^{-12}) when using a sufficiently small timestep in every Tully model. However, when we now use the full CTMQC equation we

see a very different picture.

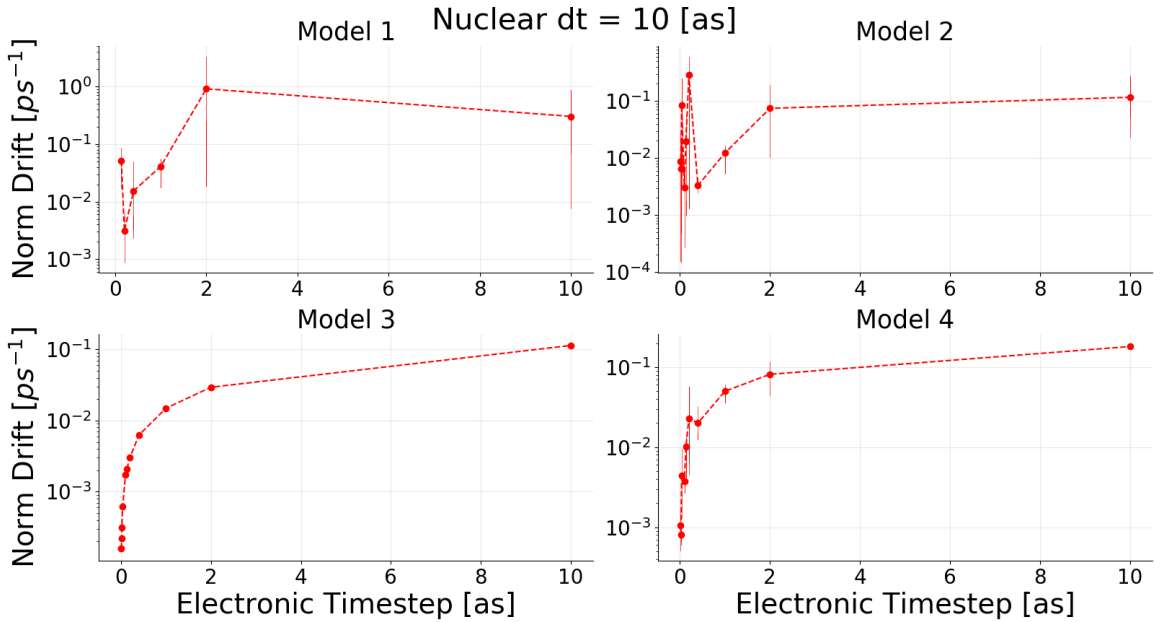


Figure 2.6: The norm conservation when using standard CTMQC as outlined in the literature for each of the Tully models. These simulations were ran with a high initial momentum. The red markers show data points and vertical bars show error bars associated with each point.

In figure 2.6, we can see that only in Model 3 we see a similar trend as in Ehrenfest for the norm conservation -i.e. a decreasing electronic timestep gives a rapidly decreasing norm drift. In models 1 and 2 we see that the norm drift doesn't get much better as we decrease the timestep and there are large error bars associated with each data point. In model 4 this is less pronounced but is still clearly effected. This is due to an instability in the way the quantum momentum term ($\mathcal{Q}_{lk,v}^{(I)}$) is calculated.

The calculation of the quantum momentum is discussed in detail in Min, 17⁵⁶ and outlined in the introduction to the thesis in section 1.6. As mentioned in that section, the denominator in the expression for $\mathbf{R}_{lk,v}$ may be positive or negative and when it switches between the 2 it can approach zero very closely. If this denominator approaches zero more quickly than the numerator then we can see large spikes in the $\mathbf{R}_{lk,v}$ term which can lead to large norm drifts.

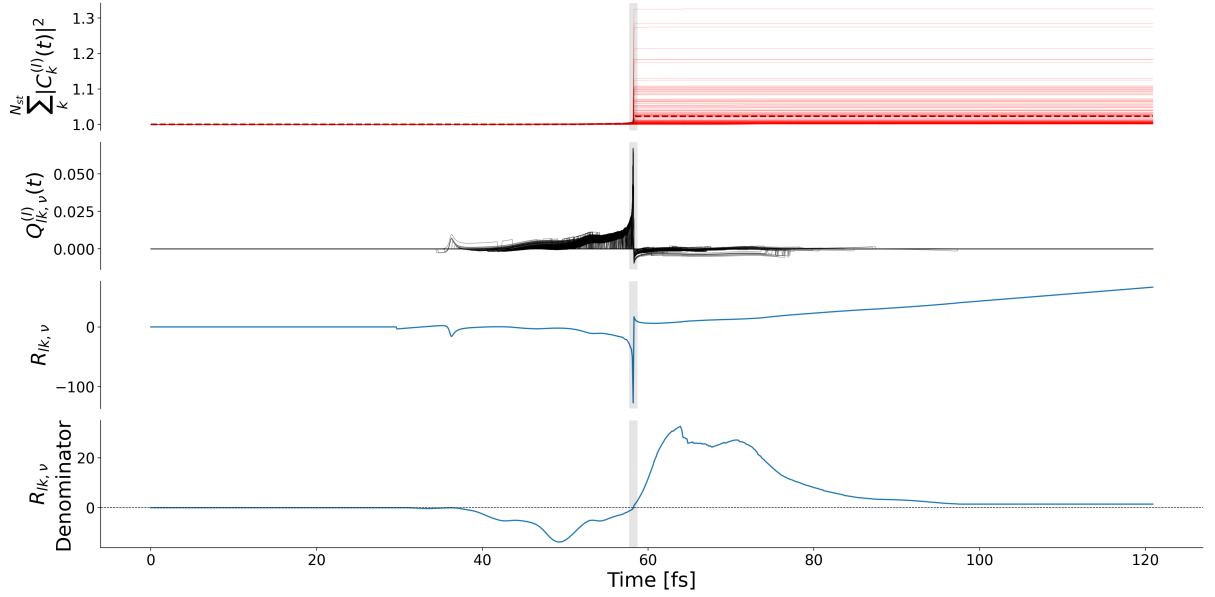


Figure 2.7: As the denominator of the $\mathbf{R}_{lk,v}$ term approaches zero (bottom panel) the full $\mathbf{R}_{lk,v}$ term (2nd to bottom panel) can approach infinity which propagates through the $\mathcal{Q}_{lk,v}^{(I)}$ term (2nd to top panel) causing discontinuities and norm drift in the populations (top panel). The grey vertical bar denotes the region the denominator approaches 0. The thin solid red lines in the top panel show the norm drift for individual replicas.

2.1.4.1 Quantum Momentum Instabilities

As we can see in figure 2.7, as the denominator of the $\mathbf{R}_{lk,v}$ term approaches 0 the full $\mathbf{R}_{lk,v}$ term may spike causing a discontinuity in the populations. The reason this only occurs in Models 1, 2 and 4 is due to the fact that the difference in the adiabatic momenta terms ($\mathbf{f}_{l,v}^{(I)} - \mathbf{f}_{k,v}^{(I)}$) doesn't cross 0 in Model 3. In order to correct for this I have investigated a number of corrections to the calculation of the quantum momentum. These depend on the detection of the spikes/divergences in the $\mathbf{R}_{lk,v}$ term and then the appropriate treatment of them. In order to detect the divergences a simple threshold on the $|\frac{\delta}{\delta t} \mathbf{R}_{lk,v}|$ is applied when the denominator of the $\mathbf{R}_{lk,v}$ is sufficiently close to 0. For example, if the absolute time-derivative of the $\mathbf{R}_{lk,v}$ term is larger than a value (say 5) and the bottom of the fraction in equation (1.15) is within 0.1 of 0 then we assume the $\mathbf{R}_{lk,v}$ term is diverging and the simulation code then uses a different method of propagating the electronic coefficients.

The alternative propagation methods I have investigated are:

1. Use Ehrenfest Dynamics (set $\mathcal{Q}_{lk,v}$ term to 0).
2. Extrapolate the value of $\mathbf{R}_{lk,v}$ from values before the divergence (see appendix C.1).
3. Switch to using the alternative intercept $\mathbf{R}_{0,v}^{(I)}$ (see appendix C.2).

of these 3 methods, method 3 was the most successful in reducing the norm drift in the Tully Models as can be seen in figure 2.8. In figure 2.8 we see the norm drift results after

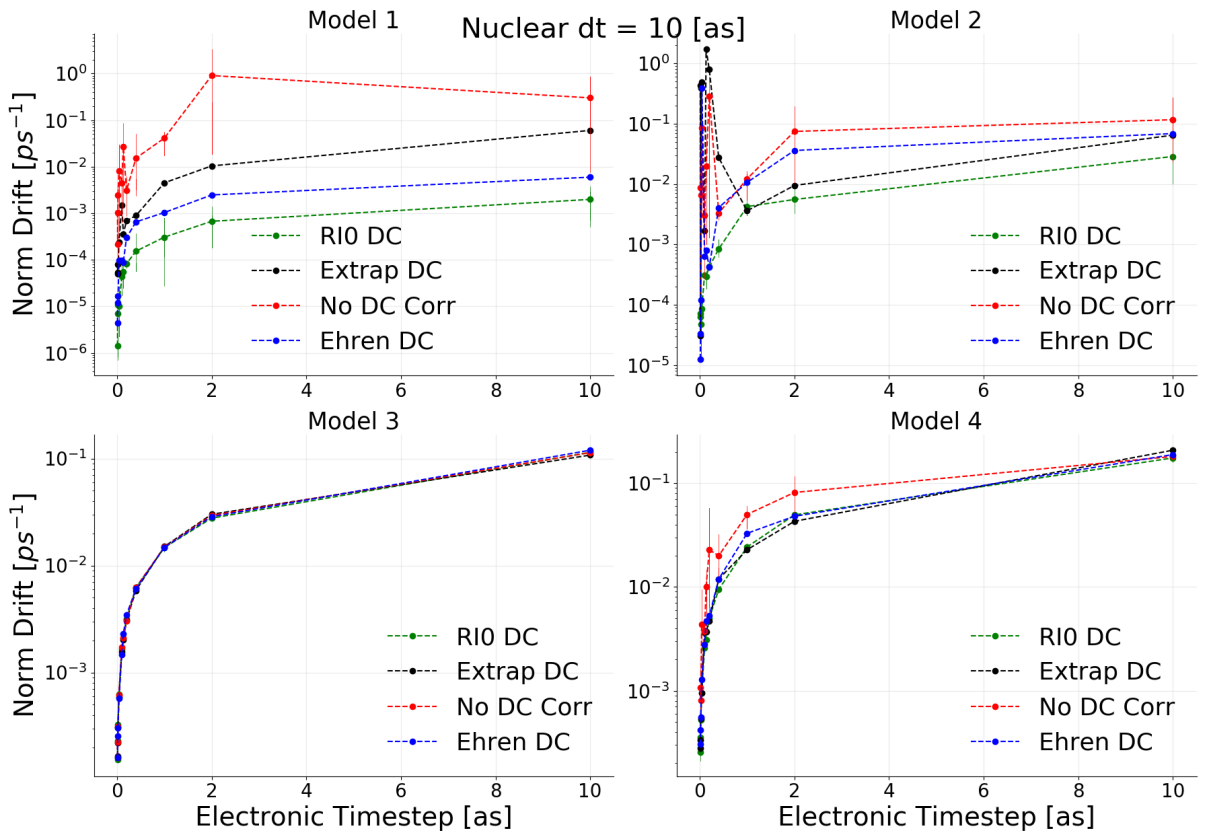


Figure 2.8: Norm conservation in CTMQC after applying a divergence correction to the $\mathbf{R}_{lk,v}$ term. RI0 refers to method 3, Extrap DC refers to method 2 and Ehren DC refers to method 1. No DC Corr shows the population norm without any corrections applied.

the 3 $\mathbf{R}_{lk,v}$ correction methods have been applied. The red curve shows the original data (as in figure 2.6) with its large divergences in the norm drift. The green curve shows the alternative intercept method, the blue curve shows the effect of switching to Ehrenfest during the $\mathcal{Q}_{lk,v}^{(I)}$ spikes and the black shows a method that involved extrapolating the $\mathbf{R}_{lk,v}$ value from data before the spike began. We can see clearly all 3 methods improve

the norm drift, though using the alternative intercept seems to help the most. Model 3 is not affected as we do not see these divergences in the $\mathbf{R}_{lk,v}$ due to the denominator in this particular model never crossing from positive to negative (through zero). It is important to note that in each of the models with the divergence correction applied all models exhibit the expected trend of decreasing the time-step improves norm conservation. However, the norm conservation in all 4 models is still significantly higher ($\sim 7\text{-}8$ orders of magnitude) higher than that of Ehrenfest. I think this is due to the product of the adiabatic populations, $|C_l^{(I)}|^2 |C_k^{(I)}|^2$, being used in the calculation of the quantum momentum which can be a more quickly varying quantity than just the adiabatic populations alone.

2.1.5 Mathematical Tests

Multiple tests of the implementation of the quantities in the equations have been implemented in the code to ensure correct outputs. A checklist of any mathematical tests is given below:

- Checking the (anti-)symmetry of the (NACV) Hamiltonian when constructed
- Comparing the adiabatic momentum term to post-production time-integrated adiabatic energies (using trapezium rule)
- Checking special case solutions when all replicas are initialised at the same position such as:
 - $\mathcal{Q}_{lk,v}^{(I)} = 0$
 - CTMQC = Ehrenfest
- Checking special cases for when $\boldsymbol{\sigma}$ is replica independent (i.e. $\boldsymbol{\sigma}^{(I)} = \boldsymbol{\sigma}$):
 - $\boldsymbol{\sigma} = \frac{\hbar}{2\sigma^2}$
 - $\mathbf{R}_{lk,v} = \mathbf{R}_v^{(I)} \frac{\hbar}{2\sigma^2}$ (Assuming the positions, $\mathbf{R}_v^{(I)}$ are also replica independent)
- If all adiabatic population is localised on a single state ($|C_l^{(I)}|^2 = [1, 0, 0, \dots, 0]$). Then we get Ehrenfest dynamics on that replica.

I have also provided 2 (more substantial) mathematical tests for the code below in the following sections.

2.1.5.1 Time Derivative of Replica-Sum of Adiabatic Populations

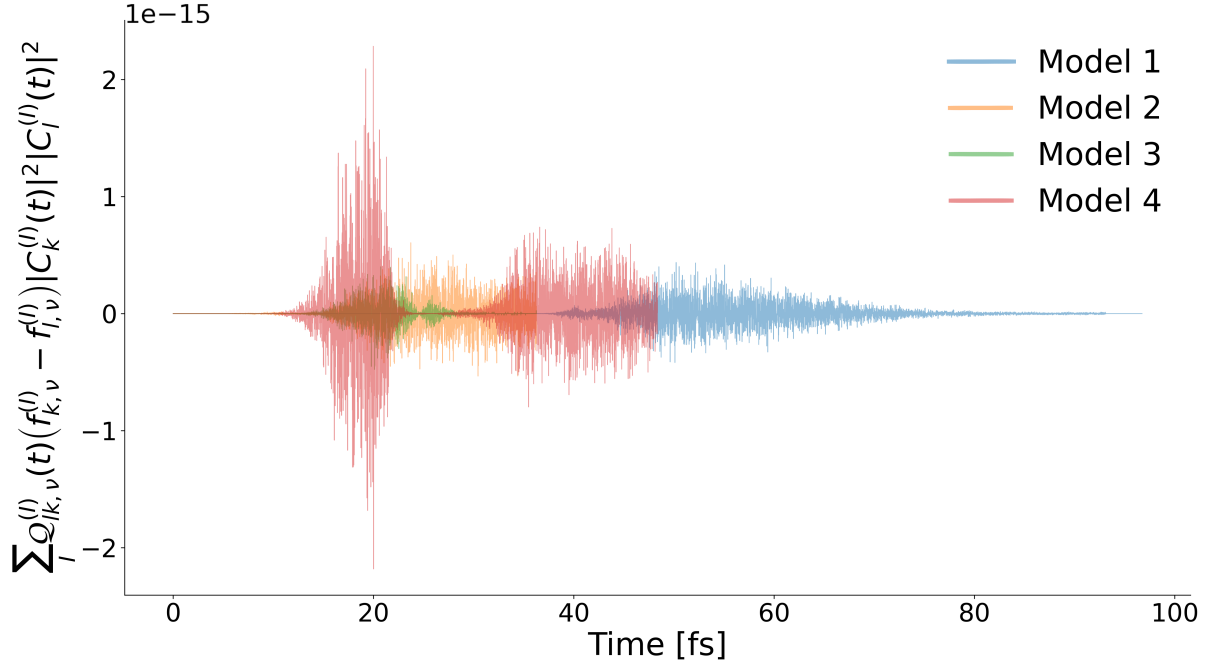


Figure 2.9: The conserved quantity given in equation (2.5). Each color represents data outputted by a simulation using a different model (specified in the legend). Each time-series is plotted with a translucent color meaning each model's data can be seen at once.

In the SI of Min, 17⁵⁶ a conservation equation (S27) is given. This is repeated below in equation (2.5)

$$\sum_I \mathcal{Q}_{lk,v}^{(I)}(t) \left(f_{k,v}^{(I)} - f_{l,v}^{(I)} \right) |C_k^{(I)}(t)|^2 |C_l^{(I)}(t)|^2 = 0 \quad \forall l, k, v \quad (2.5)$$

An example time-series of this quantity is given in figure 2.9 for each Tully model. The data used to calculate come from simulations of each of the Tully models using the parameters given in appendix A. No smoothing was used for the $\mathbf{R}_{lk,v}^{(I)}$ term. It can be seen in this figure that the conservation quantity hovers around 0 for each model with a maximum deviation of 10^{-15} m_eHa.

2.1.5.2 $\sum_l \mathbb{X}_{qm,ll} |C_l^{(I)}|^2$

As the equations are currently formulated another numerical test validating the quantum momentum part of the propagation equations for the coefficients can be used. The CTMQC equation for the propagation of the adiabatic expansion coefficients is given in

equation (1.10). The quantum momentum part of this equation is given below in equation (2.6).

$$\mathbb{X}_{qm,ll}^{(I)} = \sum_{v=1}^{N_n} \sum_k \frac{\mathcal{Q}_{lk,v}^{(I)}}{\hbar M_v} \cdot [\mathbf{f}_{k,v}^{(I)} - \mathbf{f}_{l,v}^{(I)}] |C_k^{(I)}|^2 \quad (2.6)$$

Where $\mathbb{X}_{qm,ll}^{(I)}$ is the diagonal matrix that, when multiplied with the adiabatic expansion coefficients, gives the quantum momentum contribution to the propagation of the expansion coefficients.^I

We can test the construction of this matrix within the code by multiplying by the adiabatic populations and summing as shown in equation (2.7). It can be shown, assuming perfect norm conservation, that this should equal exactly 0 -due to the symmetry of the $|C_l^{(I)}|^2 |C_k^{(I)}|^2$ and the quantum momentum matrix. This is checked for every timestep during propagation.

$$\sum_l \mathbb{X}_{qm,ll}^{(I)} |C_l^{(I)}|^2 = 0 \quad (2.7)$$

2.1.6 Energy Conservation

2.1.6.1 Ehrenfest

Energy conservation is a very important property in most molecular dynamics simulations. In Ehrenfest of mean-field molecular dynamics nuclei are propagated on a population-weighted mean potential energy surface, e.g. $\sum_k |C_l^{(I)}(t)|^2 = E_{eff}(t)$ ⁶². Kinetic energy of the classical nuclei is given by the standard formula, e.g. $\frac{1}{2}mv^2$. We can therefore write down the conserved quantity as defined below in equation (2.8):

$$\frac{dE}{dt} = \frac{d}{dt} \left[\frac{1}{2}mv^2 + \sum_k |C_l^{(I)}(t)|^2 \right] = 0 \quad (2.8)$$

As in the norm conservation checks in section 2.1.4, parameters from the high momentum cases were taken as initial conditions for simulations with various nuclear timesteps, this time holding the electronic timestep constant. The high momenta cases were chosen to show the worst case energy conservations, within this very simple system. A linear line of

best fit was then fitted to the data and the drift in the total energy (given in (2.8)) was calculated from its gradient. The results of these simulations are given in figure 2.10. In

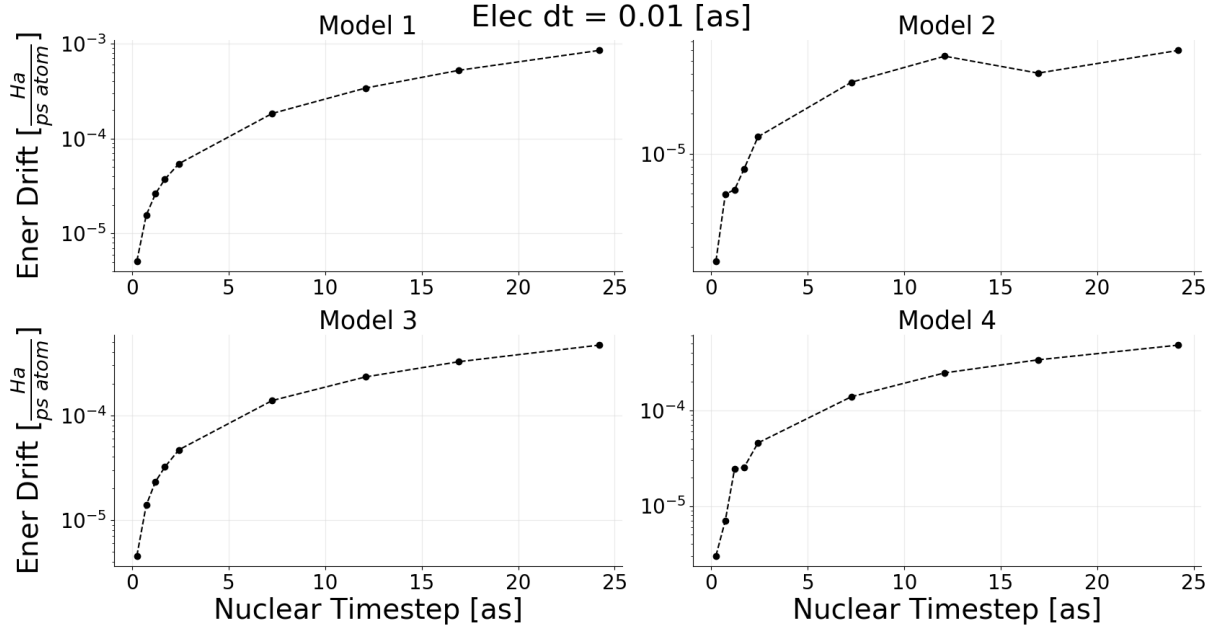


Figure 2.10: Energy conservation values for various nuclear timesteps for the high momentum case of each Tully model.

figure 2.10, we see the expected results that as the nuclear timestep is decrease the drift in the total energy also decreases. This trend validates the implementation and shows that in the limit of infinitely small timestep (and infinite computer precision) perfect energy conservation would be achieved. However, fairly small nuclear timesteps are required to achieve reasonable energy conservations. This is because the system contains only 1 atom with a mass comparable to that of Hydrogen. If one needed an improved energy conservation a higher order integrator than the velocity verlet used here may also improve results slightly.

2.1.6.2 CTMQC

In CTMQC the energy conservation is

2.2 Calculation of $\mathcal{Q}_{lk,v}^{(I)}$

In order to calculate the quantum momentum the nuclear density must be constructed from the nuclei's positions. However, the nuclei are treated classically, i.e. as point

particles. To approximate the nuclear density from atomic positions a normal distribution is placed with the mean at position of each particle with a width of σ . This introduces a new parameter which must be tuned in order to reproduce sensible results. If the width is too small the resulting nuclear density is too noisy and the quantum momentum values unreliable. If the width is too large the nuclear density is very smooth with little variation and the quantum momentum values become very small. Seeing as the quantum momentum is one of the most important factors affecting coherence between electronic states the careful selection of the σ parameter is important. This issue is not very well addressed in the literature. In this section I will show results of calculation carried out with various values of σ as well as a method for a dynamic calculation of $\sigma_v^{(I)}(t)$ on the fly.

2.2.1 Constant Values of σ

The simplest option for the calculation of $\mathcal{Q}_{lk,v}^{(I)}$ is to keep the gaussian width parameter, σ , constant throughout the simulation. This also allows us to investigate the role of σ within the simulations and to determine its influence on the dynamics. To this end various simulations were carried out on the 4 Tully models with the high initial momentum. In each simulation parameters were all the same apart from the value of σ which took a value of either: 0.1, 0.2, 0.3, 0.35, 0.4, 0.5 or 1. The results for these simulations are shown in figure 2.11. In this figure, we see that as the σ parameter is increased the levels of decoherence also increases. This means for larger σ values electronic populations remain in a mixed state for longer and take more time to collapse onto a single adiabatic state. Clearly, the construction of this σ parameter is important for recovery of correct electronic dynamics. Surprisingly, this doesn't seem to have much of an effect on the resulting populations. However, this is due to the fact in the limit of large σ CTMQC becomes identical to Ehrenfest dynamics and Ehrenfest dynamics captures the evolution of the adiabatic populations very well for each model, with the exception of model 4. It should also be noted that for small values of σ , propagation using CTMQC can become unstable due to a very high quantum momentum term.



Figure 2.11: 4 high momenta cases of the Tully models with a varying σ parameter used in the calculation of the quantum momentum.

2.2.2 Dynamic $\sigma_v^{(I)}(t)$ calculation

In the appendix of Gossel, 18³ an algorithm was outlined to calculate σ on-the-fly based on the density of replicas within a cutoff distance of each atom. This is given in appendix F.

Chapter 3

CTMQC applied to molecular systems

In order to apply CTMQC to large molecular systems (hundreds of molecules) a new way to construct the Hamiltonian is needed. In this work I have implemented the CTMQC equations within the fragment-orbital based framework. This relies on the equations being expressed in a pseudo-diabatic basis and the Hamiltonian being constructed in 2 parts: the diagonal elements (site energies) and the off-diagonals (electronic couplings). The basis is termed 'pseudo-diabatic' due to the fact that non-adiabatic coupling vectors are small but non vanishing, this results in a basis where the excess charge carrier is strongly but not strictly localised on a single molecule. Within the Hamiltonian, the site energies are calculated via classical force-fields and the electronic couplings are calculated via the analytic overlap method^{58,60} (AOM). In this method the coupling elements are assumed to be proportional to the overlap between the highest singly occupied molecular orbitals (SOMO) on the donor and acceptor molecules (see equation (3.1)). This approximation is often used in the literature, e.g. in the fragment orbital density functional theory^{63–65} (FODFT) method and has been shown to be valid for π -conjugated molecules^{58,66}.

$$H_{ab} = C\langle \varphi_a | \varphi_b \rangle = CS_{ab} \quad (3.1)$$

Where $\varphi_{a(b)}$ represents a singly occupied molecular orbital on the donor (acceptor) and C is the scaling constant and comes from DFT parameterisation. The singly occupied molecular orbitals are calculated as a linear combination of Slater-type orbitals (STO) as in equation (3.2). In this equation we loop over each molecule in the atom and sum

the size of the contribution, $c_{p\pi,i}$, multiplied by the STO, $p_{\pi,j}$. In this case the STO is represented by a p-orbital. The size of the p-orbital on each atom, $c_{p\pi,i}$, is parameterised before the simulation with DFT.

$$|\varphi_{mol}\rangle = \sum_{i \in mol}^{N_{atoms}} c_{p\pi,i} |p_{\pi,i}\rangle \quad (3.2)$$

Importantly, the AOM method offers a very fast way to calculate the off-diagonal elements of the hamiltonian via a finite-difference method with an accuracy comparable to that of DFT methods. This has been implemented within an open-source software package named CP2K and is used by a fragment-orbital based surface hopping technique to study large systems of hundreds of molecules. In the next chapter the surface hopping technique will be discussed in further detail and applied to a system of pentacene molecules in order to investigate charge carrier (hole) transfer within amorphous systems.

3.1 Basis Transformation

In order to use the FOB method, as stated above the CTMQC equations in the adiabatic basis must be transformed to the diabatic basis. In the following derivation C_l will represent the adiabatic expansion coefficient corresponding to state l and u_l will represent the orthogonal diabatic expansion coefficients.

The CTMQC equations in the adiabatic basis are given below in equation (3.3) of the forces and (3.4) coefficients:

$$\begin{aligned} \mathbf{F}_v^{(I)} = & - \sum_k |C_k^{(I)}|^2 \nabla_v E_k^{(I)} - \sum_{k,l} C_l^{*(I)} C_k^{(I)} \left(E_k^{(I)} - E_l^{(I)} \right) \mathbf{d}_{v,lk}^{ad,(I)} \\ & - \sum_{l,k} |C_l^{(I)}|^2 \left(\sum_{v'}^{N_n} \frac{2}{\hbar M_{v'}} \mathcal{D}_{v',lk}^{(I)} \cdot \mathbf{f}_{l,v'}^{(I)} \right) [\mathbf{f}_{k,v}^{(I)} - \mathbf{f}_{l,v}^{(I)}] |C_k^{(I)}|^2 \end{aligned} \quad (3.3)$$

$$\begin{aligned}\dot{C}_l^{(I)} = & -\frac{i}{\hbar} E_l^{(I)} C_l^{(I)} - \sum_k C_k^{(I)} \sum_{v=1}^{N_n} \frac{\mathbf{P}_v^{(I)}}{M_v} \cdot \mathbf{d}_{v,lk}^{ad,(I)} \\ & - \sum_{v=1}^{N_n} \sum_k \frac{\mathcal{Q}_{v,lk}^{(I)}}{\hbar M_{v'}} \cdot [\mathbf{f}_{k,v}^{(I)} - \mathbf{f}_{l,v}^{(I)}] |C_k^{(I)}|^2 C_l^{(I)}\end{aligned}\quad (3.4)$$

Where:

- $E_k^{(I)}$ is the adiabatic energy for state k and trajectory I
- $C_k^{(I)}$ is the adiabatic expansion coefficient for state k and trajectory I
- $\mathbf{P}_v^{(I)}$ is the classical momentum of atom v on trajectory I
- $\mathbf{d}_{v,lk}^{ad,(I)}$ is the nonadiabatic coupling vector (given in the adiabatic basis)
- M_v is the mass of nuclei v
- $\mathcal{Q}_{v,lk}^{(I)}$ is the quantum momentum vector for atom v corresponding to the lk pair of states in trajectory I
- $\mathbf{f}_{l,v}^{(I)}$ is the adiabatic momentum on state l , atom v and trajectory I

3.1.1 Coefficients

To transform the equation for the propagation of the coefficients it is far neater to use the notation of linear algebra as in equation (3.5) below:

$$\dot{\mathbf{C}}^{(I)} = \mathbb{X}_v^{(I)} \mathbf{C}^{(I)} = \left(\mathbb{X}_{eh,v}^{(I)} + \mathbb{X}_{qm,v}^{(I)} \right) \mathbf{C}^{(I)} \quad (3.5)$$

Where the \mathbb{X} matrices are defined as in equations (3.6) and (3.7) below.

$$\mathbb{X}_{lk,v}^{eh(I)} = -\frac{i}{\hbar} E_l^{(I)} - \sum_v \frac{\mathbf{P}_v^{(I)}}{M_v} \cdot d_{lk,v}^{ad,(I)} \quad (3.6)$$

$$\mathbb{X}_{ll,v}^{qm(I)} = - \sum_{v=1}^{N_n} \sum_k \frac{\mathcal{Q}_{v,lk}^{(I)}}{\hbar M_{v'}} \cdot [\mathbf{f}_{k,v}^{(I)} - \mathbf{f}_{l,v}^{(I)}] |C_k^{(I)}|^2 \quad (3.7)$$

Using the identities:

$$\mathbb{U}^{-1} = \mathbb{U}^\dagger \quad (3.8)$$

$$\mathbf{C}^{(I)} = \mathbb{U}^{\dagger(I)} \mathbf{u}^{(I)} \quad (3.9)$$

$$\dot{\mathbf{C}}^{(I)} = \mathbb{U}^{\dot{\dagger}(I)} \mathbf{u}^{(I)} + \mathbb{U}^{\dagger(I)} \dot{\mathbf{u}}^{(I)} \quad (3.10)$$

Where $\mathbb{U}^{(I)} = \langle \phi_l^{(I)} | \psi_n^{(I)} \rangle$ is the unitary transformation matrix transforming from the diabatic to adiabatic basis. The $\mathbf{u}^{(I)}$ terms are the diabatic expansion coefficients on trajectory I.

After some algebra we arrive at:

$$\dot{\mathbf{u}}^{(I)} = \underbrace{\left(\mathbb{U}^{(I)} \mathbb{X}_{eh} \mathbb{U}^{\dagger(I)} + \mathbb{U}^{(I)} \mathbb{U}^{\dagger(I)} \right) \mathbf{u}^{(I)}}_{\text{Ehrenfest}} + \underbrace{\left(\mathbb{U}^{(I)} \mathbb{X}_{qm} \mathbb{U}^{\dagger(I)} \right) \mathbf{u}^{(I)}}_{\text{Quantum Momentum}} \quad (3.11)$$

In equation (3.11) I've separated the contribution from Ehrenfest and the contribution from the new quantum momentum terms. The Ehrenfest part can be shown to reduce to a simpler form (see Spencer, 2016⁶⁰ and Carof, 17⁶⁷ for more details). The quantum momentum term must be coded up as shown -with the transformation matrices. This gives the final equation for the propagation of the diabatic expansion coefficients, shown in equation (3.12).

$$\dot{\mathbf{u}}^{(I)} = \left(-\frac{i}{\hbar} \mathbb{H}^{(I)} - \mathbb{D}_{diab}^{(I)} \right) \mathbf{u}^{(I)} + \left(\mathbb{U}^{(I)} \mathbb{X}_{qm} \mathbb{U}^{(I)} \right)^{-1} \mathbf{u}^{(I)} \quad (3.12)$$

Where $\mathbb{H}^{(I)}$ is the diabatic Hamiltonian constructed via the AOM method, $\mathbb{D}_{diab}^{(I)}$ are the diabatic nonadiabatic coupling elements ($d_{diab,lk}^{(I)} = \langle \phi_l | \dot{\phi}_k \rangle$).

3.1.2 Forces

A full derivation of the transformation of basis for the equation propagating forces is given in appendix G. The result is given in equation (3.13) below:

$$\begin{aligned} \mathbf{F}_{eh,v}^{(I)} = & \sum_{i,j} \mathbf{u}_i^{*(I)} \mathbf{u}_j^{(I)} \left(\nabla_v H_{ij}^{(I)} + \sum_l \mathbf{d}_{lk,v}^{(I)} H_{lj}^{(I)} - \sum_l \mathbf{d}_{lj,v}^{(I)} H_{il} \right) \\ & - \sum_{l,k} |C_l^{(I)}|^2 \left(\sum_{v'}^{N_n} \frac{2}{\hbar M_{v'}} \mathcal{Q}_{v',lk}^{(I)} \cdot \mathbf{f}_{l,v'}^{(I)} \right) [\mathbf{f}_{k,v}^{(I)} - \mathbf{f}_{l,v}^{(I)}] |C_k^{(I)}|^2 \end{aligned} \quad (3.13)$$

There are a couple of things to note with this equation. Firstly, the quantum momentum part has not been transformed. This is because the forces are basis independent and doesn't need to be transformed. The quantities required for the calculation of this part of the equation are already calculated in order to propagate the coefficients so only a small amount of extra effort is required to calculate the quantum momentum force term. The Ehrenfest part of the equation has been transformed. This is because the nonadiabatic coupling vectors within the adiabatic basis are never required so are never calculated. Further, the commutator term in the diabatic basis has been shown to provide a negligible contribution to the overall force. Seeing as this term requires significant computational effort it can be neglected. This makes the calculation of the Ehrenfest forces in the diabatic basis far cheaper than in the adiabatic basis.

3.2 Testing the diabatic propagator

The diabatic propagation can be tested against the already tested adiabatic propagator using the Tully model Hamiltonian. The code should give the same results, given the same inputs. To check this, in figure 3.1, the simulations carried out in figure 2.4 were repeated though this time the diabatic propagator was used. We can see in figure 3.1 that the results for the adiabatic and diabatic propagator are almost exactly the same for each model. In model 3, where the problem with the divergent $\mathcal{Q}_{lk,v}^{(I)}$ doesn't occur, the 2 results are exactly on top of each other. In the other models there is a slight discrepancy. This is due to the unpredictable $\mathcal{Q}_{lk,v}^{(I)}$ spikes not being perfectly corrected. However, figure 3.1 still serves as confirmation of the propagation within the diabatic basis.

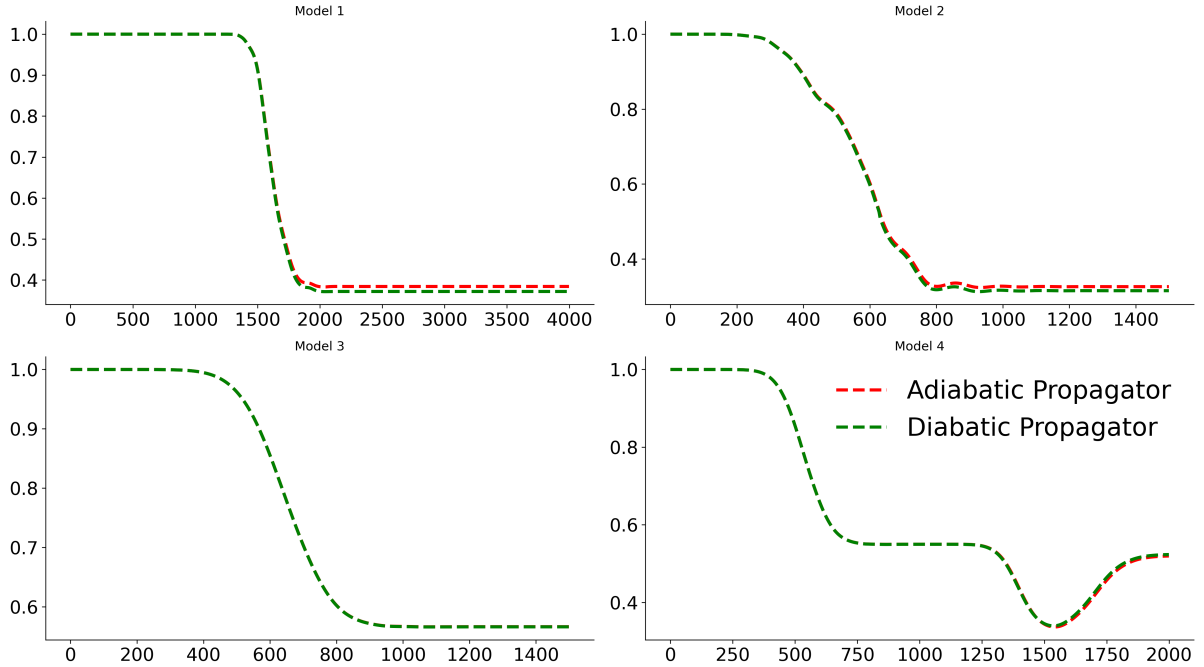


Figure 3.1: The 4 Tully models simulated using propagating the equations within a diabatic and adiabatic basis. The green line shows results from the diabatic propagator and the red line shows results from the adiabatic propagator.

3.3 Simulating Molecular Systems

To go beyond the 1D Tully model systems the AOM method is combined with CTMQC and applied to an Ethylene dimer. Fortunately, the majority of the code from the Tully model systems can be re-used. In fact, the only difference is the way the Hamiltonian (and diabatic NACE) is constructed. The code for carrying out these tasks (the AOM part) has been implemented by previous members of the group and has been well tested and verified against the literature. Therefore, I will not include any tests of this part of the code in this document but instead refer the reader to the numerous papers discussing AOM and its use in within the fewest switches surface hopping framework^{14,68–77}. An ethylene dimer was chosen as a reasonable first system due to its relative simplicity (shown in figure 3.2) the total number of atoms is 12 and only 2 electronic states will be considered. The system shown in figure 3.2 was initialised in the adiabatic ground state. Positions and velocities were sampled from a short NVT molecular dynamics equilibration. The scaling factor (C in equation (3.1)) was chosen to give a coupling of approximately 27 meV. This is approximately $\frac{1}{4} \times$ the reorganisation energy -parameterised to be 100 meV.

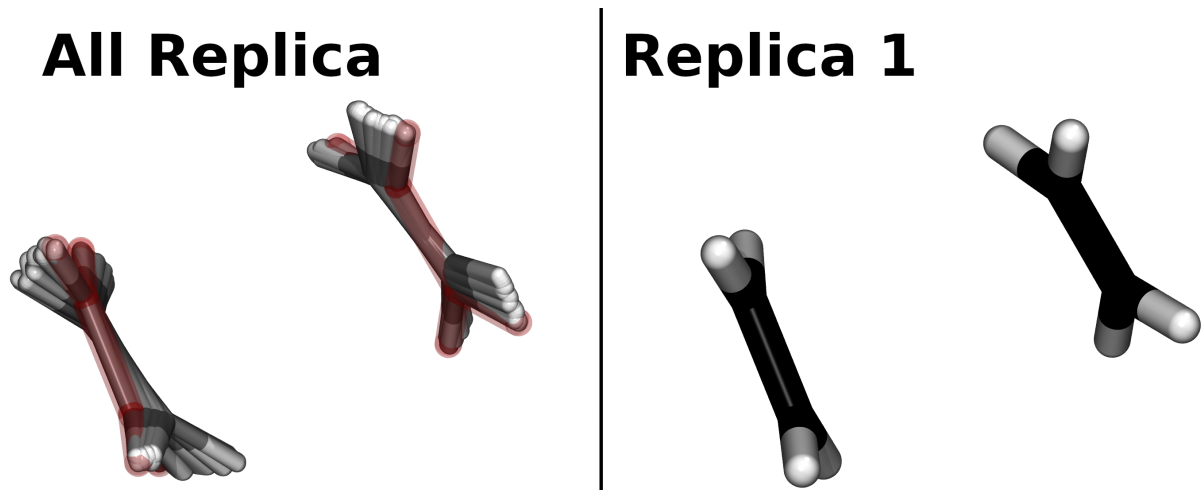


Figure 3.2: An example Ethylene dimer used to test the CTMQC implementation. The right panel shows the positions of just 1 replica. The left panel shows the positions of all replica with the replica shown on the right highlighted in red.

The amount of charge transfer is dependent on the ratio between reorganisation energy and the electronic couplings ($\frac{H_{ab}}{\lambda}$). The factor of $\frac{1}{4}$ was chosen to be a reasonable factor -seen in other organic semiconducting systems. The nuclear timestep was chosen to be 0.05fs and the electronic one was 0.005 fs. The switch to $\mathbf{R}_{0,v}^{(I)}$ was chosen as the correction method of the quantum momentum and 100 trajectories were used.

The populations from a trial run using the set up described above was carried out and the populations and norm of the adiabatic expansion coefficients are plotted in figure 3.3. In this figure we see large jumps in the norm, these are caused by the divergences in the quantum momentum term. These occur more in this system as it is more complex (more atoms, higher dimensional) and runs for a longer time with more avoided crossings. The fact that there are 12 atoms and 3 Cartesian dimensions instead of 1 means that the $\mathbf{R}_{lk,v}^{(I)}$ term must be calculated many more times increasing the probability of happening upon a divergence. The errors can also accumulate meaning that after a few trivial crossings the populations become extremely noisy. This eventually causes the code to crash and results from it cannot be trusted. Most commonly the reason for the code crashing is a large spike in the computed forces caused by a spike in the quantum momentum. This large force then causes the atoms to collide and the code to crash. The code is very stable when just using Ehrenfest dynamics. Many more simulations have been carried

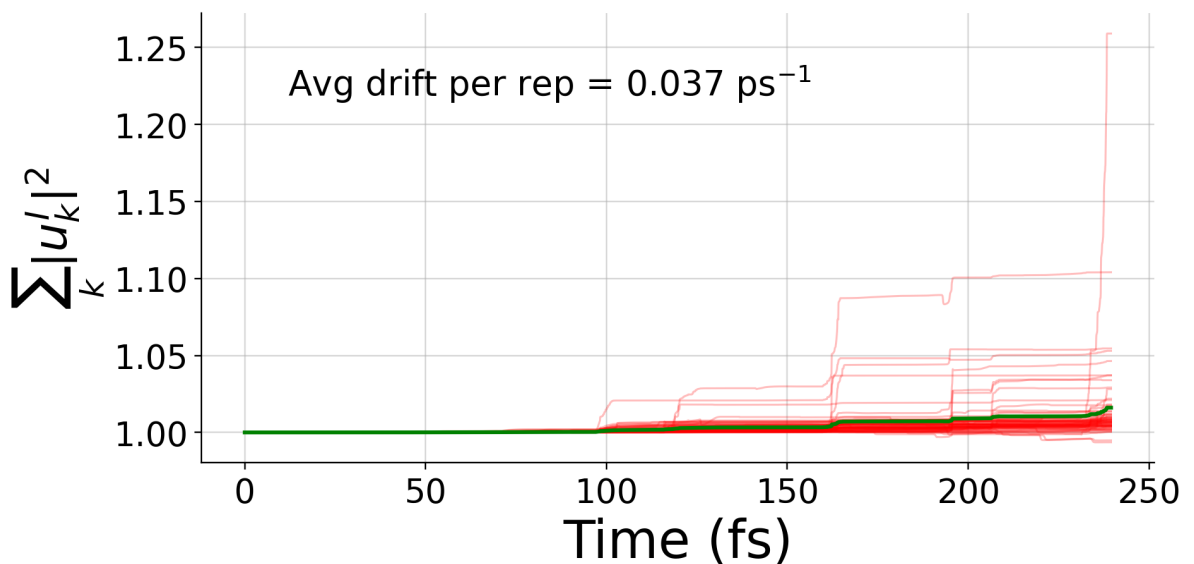


Figure 3.3: The norm of the adiabatic expansion coefficients. Thin red lines show the norm for each trajectory and the thick green line shows the average over all trajectories.

out to diagnose and fix this issue. Results from all of these cannot be included in this document though I will provide a brief summary of results below.

3.3.1 Varying the number of replicas

Increasing the number of replicas in the system, somewhat counterintuitively, decreases stability. This is because with more replicas there is more of a chance the code will stumble upon a calculation giving a divergence in the quantum momentum term.

3.3.2 Varying the timestep

Decreasing the timestep does help to improve norm conservation (before the code crashes). However, it does not lead to a more stable simulation that allows for longer timescales to be simulated. This is because decreasing the timestep provides more opportunity for a small numerical error to cause a divergence in the quantum momentum term.

3.3.3 Removing Center of Mass Motion

In some simulations the replicas positions spread out so much that the quantum momentum term became negligible. This was to prevent that from happening.

3.3.4 Varying the gaussian width (σ) parameter

If the σ parameter is set to be large (> 2) then the simulation is more stable as the quantum momentum term is smaller and errors don't accumulate as quickly. However, this the limit of a very large σ is Ehrenfest dynamics. If the σ is set to be small (< 0.2) the simulation becomes extremely unstable as the quantum momentum forces populations to decohere too quickly. This is discussed in more detail in section 2.2.

3.3.5 Turning off the quantum momentum addition to the force term

The code runs more stably if the quantum momentum term is not included in the forces. This has also been shown to be much less important for the accuracy of the results than the quantum momentum addition to the coefficients. However, even in this case the code eventually crashes after an accumulation of errors in the coefficients results in erroneous forces resulting in geometries that fail CP2K internal checks.

3.3.6 Renormalisation

This does not seem to help with stability. Furthermore, it merely helps hide the large norm drift and doesn't fix the problems it causes.

3.4 Conclusions

The CTMQC method shows great promise as a new nonadiabatic molecular dynamics (NAMD) technique. It was derived as the semi-classical limit of the exact factorisation of the time-dependent electron-nuclear wave function^{47,48}. It purports to handle decoherence corrections in a more rigorous, first principles way without the need of empirical parameters. Although this method was first reported in 2015⁴⁸, there are still very few papers reporting results using this method^{3,48,56}. With the most complex system being

restricted to a 7 atom molecule⁵⁶. I believe this is due to the problems with the current formalism. Before, the widespread acceptance of CTMQC as a standard nonadiabatic molecular dynamics method 2 critical flaws must be addressed. First is the calculation of the gaussian width parameter, σ and the second is the divergence of the quantum momentum term. It would be possible to further investigate the width parameter, perhaps through benchmarks against higher level calculations to establish a relationship between characteristics of the system and the width parameter. From a short investigation using the Tully models it seems a constant width parameter gives reasonable results and it should be set to be between 0.2 and 0.5. This problem does not seem intractable. However, it may be harder to correct for the large divergences in the quantum momentum caused by the denominator of the quantum momentum intercept term, $\mathbf{R}_{lk,v}$ approaching zero. This causes the code to become unstable for even simple molecular systems. In the 1D Tully models this could be corrected by switching to an alternative intercept, $\mathbf{R}_{0,v}^{(I)}$. However, this alternative intercept results in unphysical population transfer in regions of zero nonadiabatic coupling so cannot be used throughout the simulation.

Both these problems can both be traced back to the construction of the nuclear density from the nuclear positions. The method explored in this thesis is the method reported in the literature. That involved placing a gaussian function centered on each atomic position with a certain width, σ to smear out the position and give a smooth nuclear distribution. I believe that exploring alternative technique to construct the nuclear density from atomic positions may lead to the largest improvements in the CTMQC technique. Perhaps even allowing one to study complex molecular systems with many nonadiabatic coupling regions such as those typically found in charge transfer studies.

In this chapter I have implemented and tested a working version of CTMQC in both CP2K and as a standalone python script. These are both available for downloading from the author's github page at: <https://github.com/95ellismle>. I have given the CTMQC equations in an orthogonal diabatic basis and linked it to the AOM method, which provides a fast way of calculating electronic couplings within the Hamiltonian. I have also

highlighted what I believe to be the largest problems facing CTMQC. However, as these problems may require an entire PhD project in themselves, I have not addressed them in much detail. In the rest of this work I will discuss an alternative NAMD technique, namely fewest switches surface hopping, and apply it to large molecular system to get experimentally verifiable results.

Chapter 4

Extending surface hopping for larger systems

Fragment-orbital based surface hopping (FOB-SH) is a technique developed within the Blumberger group⁶⁰ designed to simulate large molecular systems. It has had much success in the study of organic crystalline materials^{21,67}. Most notably the electron/hole mobilities of a variety of common organic semi-conducting materials were measured within a factor of 2 of experimental measurements. However, in order to study very large amorphous and semi-crystalline systems some more memory/computation optimisations were required and electrostatic interactions (which weren't important in previous systems) needed to be accounted for. In this chapter I outline some minor improvements I implemented within the surface hopping code as well as the method used to implement the electrostatic interactions.

4.1 Code Optimisations

Chapter 5

Charge transfer in amorphous systems

Although it is important to know the maximum bound on the mobility of the charge carrier in a perfect crystal of an organic semiconductor, in reality it is very difficult to control defect formation in OSs^{78?}. This is due to van der Waals forces only weakly holding molecules at lattice sites, allowing molecules greater freedom than in traditional inorganic crystal, and increasing the chance of defect formation which can trap/scatter charge carriers reducing overall mobility. This means it is important to investigate and characterise charge transport properties for not just perfectly crystalline OSs but also those that show a range of amorphicity.

The molecule chosen to investigate amorphous films was pentacene. This molecule is a popular organic semiconductor and the subject of much research due to its high field effect mobility⁷⁹, use in device applications⁸⁰ and, more recently, the use of functionalization to alter device properties^{81,82}. The pentacene molecule consists of 5 joined benzene rings (36 atoms) and crystals typically pack with a herringbone motif as shown in figure 5.1.

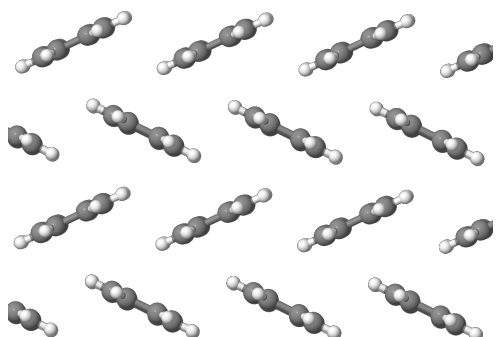


Figure 5.1: An example of the herringbone packing typically found in Pentacene crystals

5.1 Creating Amorphous Pentacene

In order to create the amorphous pentacene systems a melt-quench technique was used. This is a standard technique, often used to create amorphous systems in both computational and experimental fields⁸³⁻⁸⁷. The procedure followed is shown in figure 5.2.

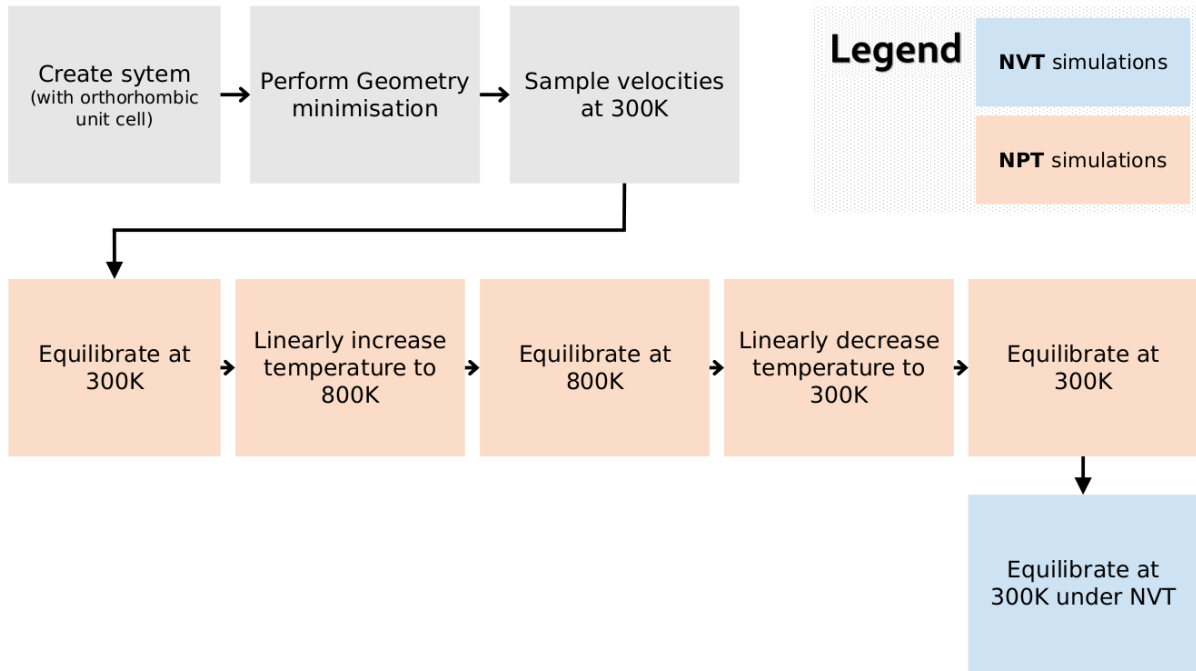


Figure 5.2: The melt-quench scheme used to create amorphous pentacene systems. Blue boxes indicate steps using an NPT ensemble, orange boxes indicate use of a NVT ensemble.

In this procedure, the system was initialised with an individual pentacene molecule on a regular 3D grid using an orthorhombic unit cell. This was chosen to make analysis of the resulting structures easier than with the triclinic unit cell typically used to simulate pentacene crystals. The velocities were initially randomly sampled from a gaussian distribution and a Nose-Hoover thermostat and barostat was used to control the temperature and pressure. The Lammmps molecular dynamics package was used^{88,89} and electrostatic interactions were handled with Lammmps' particle-particle-particle-mesh ewald method⁹⁰. RESP⁹¹ (restrained electrostatic potential) partial charges were parameterised using Gaussian 16⁹² with the B3-LYP level of theory and a 6-311g(d) basis set. The use of partial charges was essential in the creation of the amorphous systems and will be discussed further in section 5.4.1. Finally, for inter and intra molecular interactions the general AMBER force-field⁹³ (GAFF) was applied. There doesn't seem to be one predominant

forcefield to use in simulations of pentacene though parameters from GAFF have been used in a number of studies^{94–100}.

Four different quenching times were used spanning 4 orders of magnitude: 0ns, 1ns, 10ns and 100ns. For the 0ns, 1ns and 10ns quenching simulations 3,000 molecules were simulated. In the 100ns quenched structure 3060 molecules were simulated. The initial structure for the 1ns and 10ns quenched structures were taken from a restart of the 0ns quenched simulation after the 800K equilibration step. The 0ns and 1ns quenched structure were carried out under 1 atmosphere of pressure in x, y and z. However, the 10ns quenching required a small increase to 5 atmospheres as the structure had a tendency to deform such that one of the cell vectors became either very large or very small. In the 100ns quenched structure I updated the barostat target pressure (before the phase transition) to account for similar deviations in simulation box dimensions.

5.2 Structure of the quenched simulations

A movie showing the full 100ns melt-quench simulation can be found here: <https://youtu.be/6IQcYErQHVs>. Still images of the final snapshot of each different quenching time are shown in figure 5.3.

5.2.1 Final Structure Snapshots

We can see qualitatively that as we increase the quenching time from a) → d) the structure starts to look more ordered and crystal layers are starting to be formed. Looking longer at the structure we see that lower quench times tend to form small crystal clusters. In the 0ns quenched structure these clusters tend to be just ~7-10 molecules in size. As we increase the quenching time to 1ns we see 1D channels of crystalline pentacene start to form throughout the structure, though the structure is still relatively disordered due to these channels being randomly oriented with respect to one another. As we increase the quenching time these crystal fragments become larger until in the 100ns quenched structure the whole system is comprised of just 2 crystals. The reason for this is, as we decrease the rate of cooling (increase quench time) we also decrease the rate of crystals being seeded. This allows any crystals that have formed to grow larger without being

impeded by the growth of any other crystals. This can most clearly be seen in the animation of the [100ns melt quench simulation](#) linked above.

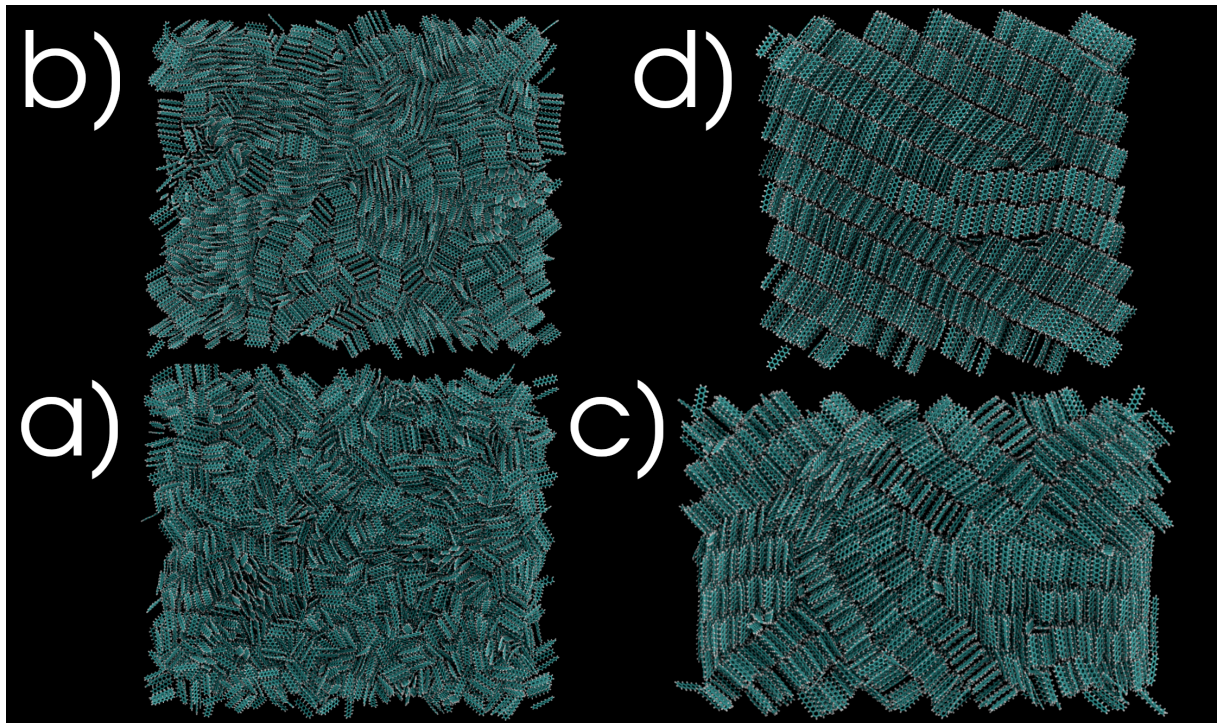


Figure 5.3: The final snapshot of each quenching simulation visualised in VMD⁴ and rendered with Tachyon⁵. Snapshots are ordered by quenching time i.e. a) is the 0ns quench, b) is the 1ns quench and so on.

5.2.2 Molecular Packing

We can isolate clusters in each of the different structures shown in figure 5.3 to reveal the molecular packing within. In figure 5.4 a DBSCAN-like algorithm has been applied to the final structure from the 100ns quench to cluster molecules based on the molecular density in a given region of space. These clusters have then been highlighted by different colours. The top-most green cluster has been rotated such that, on the left, we are viewing it at an angle perpendicular to the plane of molecules, as shown by the cartoon eye. Comparing this plane to the crystal plane to the right of it we can see a remarkable similarity in the packing motif. The herringbone packing has formed and (as can be seen in figure 5.7 in section 5.2.4) the herringbone intersection angle is remarkably similar to the crystal plane. This serves as a confirmation of the choice of force-field and the parameterisation of the partial charges.

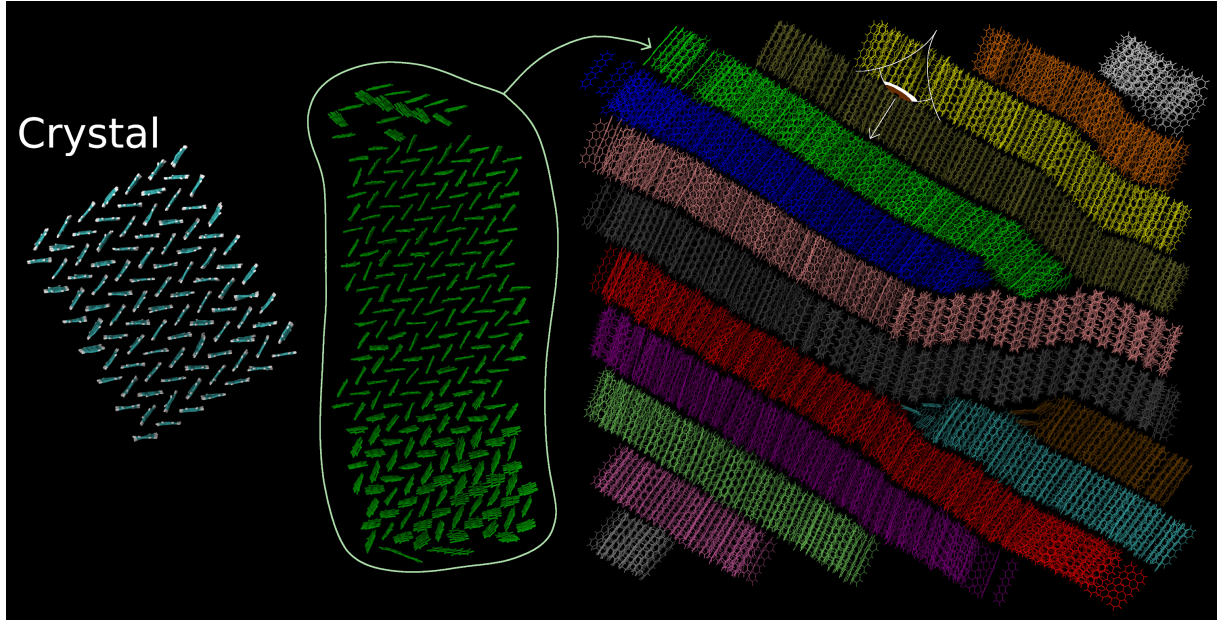


Figure 5.4: The 100ns quenched structure with different clusters shown with different colours. A bird's eye view of the green cluster has been shown on the left to demonstrate the herringbone packing within each cluster/layer. The far-right image labelled 'Crystal' is a snapshot of a crystal plane after a short MD equilibration.

Although this herringbone packing pattern is most obvious in the 100ns quenched structure, it can also be seen in the other structures. At the other extreme in the 0ns quenched structure we see small clusters (< 15 mols) of pentacene crystals forming. This is shown in figure 5.5. As the quench time increases these crystal fragments have more time to grow unimpeded by other crystals seeded nearby.

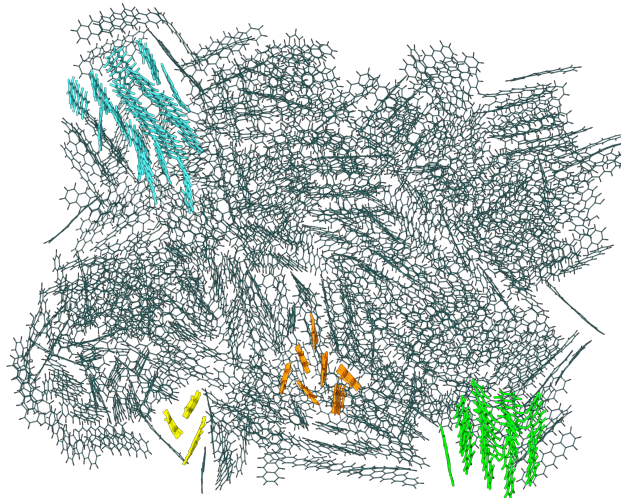


Figure 5.5: A slice from the 0ns quenched structure with selected clusters of herringbone-like packing highlighted.

To quantify the change in the structure for the differently quenched structures 4 macroscopic properties can be plotted: the mass density, the angular distribution, the radial distribution function and the orientational order parameter. These are discussed in the following sections.

5.2.3 Mass Density

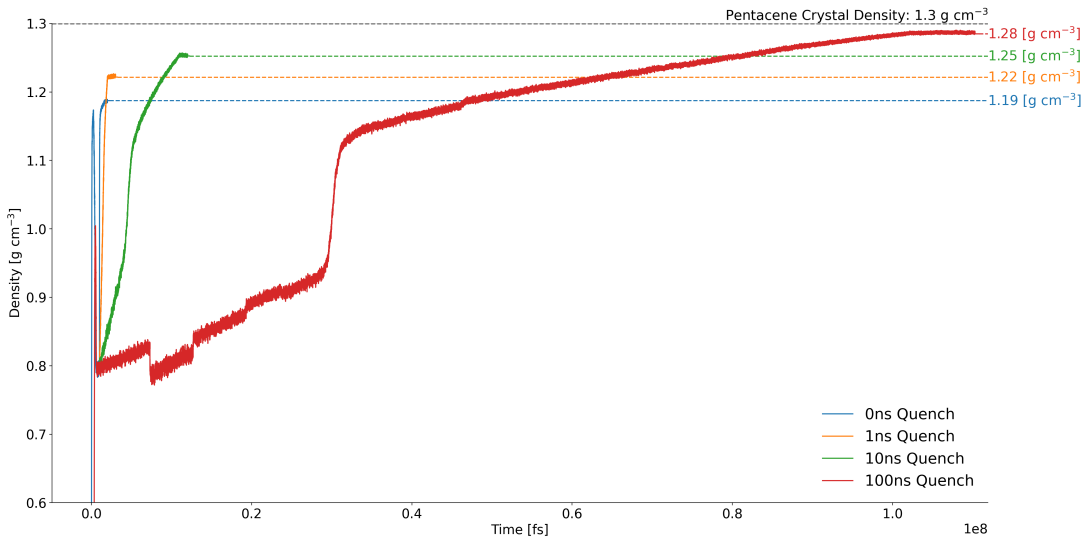


Figure 5.6: A time series of the density of the quenched structures. The black line shows the experimental mass density of crystal pentacene.

The mass density of the 4 different quenching simulations can be seen in figure 5.6. This was calculated by dividing the total mass of the atoms in the system by the volume (product of cell vectors) of the simulation box. The first thing to notice in this graph is as we increase the quenching time we increase the density of the final sample. This is due to the molecules packing more efficiently in the crystal than in an amorphous structure. We also see very clearly in the plots the sudden increase in density associated with the phase transition from liquid to solid Pentacene. In the 1ns quench structure (quenched with the barostat set to 1 atmosphere) this occurs around Pentacene's experimental melting of 530.15K¹⁰¹ providing confirmation of the choice of force-field. The 0ns, 1ns and 10ns runs were performed in a single 24 hour run. The 100ns quench was performed using many restarts, the discontinuities in the density for the 100ns structure come from these restarts. I don't believe they affect the final structure as these only occur while the system

is in the liquid state.

5.2.4 Angular Distribution

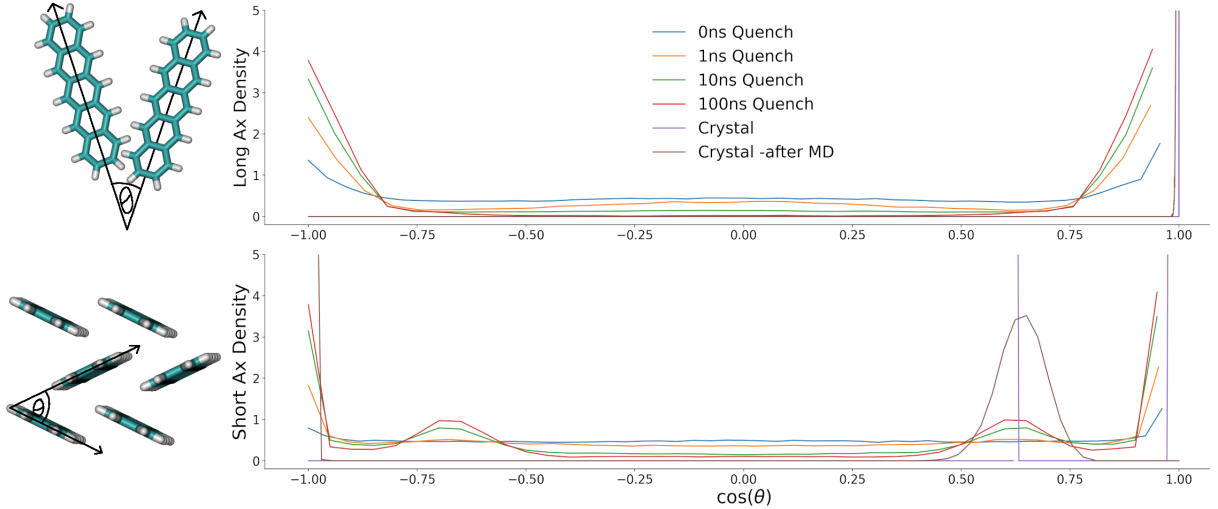


Figure 5.7: The angular distribution for the 4 different quench times is shown above. The brown and purple lines are from a perfect crystal before and after a short MD run. The others are after the various melt-quench simulations. On the right is a schematic showing which angles are referenced in each plot.

The angular distribution shows the distribution angles each molecule makes with the other molecules in the system. In figure 5.7 it was calculated by calculating the angle of an axis of each molecule with its nearest neighbours (a 20Å center of mass cutoff was used). This data was then grouped into a histogram which is plotted. In figure 5.7 we can see as the quenching time increases we start to notice an ever more prominent peak appear at either extreme of the x axis. This is because the molecules are aligning parallel with one another. The symmetry of the plot is an artefact of the melt stage of the simulation were each molecule was free to rotate randomly.

If we now look at the short axis plot we can see that, again, as the quench time increases we start to see a more ordered structure start to form. This time the herringbone intersection angle between molecules (54.3° ¹⁰²) within the herringbone structure is retrieved. This is a result of using partial charges in the simulation -running the same simulations without partial charges results in an unrealistic face-to-face stacking. The brown and purple line show the same calculation run on a crystal of pentacene before and

after MD. The purple line comes from an analysis of a repeated unit cell, hence we get 2 delta functions: one at 54.3° and one at 0° . This structure was then equilibrated with electrostatics for 50ps and we start to see a broadening of the herringbone intersection angle and to a lesser extent (on the left side) a broadening of the angle between parallel pairs.

5.2.5 Radial Distribution Function

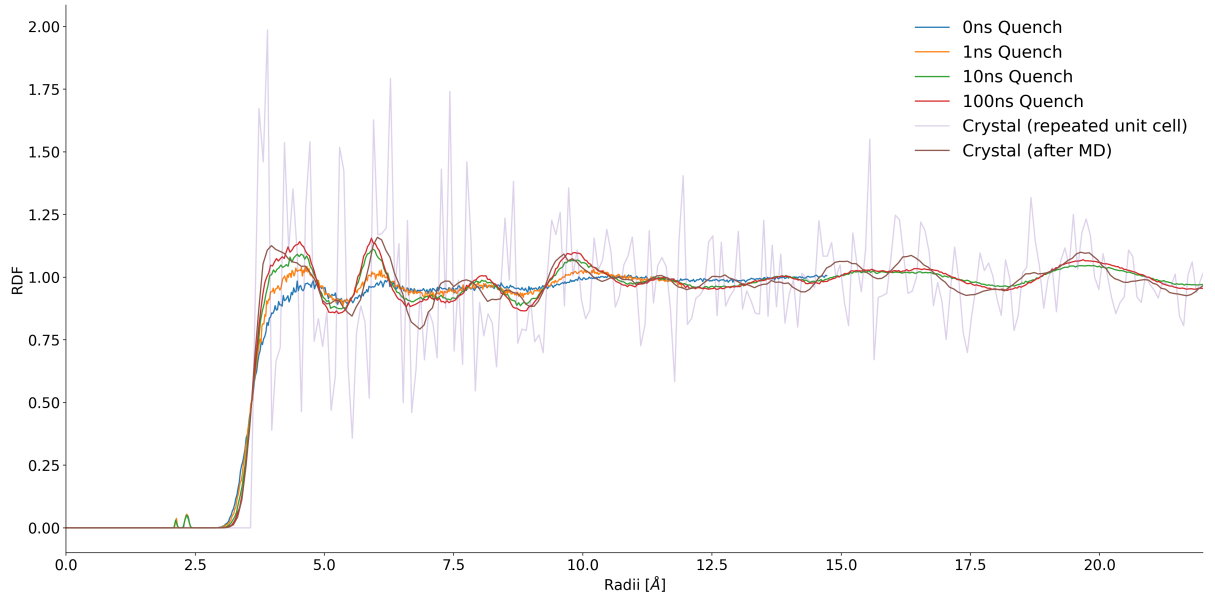


Figure 5.8: The carbon-carbon radial distribution function for 4 different quenching times and a crystal before and after 50ps of MD. The quenches (0, 1, 10 and 100ns) are shown in blue, orange, green and red respectively. The crystal data are shown in purple and brown.

The radial distribution function (RDF) describes the change of density from each particle in the system and is normalised to the bulk density (i.e. $\frac{N}{V}$). This was calculated by counting the number of atoms within a spherical shell from each atom and then dividing by the volume between these spheres. This local density was then normalised to the bulk crystal density. In systems with atoms regularly placed throughout the system we would expect to see sharp peaks in the RDF as there would be many gaps with no atoms. Conversely, with a totally amorphous system we would expect to see (once we reach twice the Van der Waals radius from each atom) a flat line at 1 as local density should be very similar to the global density. This pattern is what we observe in figure 5.8. The sharp

peaks of the purple line show the RDF of a perfect crystal (repeated unit cell) confirming we have a highly ordered system. On the other extreme the blue line shows very weak ordering of the atoms' positions with any ordering vanishing after $\sim 12.5\text{\AA}$ from each atom. This is due to the 0ns structure comprising primarily of small crystal fragments giving rise to a small amount of very local order but over longer distances this order vanishes. Again, as the quench time increases, the ordering increases resulting in larger peaks that more closely match the RDF of the crystal after a short MD equilibration.

5.2.6 Orientational Order Parameter

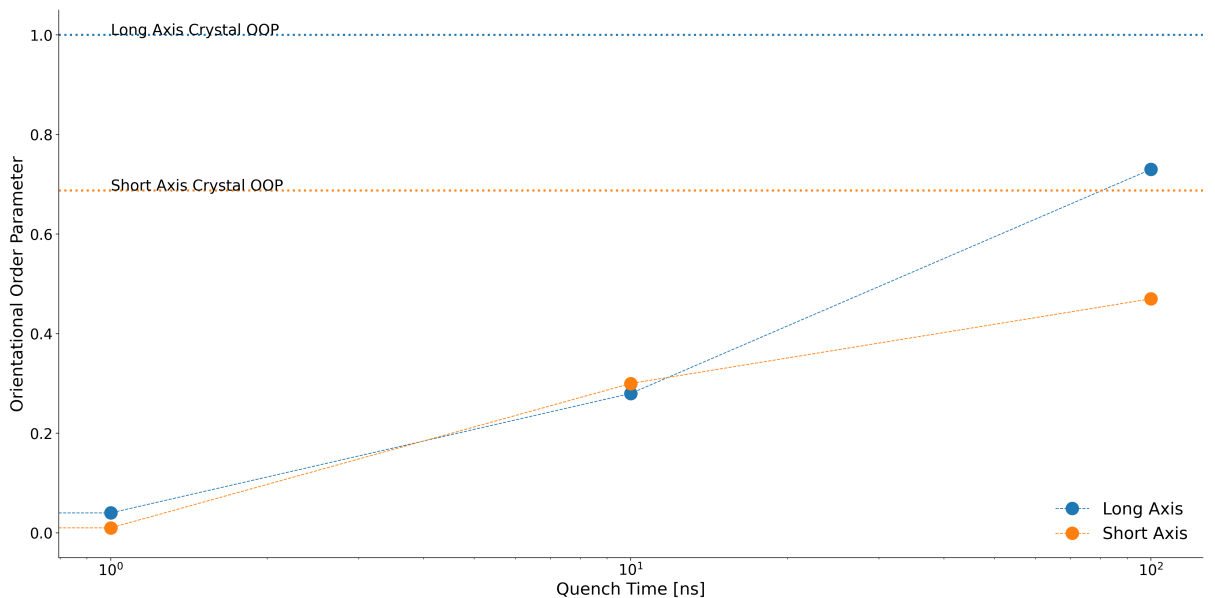


Figure 5.9: The change in the orientational order parameter (OOP) with respect to the quenching time. The blue data represents the values for the long axis and the orange data represents the short axis values. The horizontal lines show the theoretical value for a perfect crystal.

The orientational order parameter gives a single number describing how aligned the molecules within a system are. Values lie on a scale from -0.5 to 1, where 1 denotes all molecules are aligned, 0 denotes a random alignment of molecules and -0.5 denotes an anti-alignment with respect to the reference vector. The formula for the orientational order parameter is given below in equation (5.1).

$$S = \frac{3}{2} \frac{1}{N_{mol}} \sum_i^{N_{mol}} \left[\frac{\mathbf{v}_i \cdot \mathbf{v}_{ref}}{|\mathbf{v}_i| |\mathbf{v}_{ref}|} \right]^2 - \frac{1}{2} \quad (5.1)$$

Where \mathbf{v}_i is the vector describing the long or short axis of molecule i. The reference vector \mathbf{v}_{ref} was defined as the average over \mathbf{v}_i i.e: $\mathbf{v}_{ref} = \langle \mathbf{v}_i \rangle_i$. N_{mol} is the number of molecules and i indicates a molecule index.

In figure 5.9 we can see the change in the orientational order parameter with quenching time and, as seen in the previous sections, as we increase the quenching time we increase (orientational) order in the system.

5.3 Charge Transfer Properties

We have seen that the final structure of the pentacene systems becomes more ordered and crystal-like as the quenching time is increased. It would be good now to see how this affects the charge transfer properties. A key quantity governing charge transfer rates is the ratio between electronic coupling and reorganisation energy, $\frac{H_{ab}}{\lambda}$. Seeing as we have a single molecule system, by plotting the electronic coupling we can get a qualitative view of the charge transfer dynamics and see which paths are the most likely within the structure.

5.3.1 Global Couplings

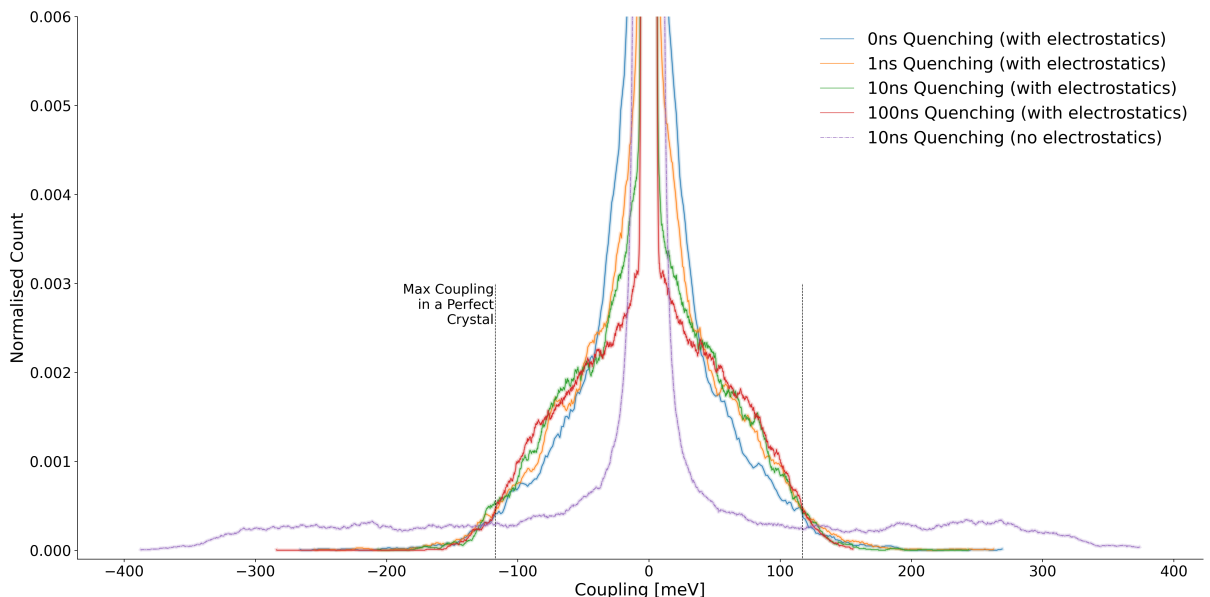


Figure 5.10: The global coupling distribution for each of the quenched structures (in blue, orange, green and red) and 1 structure after a 10ns quench without using electrostatics (purple line). The black dashed lines represent the maximum coupling within a perfect pentacene crystal.

The global coupling distribution gives an overview of the values of coupling within the system, hence an idea of the charge transport properties of the system. To calculate these couplings I have used the analytic overlap method (AOM)⁵⁸ to calculate couplings between all pairs of molecules (using a nearest neighbour cutoff) in the final snapshot of each quenched system. As can be seen from figure 5.10 as the quench time increases a knee starts to form in the distribution at a high coupling value (80meV), this is es-

pecially obvious in the 100ns quench structure (red curve). The figure also highlights the importance of electrostatics in the formation of the correct structure. The purple line shows the coupling distribution for the same simulation except electrostatics were switched off. In this curve we see far more very high values of coupling -substantially higher than those seen in the perfect crystal. This is due to it now being favourable to form a more tightly packed face-to-face structure giving rise to larger molecular overlaps hence higher couplings.

5.3.2 Coupling Graphs

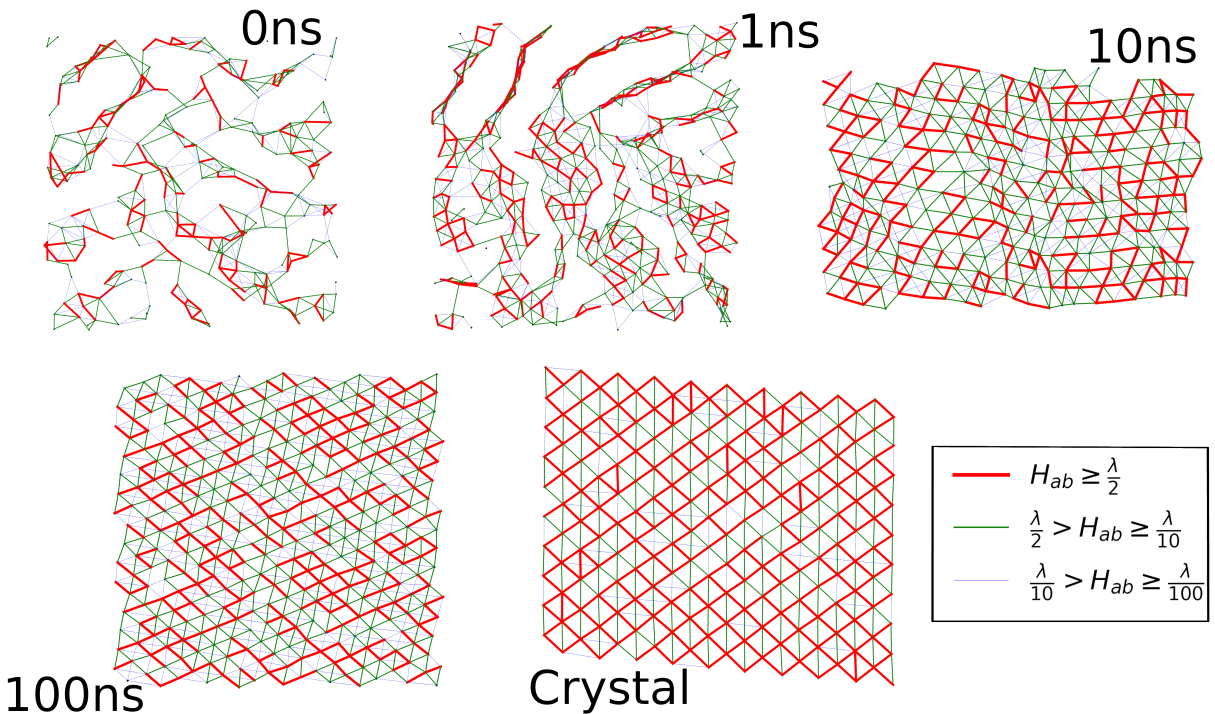


Figure 5.11: A representative network of electronic coupling that each quenched structure has formed. Each structure is labelled by the quench time (e.g. 0ns, 1ns, 10ns) or Crystal for a crystal after a short MD equilibration. Coupling strengths are categorised as high (red), medium (green) and low (blue). The definitions of the categories are given in the legend in the bottom right corner.

In figure 5.11 the graph of electronic couplings between molecules has been plotted for each of the quenched systems and a crystal system after a short equilibration run with MD. In this figure the centers of mass each molecule is represented by a small black dot and the calculated coupling value with a coloured line (red, green blue). That is, if 2 molecules have a non-negligible coupling between them they would be represented by 2

black dots with either a red, green or blue line connecting them. The couplings were calculated via the analytic overlap method⁵⁸ and a pertinent cluster of molecules was selected for each quench time. For the 0ns and 1ns quench times this was simply a slice 1 molecule thick in the z dimension, containing a few hundred molecules. For the 10ns and 100ns quenched structures a reasonable cluster of molecules was chosen after applying a density based clustering algorithm on the superstructure. For the crystal a plane from the crystal was chosen. All panes in figure 5.11 show the coupling of the selected system from an angle perpendicular to the plane of molecules.

We can see in the graph of the 0ns quenched structure there is very little order to the coupling network. Only very small fragments of high (red) coupling are formed and each one is connected via weak or medium coupling. We can define a 'high coupling fragment' as any set of molecules which can all be reached from any member of the set via an unbroken path of high coupling. The mean size of these high coupling fragments in the 0ns structure is 4.1 molecules and there are 503 of them. In this structure we would expect to see a localised polaron (over a ~ 3 molecules) and low mobilities due to the lack of conductive channels in the structure. The mean size of fragments increases and the number of fragments decreases as we increase the quenching time as shown in table 5.1.

Quench Time [ns]	Mean Fragment Size	Fragment Size Std Dev	Num Fragments
0	4.2	3.8	503
1	4.5	5.0	493
10	6.5	9.3	373
100	8.7	16.2	292

Table 5.1: The change in the number of high coupling fragments, and the mean and standard deviation of their size, found in each structure as the quenching time was varied.

We can see in table 5.1 that as the quenching time increases, the size of the highly coupled fragments (how many molecules are connected) increases and fewer of them are formed. The standard deviation also increases showing in the 0ns quenched structure

most fragments are very small but as we increase the quench time we still get smaller fragments but much larger ones can now form too. These larger fragments can act as regions of high conductivity allowing much larger mobilities to be achieved than in the quicker quenching times.

5.3.3 Hole Mobilities

To properly quantify the charge transfer dynamics the electron-hole mobility can be calculated on the output of a surface hopping simulation. A full discussion of the calculation of the electron mobility can be found here in Giannini, 19¹⁴. The mean squared displacement (MSD) of the charge carrier wavefunction was calculated and the gradient found by fitting a straight line to this. The gradient of the MSD, which is proportional to the Einstein diffusion coefficient D , was then used to calculate the mobility as in equation (5.2) below.

$$\mu_{ij} = \frac{eD_{ij}}{k_B T} \quad (5.2)$$

Where D_{ij} represents the Einstein diffusion coefficient, k_B is the Boltzmann constant, e the elementary charge and T is the temperature.

5.3.4 Simulation Set up

The surface hopping simulations require a swarm of hundreds of independent trajectories (~ 200), each with slightly different positions and velocities to fully sample phase space. The code currently does not support electrostatic interactions, so, in order to maintain the structure from the molecular dynamics simulations, center of mass restraints were used on each molecule. The restraint set up for 1 molecule is shown in figure 5.12. Here each of the 4 coloured zig-zag shapes show which atoms are restrained. These atoms were restrained about their center of mass. This configuration of restraints was used in order to

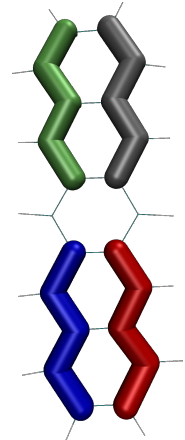


Figure 5.12: The restraint set up for 1 molecule. Each coloured zig-zag shows the atoms that are restrained.

stop rotations about the long axis for each molecule as this would allow molecules to form a face-to-face stacking giving rise to unphysically high couplings. The restraint strength was chosen to be the same as in another group members study to allow for a fair comparison of results. A short MD equilibration was performed to determine whether the restraint spring constant was sufficient to hold the molecules in place well enough to prevent the very high couplings appearing in the global coupling distribution. To further validate the choice of restraint/general set up a surface hopping simulation was carried out on a layer of bulk crystal and the mobilities were compared to known values.

In order to obtain initial positions and velocities for the individual trajectories an MD equilibration was carried out using the restraint set up. This was carried out for 220ps using the NVE ensemble. The first 4ps were discarded and positions and velocities were then sampled every 1ps in order to get 216 trajectories. When these 216 trajectories were created, the Hamiltonian was calculated for each. This allowed an adiabatic state to be selected which, when transformed to the diabatic basis gave a population close to the center of the system and had an energy within 3KT of the ground state energy. An explanation of how this was done is given in appendix H. In short the method consisted of finding the adiabatic energy (eigenvalue) and diabatic populations (eigenvector) corresponding to adiabatic state n which yielded a state both close to the center and within approximately 3KT of the ground state energy. This was done to ensure a quick convergence of the mean squared displacement of the charge carrier. The surface hopping simulations were then carried out with initial positions and velocities coming from the NVE equilibration run and the initial wavefunction being selected as mentioned above. Other parameters were taken from previous surface hopping simulations carried out by other members of the group.

5.3.4.1 0ns and 1ns Systems

The selection of the region for each surface hopping simulation was important in order to get a fair representation of the mobilities achievable within each structure. In the 0ns and 1ns quenched structures 6 slices were selected from the final snapshot of the structure. These were chosen to be independent clusters evenly spaced to sample

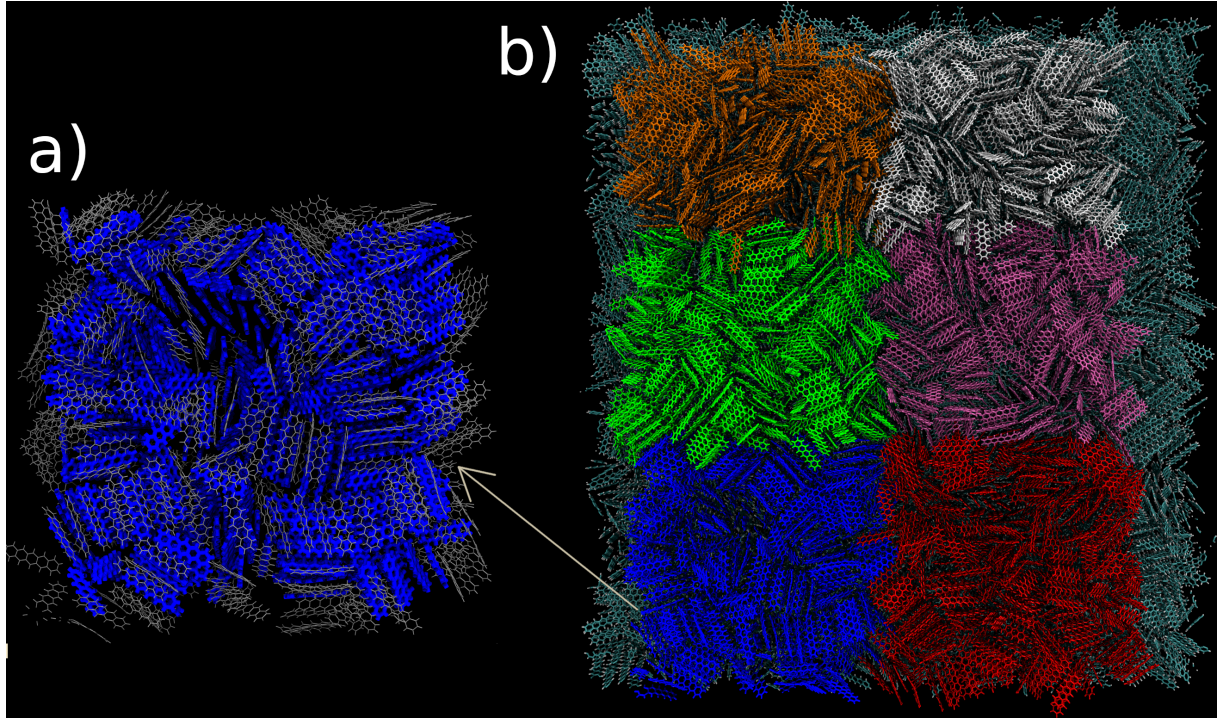


Figure 5.13: Panel a) shows a system chosen to run surface hopping on, molecules in gray are fixed in place blue molecules show the active region. Panel b) shows every sub-structure chosen in the 0ns quenched structure.

the mobility of the structure at various points. The selections are shown in figure 5.13 for the 0ns quenched structure. The same process was used in the 1ns quenched structure.

In order to preserve the structure and maintain energy conservation a shell of inactive molecules was selected from the superstructure to surround the active region. The atoms within this remained fixed to their position at $t=0$.

5.3.5 100ns System

The 100ns system is a much more ordered system and forms very well defined layers. This makes picking out structures on which to run surface hopping different to the 0/1ns quenched structures. The method I used was to first extend the superstructure in the z axis by $\pm 45\text{\AA}$ by repeating the periodic image and discarding molecules more than $\pm 45\text{\AA}$ from the simulation box boundaries. This was to ensure the resulting system was sufficiently large to converge mobilities. This added approximately 1 extra periodic image in the +ve and -ve z direction. A density based clustering algorithm (similar to

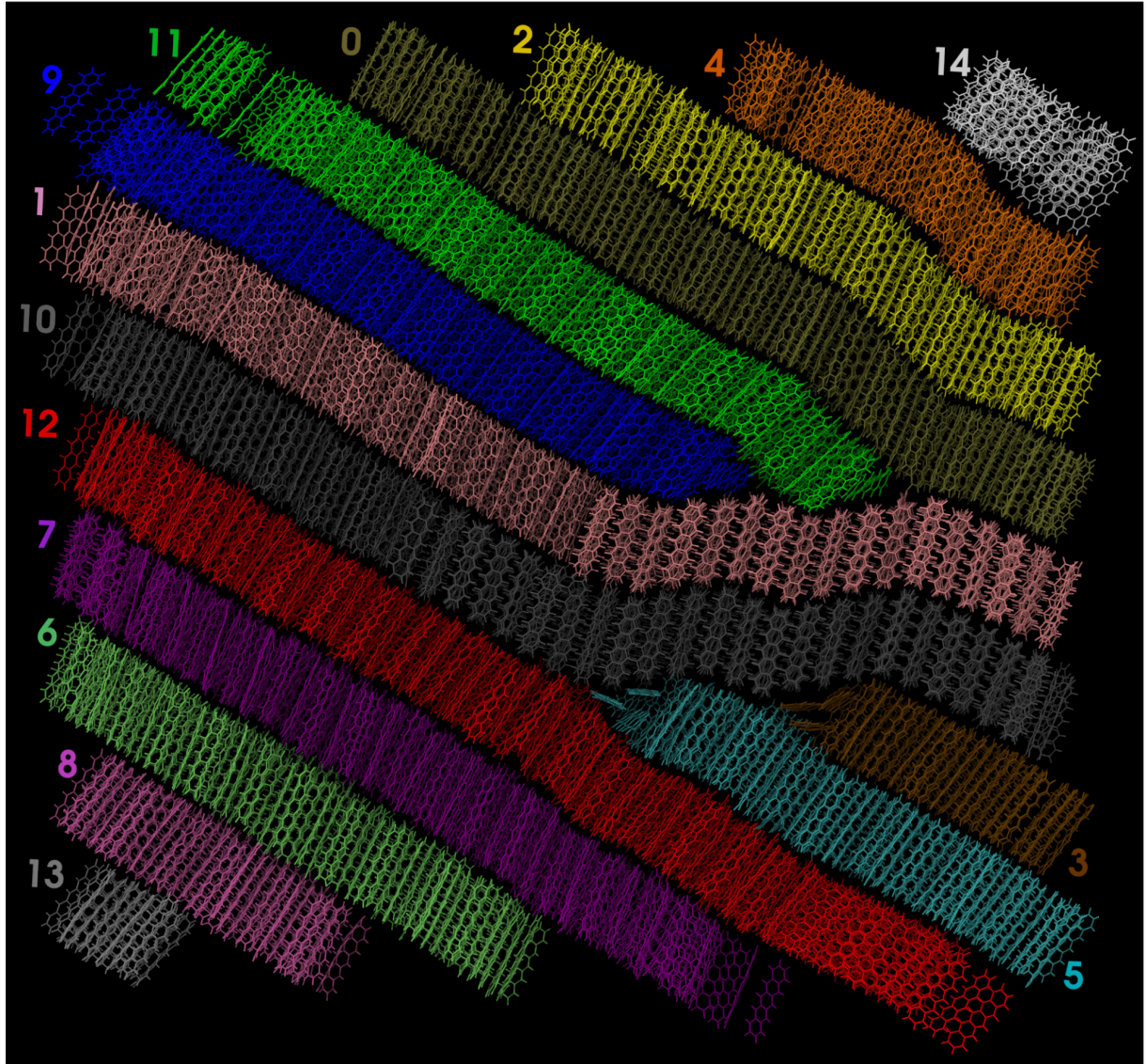


Figure 5.14: The 100ns quenched structure clustered by layer. Each different colour represents a different cluster, labelled with the numbers around the edge of the structure.

DBSCAN¹⁰³) was used to isolate the layers in the full structure by clustering centers of mass. These are shown in figure 5.14. In this figure clusters 6, 7 and 11 were chosen to calculate the mobility via surface hopping.

5.3.6 10ns System

The choice of region within the 10ns quenched structure was different from the 0/1ns and the 100ns quenched structure. Here we have some large crystal fragments forming but still very few well defined layers. In this system the mobility is expected to be much more dependant on the initial position of the charge carrier within the structure than in the 0ns and 100ns quenched structure where the structure was more uniformly disordered or ordered respectively. In order to sample a reasonable range of mobilities in this structure 4 clusters were selected shown in fig 5.15. 3 of these (red, blue and purple) were selected using a similar clustering procedure as in the 100ns quenched structure. The center-right green cluster was selected as it looked like it was a fairly disordered region where multiple crystal fragments meet, which would give a lower bound on the mobility within the 10ns structure.

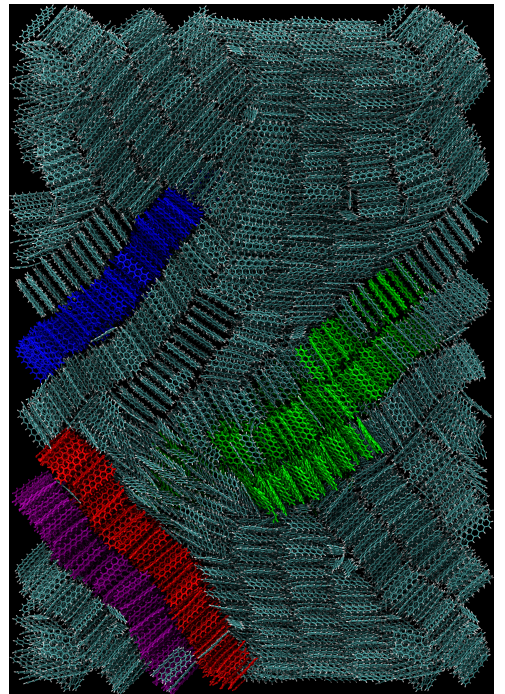


Figure 5.15: The clusters chosen to run surface hopping simulations on. The coloured clusters each represent a different structure on which surface hopping was ran.

5.4 Mobilities

5.4.1 Molecular Dynamics without Partial Charges

Chapter 6

Extending surface hopping with electrostatics

6.1 Electrostatics interaction within FOB-SH

FOB-SH is a variant of Tully's original fewest switches surface hopping (ref John Tully 1990 original surface hopping paper). The electron and nuclear dynamics are dictated by the Hamiltonian, where the spatial derivative of the diagonal elements (site-energies) give the nuclear forces which come from a classical forcefield and the off-diagonal elements (electron couplings) are proportional to the overlap of the diabatic wavefunctions. Each site-energy, $H_{\gamma\gamma}$, is defined as the potential energy of the system where the excess charge is localised on a single molecule, γ . The input parameters such as the charge distribution or the strength of the bonds are different for molecule γ than the other molecules, resulting in different forces/potentials. The different potentials from each permutation of the charge state are saved as the site-energies, the forces are saved in a different array of size $(N_{states}, N_{atoms}, 3)$. To implement electrostatic interactions the potential and the forces within the surface hopping framework will have to be altered.

To calculate the electrostatic contribution from each atom to the forces and potential the standard Ewald method was chosen, with some additional tricks to reduce the computational cost. The Ewald method, first published by Paul Ewald in 1921 (NEED REF), is a near ubiquitous method used to evaluate the potential and forces from a set of point charges. This is equivalent to carrying out the much slower to converge (NEED REF) and conditionally convergent traditional coulomb sum. The Ewald method relies

on separating the traditional coulomb summation into 2 quickly converging parts; a long range term and short range term. The short range term is carried out in real space and the long range term is carried out in reciprocal space

Chapter 7

General conclusions

Appendix A

Tully Model Paramters

A.1 Model 1 -Single Avoided Crossing

	Quantity	Value	Unit
Hamiltonian Paramters:			
$H_{11}(\mathbf{R}) = A \tanh(B\mathbf{R})$	Initial Position	-20	a.u.
$H_{12}(\mathbf{R}) = Ce^{-D\mathbf{R}^2}$	Initial Velocities	15.0, 25.0	a.u.
$H_{21}(\mathbf{R}) = H_{12}(\mathbf{R})$	Initial Adiab Pop	ground state	-
$H_{22}(\mathbf{R}) = -H_{11}(\mathbf{R})$	Simulation Time	6000, 4000	a.u.
Where $A = 0.03$, $B = 0.4$, $C = 0.005$ and $D = 0.3$	$\sigma_v^{(I)}$	0.5	a.u.
	M (σ constant)	40	-
	$\Delta t_{\text{nuclear}}$	0.1	fs
	$\Delta t_{\text{electronic}}$	0.01	fs
	$\frac{\delta \mathbf{R}_{lk,v}^{(I)}}{\delta t}$ threshold	0.15	a.u.
	N_{rep}	200	-

A.2 Model 2 -Dual Avoided Crossing

	Quantity	Value	Unit
Hamiltonian Paramters:			
$H_{11}(\mathbf{R}) = 0$	Initial Position	-8	a.u.
$H_{12}(\mathbf{R}) = Ce^{-D\mathbf{R}^2}$	Initial Velocities	16.0, 30.0	a.u.
$H_{21}(\mathbf{R}) = H_{12}(\mathbf{R})$	Initial Adiab Pop	ground state	-
$H_{22}(\mathbf{R}) = -Ae^{-B\mathbf{R}^2} + E$	Simulation Time	2500, 1500	a.u.
Where A = 0.1, B = 0.28, C = 0.015, D = 0.06 and E = 0.05	$\sigma_v^{(I)}$	0.5	a.u.
	M (σ constant)	40	-
	$\Delta t_{\text{nuclear}}$	0.1	fs
	$\Delta t_{\text{electronic}}$	0.01	fs
	$\frac{\delta \mathbf{R}_{ik,v}^{(I)}}{\delta t}$ threshold	0.15	a.u.
	N_{rep}	200	-

A.3 Model 3 -Extended Coupling

	Quantity	Value	Unit
Hamiltonian Paramters:			
$H_{11}(\mathbf{R}) = A$	Initial Position	-15	a.u.
$H_{12}(\mathbf{R}) = \begin{cases} Be^{C\mathbf{R}}, & R \leq 0 \\ B(2 - e^{-C\mathbf{R}}), & R > 0 \end{cases}$	Initial Velocities	10, 30	a.u.
$H_{21}(\mathbf{R}) = H_{12}(\mathbf{R})$	Initial Adiab Pop	ground state	-
$H_{22}(\mathbf{R}) = -H_{11}(\mathbf{R})$	Simulation Time	5000, 1500	a.u.
Where A = 6×10^{-4} , B = 0.1 and C = 0.9	$\sigma_v^{(I)}$	0.5	a.u.
	M (σ constant)	40	-
	$\Delta t_{\text{nuclear}}$	0.1	fs
	$\Delta t_{\text{electronic}}$	0.01	fs
	$\frac{\delta \mathbf{R}_{ik,v}^{(I)}}{\delta t}$ threshold	0.15	a.u.
	N_{rep}	200	-

A.4 Model 4 -Dual Arch

Hamiltonian Paramters:

$$H_{11}(\mathbf{R}) = A$$

$$H_{12}(\mathbf{R}) = \begin{cases} B \left[-e^{C(\mathbf{R}-D)} + e^{C(\mathbf{R}+D)} \right] & R \leq -D \\ B \left[e^{-C(\mathbf{R}-D)} - e^{-C(\mathbf{R}+D)} \right] & R \geq D \\ B \left[2 - e^{C(\mathbf{R}-D)} - e^{-C(\mathbf{R}+D)} \right] & -D < R < D \end{cases}$$

$$H_{21}(\mathbf{R}) = H_{12}(\mathbf{R})$$

$$H_{22}(\mathbf{R}) = -H_{11}(\mathbf{R})$$

Where $A = 6 \times 10^{-4}$, $B = 0.1$, $C = 0.9$ and

$$D = 4$$

Quantity	Value	Unit
Initial Position	-20	a.u.
Initial Velocities	10, 40	a.u.
Initial Adiab Pop	ground state	-
Simulation Time	6000, 2000	a.u.
$\sigma_v^{(I)}$	0.5	a.u.
M (σ constant)	40	-
$\Delta t_{\text{nuclear}}$	0.1	fs
$\Delta t_{\text{electonic}}$	0.01	fs
$\frac{\delta \mathbf{R}_{lk,v}^{(I)}}{\delta t}$ threshold	0.15	a.u.
N_{rep}	200	-

Appendix B

Wigner Distribution Derivation

The nuclear wavepacket (at time 0) is given by:

$$\chi(R) = \frac{1}{(\pi\mu^2)^{\frac{1}{4}}} e^{-\frac{(R-R_0)^2}{2\mu^2} + ik_0(R-R_0)} \quad (\text{B.1})$$

The Wigner quasiprobability function for momentum and position (p, R) is given by:

$$W(p, R) = \frac{1}{\pi\hbar} \int_{-\infty}^{\infty} \chi^*(R+y)\chi(R-y)e^{\frac{2ipy}{\hbar}} dy \quad (\text{B.2})$$

However, both Ehrenfest and CTMQC require atomic positions as input so we must extract the position and velocity probability densities from this. We get these from the marginal integrals of the Wigner distribution i.e.

$$|f(R)|^2 = \int_{-\infty}^{\infty} W(R, p) dp \quad (\text{B.3})$$

$$|f(p)|^2 = \int_{-\infty}^{\infty} W(R, p) dR \quad (\text{B.4})$$

In order to calculate these marginal integrals we must first crunch through the maths of equation (B.2). Substituting eq (B.1) into (B.2):

$$W(p, R) = \frac{1}{\pi\hbar} \int_{-\infty}^{\infty} \frac{1}{\mu\sqrt{\pi}} e^{-\frac{(R+y-R_0)^2}{2\mu^2} - 2ik_0y - \frac{(R-y-R_0)^2}{2\mu^2}} e^{\frac{2ipy}{\hbar}} dy \quad (\text{B.5})$$

Simplifying the 2 quadratic equations (equation (B.5)) we get:

$$W(p, R) = \frac{1}{\pi \hbar} \int_{-\infty}^{\infty} \frac{1}{\mu \sqrt{\pi}} e^{-\mu^{-2}(y^2 - 2ik_0 y \mu^2 + (R-R_0)^2)} e^{\frac{2ipy}{\hbar}} dy \quad (\text{B.6})$$

We can now take the expressions not dependant on y outside of the integral and combine the exponents.

$$W(p, R) = \frac{1}{\pi \sqrt{\pi} \mu \hbar} e^{-\frac{(R-R_0)^2}{\mu^2}} \int_{-\infty}^{\infty} e^{-\frac{y^2 + 2iy\mu^2(\frac{p}{\hbar} - k_0)}{\mu^2}} dy \quad (\text{B.7})$$

Integrating we get:

$$\int e^{-\frac{y^2 + 2iy\mu^2(\frac{p}{\hbar} - k_0)}{\mu^2}} dy = \frac{\sqrt{\pi} \mu}{2} e^{-\frac{\mu^2}{\hbar^2}(p - \hbar k_0)^2} \operatorname{erf} \left[\frac{y}{\mu} + i \left(\frac{p\mu}{\hbar} - \mu k_0 \right) \right] \quad (\text{B.8})$$

Applying limits we get:

$$\int_{-\infty}^{\infty} e^{-\frac{y^2 + 2iy\mu^2(\frac{p}{\hbar} - k_0)}{\mu^2}} dy = \sqrt{\pi} \mu e^{-\frac{\mu^2}{\hbar^2}(p - \hbar k_0)^2} \quad (\text{B.9})$$

Substituting this back into the Wigner distribution (equation (B.2)) we finally get:

$$W(p, R) = \frac{1}{\pi \hbar} e^{-\frac{(R-R_0)^2}{\mu^2}} e^{-\frac{(p - \hbar k_0)^2}{\hbar^2/\mu^2}} \quad (\text{B.10})$$

Taking the marginal integrals we get the position and velocity probability distributions:

$$|f(R)|^2 = \frac{2}{\mu \sqrt{\pi}} e^{-\frac{(R-R_0)^2}{\mu^2}} \quad (\text{B.11})$$

$$|f(p)|^2 = \frac{2}{\frac{\hbar}{\mu} \sqrt{\pi}} e^{-\frac{\mu^2}{\hbar^2}(p - \hbar k_0)^2} \quad (\text{B.12})$$

The above distributions are randomly sampled to get initial atomic velocities and positions for each simulation.

Appendix C

$\mathbf{R}_{lk,v}$ Alternatives

C.1 $\mathbf{R}_{lk,v}$ Extrapolation

C.2 Alternative Quantum Momentum Intercept

In Agostini, 16² another quantum momentum intercept term is discussed. This term is not used because, as previously discussed in section 1.4, it leads to unphysical transfer of population between adiabatic states when the nonadiabatic coupling elements are 0. However, it can be used in these Tully Models as an effective fix to the discontinuities caused by the $\mathbf{R}_{lk,v}$ term.

The other quantum momentum intercept, $\mathbf{R}_{0,v}^{(I)}$, comes directly from the construction of the nuclear density using a linear combination of a product of gaussians (see equation (1.12) in the introduction). It is defined as in equation (C.1) below:

$$\mathbf{R}_{0,v}^{(I)} = \sum_{J}^{N_{tr}} \left[\frac{\hbar \prod_{v'} g_{\sigma_{v'}^{(J)}(t)} (\mathbf{R}_{v'}^{(I)}(t) - \mathbf{R}_{v'}^{(J)}(t))}{2 \sigma_v^{(J)}(t)^2 \sum_{K}^{N_{tr}} \prod_{v'} g_{\sigma_{v'}^{(K)}(t)} (\mathbf{R}_{v'}^{(I)}(t) - \mathbf{R}_{v'}^{(K)}(t))} \mathbf{R}_v^{(I)} \right] \quad (C.1)$$

However, as switching to this intercept directly may cause discontinuities in itself a smoothing parameter is applied to ease the switch. This is given in equation (C.2) below:

$$[1 - A(t)] R_{good}(t) + A(t) R_{bad}(t) = R_{effective}(t) \quad (C.2)$$

R_{good} refers to the intercept that should be switched to (e.g. for the detection of a spike in the $R_{lk,v}^{(I)}$ we switch to the intercept in in equation (C.1)). $R_{lk,v}^{(I)}$ refers to the intercept that is being switched from (e.g. when it is detected that the divergence of $R_{lk,v}^{(I)}$ has finished then we switch from the alternative intercept back to $R_{lk,v}^{(I)}$). $A(t)$ is a smoothing parameter and is given in equation (C.3) below:

$$A(t) = \frac{D_v^{(I)}}{2} \left[\tanh\left(t - \frac{t_{final} + t_{init}}{0.6Ndt}\right) + 1 \right] \quad (\text{C.3})$$

Where $D_v^{(I)}$ is the distance between the 2 intercepts (e.g. $D_v^{(I)} = R_{lk,v}^{(I)} - R_{0,v}^{(I)}$), N is the number of steps to take before settling solely on one intercept, t_{init} is the time of detection of the divergence, t_{final} is the time at which the code settles on 1 intercept and dt is the timestep taken.

A cartoon of this process is given in figure C.1

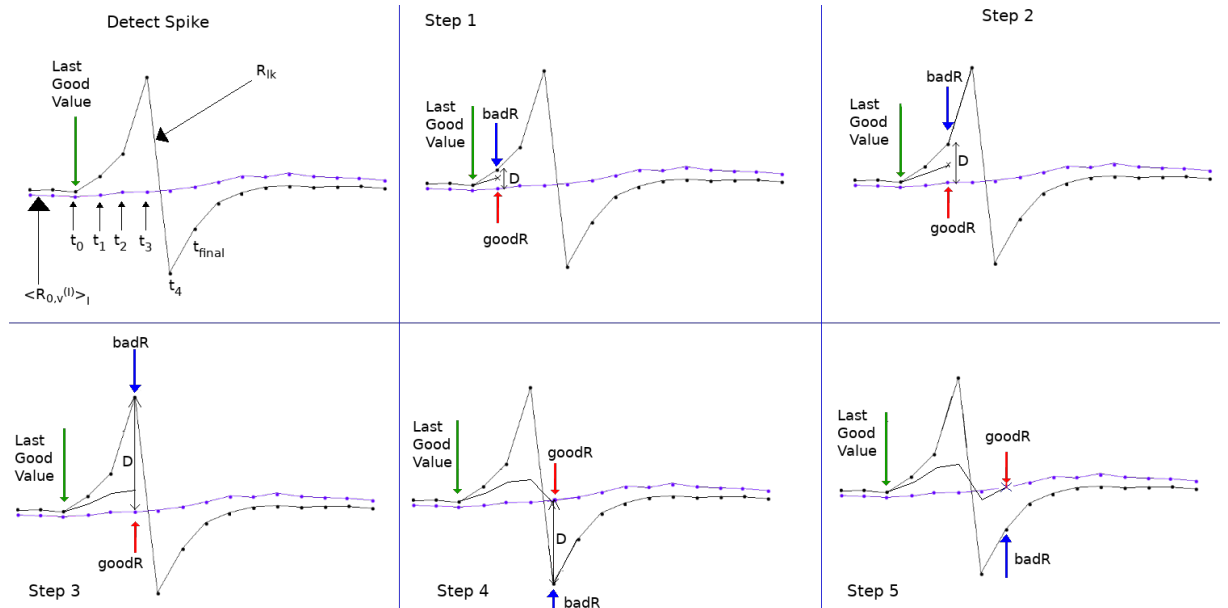


Figure C.1: A crude demonstration of the principle behind the smoothing procedure in switching between intercepts. The black line shows an intercept begin to diverge and the alternative intercept is shown in purple. As the step is incremented the amount of the alternative intercept that makes up the effective intercept is increased until only 1 intercept is used.

Appendix D

Rabi Oscillation

The time dependant Schrödinger equation is given below:

$$\hbar \frac{\delta}{\delta t} \Phi(\mathbf{R}(t), t) = \hat{H}(\mathbf{R}(t), t) \Phi(\mathbf{R}(t), t) \quad (\text{D.1})$$

If we hold the nuclear coordinates in place (e.g. remove time-dependence from nuclear coordinates) we get an ordinary differential equation as shown below:

$$\hbar \frac{d}{dt} \Phi(\mathbf{R}, t) = \hat{H}(\mathbf{R}, t) \Phi(\mathbf{R}, t) \quad (\text{D.2})$$

This has the following general solution. This can be solved with a Taylor series expansion.

$$\Phi(\mathbf{R}, t) = e^{\hbar \hat{H} t} \Phi(\mathbf{R}, 0)$$

Figure

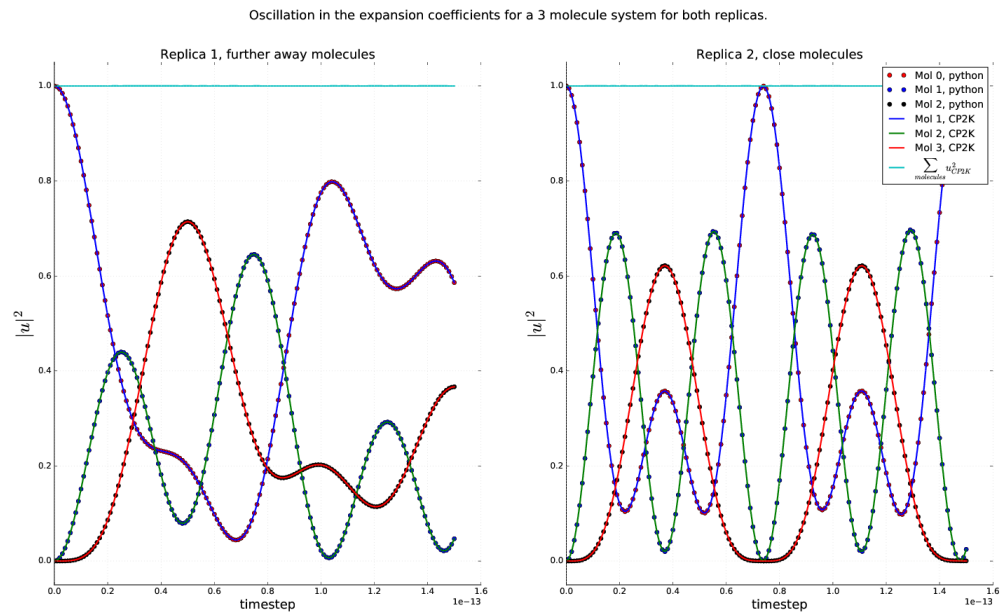


Figure D.1: Rabi oscillation occurring within a Ethylene trimer system. Dotted lines were calculated using equation (D.2), solid lines were calculated using the RK4 propagator within the CTMQC section of the CP2K code. The norm is shown on the top as a cyan line and the x axis shows the timestep in seconds.

Appendix E

Norm Conservation in CTMQC and Ehrenfest

A statement of the conservation of the norm, for a single trajectory, is given below in equation (E.1)

$$\frac{d}{dt} \sum_l |C_l(t)|^2 = \sum_l C_l^*(t) \frac{dC_l(t)}{dt} + \frac{dC_l^*(t)}{dt} C_l(t) = 2\mathbb{R} \left[\sum_l C_l(t)^* \frac{dC_l(t)}{dt} \right] \quad (\text{E.1})$$

Substituting the equation for the evolution of the adiabatic coefficients (and removing the purely imaginary term) into (??) we get equation (E.3)

$$\frac{d}{dt} \sum_l |C_l(t)|^2 = 2 \sum_l \mathbb{R} \left[\frac{-i}{\hbar} \cancel{\epsilon_{B\theta}^l} C_l(t)^* \cancel{C_l(t)} - \sum_k \left[C_l(t)^* C_k(t) d_{lk}^{ad} - (A_l - B_l) C_l(t)^* C_l(t) \right] \right] \quad (\text{E.2})$$

$$= -2 \sum_l \mathbb{R} \left[\sum_k \left[C_l(t)^* C_k(t) d_{lk}^{ad} - (A_l - B_l) C_l(t)^* C_l(t) \right] \right] \quad (\text{E.3})$$

Where:

$$A_l = \sum_{v=1}^{N_n} \sum_k \frac{\mathcal{Q}_{lk,v}(t)}{\hbar M_v} \cdot \mathbf{f}_{k,v}(t) |C_k(t)|^2 \quad (\text{E.4})$$

$$B_l = \sum_{v=1}^{N_n} \sum_k \frac{\mathcal{Q}_{lk,v}(t)}{\hbar M_v} \cdot \mathbf{f}_{l,v}(t) |C_k(t)|^2 \quad (\text{E.5})$$

The NACE term evaluates to 0 due to the anti-symmetry of the NACE giving us equation (E.7).

So far, we have proved that the norm should be conserved here for all terms apart from the quantum momentum terms i.e. Ehrenfest.

$$\frac{d}{dt} \sum_l |C_l^{QM}(t)|^2 = 2 \sum_l \Re[(A_l - B_l) C_l(t)^* C_l(t)] \quad (\text{E.6})$$

$$= 2 \left[\sum_l A_l |C_l(t)|^2 - \sum_l B_l |C_l(t)|^2 \right] \quad (\text{E.7})$$

However, $\sum_l A_l |C_l|^2 \equiv \sum_l B_l |C_l|^2$, therefore there is no change in the population and the norm should be conserved.

Appendix F

Dynamic σ Calculation

The algorithm for dynamically updating the σ parameter outlined in Gossel, 18³ is provided below.

1. Set an initial width parameter ($\sigma_v^{(I)}(t - dt)$) and a constant we will name D .
2. Calculate a cutoff distance via: $r_{cut}(t) = D\sigma_v^{(I)}(t - dt)$.
3. For each atom index, v , and replica, I , gather replicas within a cutoff distance of the current replica. Set the number of replicas within the cutoff distance to N .
4. Calculate the distance between atoms on different replicas.
5. Find the standard deviation of these distances and set the width of the gaussian, centered on atom v and replica I , to this standard deviation.
6. If the standard deviation is smaller than $\frac{D}{N} \min_I [\sigma_v^{(I)}(t - dt)]$ then set $\sigma_v^{(I)}(t) = \frac{D}{N} \min_I [\sigma_v^{(I)}(t - dt)]$.

Appendix G

Basis Transformation

We can expand the Schrödinger equation in terms of a diabatic basis, ϕ rather than an adiabatic one, ψ . These 2 expansions are given in equations (G.1) and (G.2).

$$|\Psi\rangle = \sum_n C_n |\psi_n\rangle \quad (\text{G.1})$$

$$|\Psi\rangle = \sum_l u_l |\phi_l\rangle \quad (\text{G.2})$$

It follows from this we can define a transformation matrix, U_{ln} to transform between the adiabatic and diabatic bases. This is shown in equation (G.3) where the $\overset{\leftrightarrow}{I}$ symbol represents the identity matrix. This identity only holds in the orthogonal diabatic basis ϕ and wouldn't hold for non-orthogonal bases.

$$|\psi_n\rangle = \overset{\leftrightarrow}{I} |\psi_n\rangle = \sum_l |\phi_l\rangle \langle \phi_l| \psi_n\rangle = \sum_l |\phi_l\rangle U_{ln} \quad (\text{G.3})$$

A similar relation between expansion coefficients exists

$$\sum_n C_n |\psi_n\rangle = \sum_l u_l |\phi_l\rangle \quad (\text{G.4})$$

$$\sum_n C_n \langle \psi_m | \psi_n \rangle = \sum_l u_l \langle \psi_m | \phi_l \rangle \quad (\text{G.5})$$

$$C_m = \sum_l u_l U_{lm}^* \quad (\text{G.6})$$

Finally an important property of the transformation matrix is given in equation (G.7).

$$\sum_m U_{im} U_{lm}^* = \sum_m \langle \phi_i | \psi_m \rangle \langle \psi_m | \phi_l \rangle = \langle \phi_i | \phi_l \rangle = \delta_{il} \quad (\text{G.7})$$

Equations (G.3), (G.6) and (G.7) will be used below to transform the propagation equations from the adiabatic basis to the diabatic one.

G.1 Forces

The equation for the propagation of the forces in the adiabatic basis is:

$$\begin{aligned} \mathbf{F}_v^{(I)} = & - \sum_n |C_n^{(I)}|^2 \nabla_v E_n^{(I)} - \sum_{n,m} C_m^{*(I)} C_n^{(I)} \left(E_n^{(I)} - E_m^{(I)} \right) \mathbf{d}_{v,mn}^{ad,(I)} \\ & - \sum_{m,n} |C_m^{(I)}|^2 \left(\sum_{v'}^{N_n} \frac{2}{\hbar M_{v'}} \mathcal{Q}_{v',mn}^{(I)} \cdot \mathbf{f}_{m,v'}^{(I)} \right) [\mathbf{f}_{n,v}^{(I)} - \mathbf{f}_{m,v}^{(I)}] |C_n^{(I)}|^2 \end{aligned} \quad (\text{G.8})$$

The quantum momentum part of the equation cannot be easily transformed so this will focus on the Ehrenfest part:

$$\mathbf{F}_{eh,v}^{(I)} = - \sum_n |C_n^{(I)}|^2 \nabla_v E_n^{(I)} - \sum_{n,m} C_m^{*(I)} C_n^{(I)} \left(E_n^{(I)} - E_m^{(I)} \right) \mathbf{d}_{v,mn}^{ad,(I)} \quad (\text{G.9})$$

Using equation (10) in Carof, 17⁶⁷ and the Hellman-Feynman theorem we can rewrite equation (G.9) as equation (G.10):

$$\mathbf{F}_{eh,v}^{(I)} = \sum_{m,n} C_m^{*(I)} C_n^{(I)} \langle \psi_m | \nabla_v H | \psi_n \rangle \quad (\text{G.10})$$

We can substitute the coefficients and basis functions for those in equations (G.3) and (G.6). This carried out in equation (G.15). However, I have removed the trajectory and

atom index from the terms to make the notation clearer.

$$F_{eh,v} = \sum_{m,n} C_m^* C_n \langle \psi_m | \nabla H | \psi_n \rangle \quad (\text{G.11})$$

$$= \sum_{m,n} \sum_i u_i^* U_{im} \sum_j u_j U_{jn}^* \sum_l U_{lm}^* \sum_k U_{kn} \langle \phi_l | \nabla H | \phi_k \rangle \quad (\text{G.12})$$

$$= \sum_{m,n} \sum_{i,j,k,l} u_i^* u_j U_{im} U_{lm}^* U_{jn}^* U_{kn} \langle \phi_l | \nabla H | \phi_k \rangle \quad (\text{G.13})$$

$$= \sum_{i,j,k,l} u_i^* u_j \delta_{il} \delta_{jk} \langle \phi_l | \nabla H | \phi_k \rangle \quad (\text{G.14})$$

$$= \sum_{i,j} u_i^* u_j \langle \phi_i | \nabla H | \phi_j \rangle \quad (\text{G.15})$$

However, in the code the expectation value of the gradient of the Hamiltonian ($\langle \phi_i | \nabla H | \phi_j \rangle$) isn't very easily calculable. However, the gradient of the Hamiltonian matrix elements ($\nabla \langle \phi_i | H | \phi_j \rangle$) is easily calculable via the overlap term, $\nabla H = C \nabla S_{ij}$. Therefore, using chain rule we can re-write equation (G.15) as:

$$F_{eh,v} = \sum_{i,j} u_i^* u_j \langle \phi_i | \nabla H | \phi_j \rangle \quad (\text{G.16})$$

$$= \sum_{i,j} u_i^* u_j (\nabla \langle \phi_i | H | \phi_j \rangle - \langle \nabla \phi_i | H | \phi_j \rangle - \langle \phi_i | H | \nabla \phi_j \rangle) \quad (\text{G.17})$$

$$= \sum_{i,j} u_i^* u_j \left(\nabla \langle \phi_i | H | \phi_j \rangle - \sum_l \langle \nabla \phi_i | \phi_l \rangle \langle \phi_l | H | \phi_j \rangle - \sum_l \langle \phi_i | H | \phi_l \rangle \langle \phi_l | \nabla \phi_j \rangle \right) \quad (\text{G.18})$$

$$= \sum_{i,j} u_i^* u_j \left(\nabla \langle \phi_i | H | \phi_j \rangle + \sum_l \mathbf{d}_{il} \langle \phi_l | H | \phi_j \rangle - \sum_l \mathbf{d}_{lj} \langle \phi_i | H | \phi_l \rangle \right) \quad (\text{G.19})$$

Giving the final equation for the transformed forces as:

$$\mathbf{F}_{eh,v}^{(I)} = \sum_{i,j} \mathbf{u}_i^{*(I)} \mathbf{u}_j^{(I)} \left(\nabla_v H_{ij}^{(I)} + \sum_l \mathbf{d}_{lk,v}^{(I)} H_{lj}^{(I)} - \sum_l \mathbf{d}_{lj,v}^{(I)} H_{il} \right) \quad (\text{G.20})$$

Appendix H

Adiabatic State Initialisation

By diagonalising the Hamiltonian we get the adiabatic energies (eigenvalues) for each state and transformation matrix (eigenvectors) to calculate diabatic states \mathbb{U} . We can calculate diabatic coefficients corresponding to each adiabatic state via equation (H.1) below.

$$\mathbb{U}\mathbf{C}_n = \mathbf{u}_n \quad (\text{H.1})$$

Where \mathbb{U} is the transformation matrix of size $(N_{\text{mol}}, N_{\text{mol}})$, \mathbf{C} is a complex vector of size N_{mol} containing coefficients for adiabatic state n and \mathbf{u} is a complex vector of size N_{mol} containing coefficients for diabatic state n .

Seeing as we would like to find the diabatic population corresponding to each adiabatic state we localise coefficients on each pure adiabatic state and carry out the transformation e.g: $C_i = (1+0i, 0+0i, 0+0i, \dots)$ when we want to find the diabatic coefficient corresponding to state 1 and $C_i = (0+0i, 1+0i, 0+0i, \dots)$ when we want to find the diabatic coefficient corresponding to state 2 etc.. Therefore, the column, n , of the transformation matrix, \mathbb{U} , gives the diabatic coefficients corresponding to adiabatic state, n , as shown below in equation (H.2)

$$U_{in} = u_i \quad (\text{H.2})$$

Where n is the adiabatic state index and i is the diabatic (molecular) state index.

Once we have the diabatic state corresponding to each adiabatic state, and the en-

ergy of that adiabatic state, we can find which state best fulfills the requirements of being close to the center of the system and being within $3KT$ of the ground state. In order to do this, we can loop over each adiabatic state in increasing order of energy. The center of the system is calculated and the population weighted average center of mass, \mathbf{R}_n of the diabatic coefficients corresponding to adiabatic state n is calculated as in equation (H.3).

$$\mathbf{R}_n = \sum_i |u_i|^2 \mathbf{R}_{COM,i} \quad (\text{H.3})$$

The Euclidean distance between the center of the system and $\mathbf{R}_{COM,i}$ is calculated and if this distance is below some threshold value then we initialise the surface hopping trajectory on that adiabatic state. If we do not find any states within $3KT$ of the ground state and within an acceptable radius of the center we start again this time increasing the maximum allowed distance from the center. If this maximum allowed distance is increased such that we reach another threshold distance the energy threshold is increased this time until a state is found that is close enough to the center. In this way we find an adiabatic state, which when transformed, gives a diabatic population close to center of the system and near the ground state energy.

Appendix I

Analytic Overlap Method

Appendix J

Colophon

This is a description of the tools you used to make your thesis. It helps people make future documents, reminds you, and looks good.

(example) This document was set in the Times Roman typeface using L^AT_EX (specifically LuaTeX) and BibTeX, composed with Vim Used Archer, Kathleen etc...

Bibliography

- [1] Federica Agostini, Ali Abedi, Yasumitsu Suzuki, Seung Kyu Min, Neepa T. Maitra, and E. K. U. Gross. The exact forces on classical nuclei in non-adiabatic charge transfer. *The Journal of Chemical Physics*, 142(8):084303, February 2015.
- [2] Federica Agostini, Seung Kyu Min, Ali Abedi, and E. K. U. Gross. Quantum-Classical Nonadiabatic Dynamics: Coupled- vs Independent-Trajectory Methods. *Journal of Chemical Theory and Computation*, 12(5):2127–2143, May 2016.
- [3] Graeme H. Gossel, Federica Agostini, and Neepa T. Maitra. Coupled-Trajectory Mixed Quantum-Classical Algorithm: A Deconstruction. *Journal of Chemical Theory and Computation*, August 2018.
- [4] William Humphrey, Andrew Dalke, and Klaus Schulten. VMD – Visual Molecular Dynamics. *Journal of Molecular Graphics*, 14:33–38, 1996.
- [5] John Stone. An Efficient Library for Parallel Ray Tracing and Animation. Master’s thesis, Computer Science Department, University of Missouri-Rolla, April 1998.
- [6] C. K. Chiang, C. R. Fincher, Y. W. Park, A. J. Heeger, H. Shirakawa, E. J. Louis, S. C. Gau, and Alan G. MacDiarmid. Electrical Conductivity in Doped Polyacetylene. *Physical Review Letters*, 39(17):1098–1101, October 1977.
- [7] Hideki Shirakawa, Edwin J. Louis, Alan G. MacDiarmid, Chwan K. Chiang, and Alan J. Heeger. Synthesis of electrically conducting organic polymers: halogen derivatives of polyacetylene, $(CH)_x$. *J. Chem. Soc., Chem. Commun.*, 0(16):578–580, Jan 1977.

- [8] Bernard Kippelen and Jean-Luc Brédas. Organic photovoltaics. *Energy Environ. Sci.*, 2(3):251–261, 2009.
- [9] M. J. Małachowski and J. Żmija. Organic field-effect transistors. *Opto-Electron. Rev.*, 18(2):121–136, Jun 2010.
- [10] N. Thejo Kalyani and S. J. Dhoble. Organic light emitting diodes: Energy saving lighting technology—A review. *Renewable Sustainable Energy Rev.*, 16(5):2696–2723, Jun 2012.
- [11] Sebastian Reineke, Frank Lindner, Gregor Schwartz, Nico Seidler, Karsten Walzer, Björn Lüssem, and Karl Leo. White organic light-emitting diodes with fluorescent tube efficiency. *Nature*, 459(7244):234, May 2009.
- [12] Kazuki Kato, Toshihiko Iwasaki, and Takatoshi Tsujimura. Over 130 lm/w all-phosphorescent white oleds for next-generation lighting. *Journal of Photopolymer Science and Technology*, 28:335–340, 10 2015.
- [13] Veaceslav Coropceanu, Jérôme Cornil, Demetrio A. da Silva Filho, Yoann Olivier, Robert Silbey, and Jean-Luc Brédas. Charge Transport in Organic Semiconductors. *Chemical Reviews*, 107(4):926–952, April 2007.
- [14] Samuele Giannini, Antoine Carof, Matthew Ellis, Hui Yang, Orestis George Ziogos, Soumya Ghosh, and Jochen Blumberger. Quantum localization and delocalization of charge carriers in organic semiconducting crystals. *Nature Communications*, 10(1):3843, Aug 2019.
- [15] Alessandro Troisi. Charge transport in high mobility molecular semiconductors: classical models and new theories. *Chem. Soc. Rev.*, 40:2347–2358, 2011.
- [16] Simone Fratini, Didier Mayou, and Sergio Ciuchi. The transient localization scenario for charge transport in crystalline organic materials. *Advanced Functional Materials*, 26(14):2292–2315, 2016.

- [17] I. Yavuz. Dichotomy between the band and hopping transport in organic crystals: insights from experiments. *Physical Chemistry Chemical Physics*, 19(38):25819–25828, 2017.
- [18] J. S. Brown and S. E. Shaheen. Introducing correlations into carrier transport simulations of disordered materials through seeded nucleation: impact on density of states, carrier mobility, and carrier statistics. *J. Phys.: Condens. Matter*, 30(13):135702, Mar 2018.
- [19] Tino Zimmerling and Bertram Batlogg. Improving charge injection in high-mobility rubrene crystals: From contact-limited to channel-dominated transistors. *Journal of Applied Physics*, 115(16):164511, 2014.
- [20] V. Podzorov, E. Menard, A. Borissov, V. Kiryukhin, J. A. Rogers, and M. E. Gershenson. Intrinsic charge transport on the surface of organic semiconductors. *Phys. Rev. Lett.*, 93:086602, Aug 2004.
- [21] Samuele Giannini, Antoine Carof, and Jochen Blumberger. Crossover from Hopping to Band-Like Charge Transport in an Organic Semiconductor Model: Atomistic Nonadiabatic Molecular Dynamics Simulation. *The Journal of Physical Chemistry Letters*, 9(11):3116–3123, June 2018.
- [22] Harald Oberhofer, Karsten Reuter, and Jochen Blumberger. Charge Transport in Molecular Materials: An Assessment of Computational Methods. *Chemical Reviews*, 117(15):10319–10357, August 2017.
- [23] John C. Tully. Nonadiabatic Dynamics. pages 34–71.
- [24] Simone Pisana, Michele Lazzeri, Cinzia Casiraghi, Kostya S. Novoselov, A. K. Geim, Andrea C. Ferrari, and Francesco Mauri. Breakdown of the adiabatic Born–Oppenheimer approximation in graphene. *Nat. Mater.*, 6(3):198, Feb 2007.
- [25] M. Born and R. Oppenheimer. Zur Quantentheorie der Moleküle. *Ann. Phys.*, 389(20):457–484, Jan 1927.

- [26] Sharon Hammes-Schiffer. Theoretical Perspectives on Proton-Coupled Electron Transfer Reactions. *Acc. Chem. Res.*, 34(4):273–281, Apr 2001.
- [27] Sharon Hammes-Schiffer and John C. Tully. Proton transfer in solution: Molecular dynamics with quantum transitions. *J. Chem. Phys.*, 101(6):4657–4667, Sep 1994.
- [28] My Hang V. Huynh and Thomas J. Meyer. Proton-coupled electron transfer. *Chemical Reviews*, 107(11):5004–5064, Nov 2007.
- [29] John C. Tully. Nonadiabatic molecular dynamics. *International Journal of Quantum Chemistry*, 40(S25):299–309, 1991.
- [30] Raymond Kapral and Giovanni Ciccotti. Mixed quantum-classical dynamics. *J. Chem. Phys.*, 110(18):8919–8929, May 1999.
- [31] Todd J. Martínez*. Insights for Light-Driven Molecular Devices from Ab Initio Multiple Spawning Excited-State Dynamics of Organic and Biological Chromophores. American Chemical Society, Oct 2005.
- [32] Guillermo Albareda, Heiko Appel, Ignacio Franco, Ali Abedi, and Angel Rubio. Correlated Electron-Nuclear Dynamics with Conditional Wave Functions. *Phys. Rev. Lett.*, 113(8):083003, Aug 2014.
- [33] John C. Tully. Molecular dynamics with electronic transitions. *J. Chem. Phys.*, 93(2):1061–1071, Jul 1990.
- [34] R. L et al Whetten. Molecular dynamics beyond the adiabatic approximation: New experiments and theory. *Ann. Rev. Phys. Chem.*, 36:277–320.
- [35] Neil Shenvi, Joseph E. Subotnik, and Weitao Yang. Simultaneous-trajectory surface hopping: A parameter-free algorithm for implementing decoherence in nonadiabatic dynamics. *J. Chem. Phys.*, 134(14):144102, Apr 2011.
- [36] D. F. Coker and L. Xiao. Methods for molecular dynamics with nonadiabatic transitions. *J. Chem. Phys.*, 102(1):496–510, Jan 1995.

- [37] Joseph E. Subotnik, Amber Jain, Brian Landry, Andrew Petit, Wenjun Ouyang, and Nicole Bellonzi. Understanding the surface hopping view of electronic transitions and decoherence. *Annual Review of Physical Chemistry*, 67(1):387–417, 2016. PMID: 27215818.
- [38] Giovanni Granucci, Maurizio Persico, and Alberto Zoccante. Including quantum decoherence in surface hopping. *The Journal of Chemical Physics*, 133(13):134111, 2010.
- [39] Heather M. Jaeger, Sean Fischer, and Oleg V. Prezhdo. Decoherence-induced surface hopping. *The Journal of Chemical Physics*, 137(22):22A545, 2012.
- [40] Amber Jain, Ethan Alguire, and Joseph E. Subotnik. An efficient, augmented surface hopping algorithm that includes decoherence for use in large-scale simulations. *Journal of Chemical Theory and Computation*, 12(11):5256–5268, Nov 2016.
- [41] Joseph E. Subotnik and Neil Shenvi. A new approach to decoherence and momentum rescaling in the surface hopping algorithm. *The Journal of Chemical Physics*, 134(2):024105, 2011.
- [42] Xiaosong Li, John C. Tully, H. Bernhard Schlegel, and Michael J. Frisch. Ab initio Ehrenfest dynamics. *J. Chem. Phys.*, 123(8):084106, Aug 2005.
- [43] Kenichiro Saita and Dmitrii V. Shalashilin. On-the-fly ab initio molecular dynamics with multiconfigurational Ehrenfest method. *J. Chem. Phys.*, 137(22):22A506, Dec 2012.
- [44] Daniela Kohen, Frank H. Stillinger, and John C. Tully. Model studies of nonadiabatic dynamics. *J. Chem. Phys.*, 109(12):4713–4725, Sep 1998.
- [45] John C. Tully. Perspective: Nonadiabatic dynamics theory. *The Journal of Chemical Physics*, 137(22):22A301, December 2012.
- [46] Priya V. Parandekar and John C. Tully. Detailed Balance in Ehrenfest Mixed Quantum-Classical Dynamics. *Journal of Chemical Theory and Computation*, 2(2):229–235, March 2006.

- [47] Ali Abedi, Neepa T. Maitra, and E. K. U. Gross. Exact Factorization of the Time-Dependent Electron-Nuclear Wave Function. *Physical Review Letters*, 105(12), September 2010.
- [48] Federica Agostini, Seung Kyu Min, and E. K. U. Gross. Semiclassical analysis of the electron-nuclear coupling in electronic non-adiabatic processes. *Annalen der Physik*, 527(9-10):546–555, October 2015.
- [49] Federica Agostini, Ali Abedi, Yasumitsu Suzuki, and E.K.U. Gross. Mixed quantum-classical dynamics on the exact time-dependent potential energy surface: a fresh look at non-adiabatic processes. *Molecular Physics*, 111(22-23):3625–3640, December 2013.
- [50] Ali Abedi, Federica Agostini, Yasumitsu Suzuki, and E. K. U. Gross. Dynamical Steps that Bridge Piecewise Adiabatic Shapes in the Exact Time-Dependent Potential Energy Surface. *Physical Review Letters*, 110(26), June 2013.
- [51] Seung Kyu Min, Ali Abedi, Kwang S. Kim, and E. K. U. Gross. Is the Molecular Berry Phase an Artifact of the Born-Oppenheimer Approximation? *Phys. Rev. Lett.*, 113(26):263004, Dec 2014.
- [52] Farnaz A. Shakib and Pengfei Huo. Ring Polymer Surface Hopping: Incorporating Nuclear Quantum Effects into Nonadiabatic Molecular Dynamics Simulations. *J. Phys. Chem. Lett.*, 8(13):3073–3080, Jul 2017.
- [53] Basile F. E. Curchod, Ivano Tavernelli, and Ursula Rothlisberger. Trajectory-based solution of the nonadiabatic quantum dynamics equations: an on-the-fly approach for molecular dynamics simulations. *PCCP*, 13(8):3231–3236, Feb 2011.
- [54] Ivano Tavernelli. Ab initio–driven trajectory-based nuclear quantum dynamics in phase space. *Phys. Rev. A*, 87(4):042501, Apr 2013.
- [55] Arne Scherrer, Federica Agostini, Daniel Sebastiani, E. K. U. Gross, and Rodolphe Vuilleumier. Nuclear velocity perturbation theory for vibrational circular dichroism:

- An approach based on the exact factorization of the electron-nuclear wave function. *J. Chem. Phys.*, 143(7):074106, Aug 2015.
- [56] Seung Kyu Min, Federica Agostini, Ivano Tavernelli, and E. K. U. Gross. Ab Initio Nonadiabatic Dynamics with Coupled Trajectories: A Rigorous Approach to Quantum (De)Coherence. *The Journal of Physical Chemistry Letters*, 8(13):3048–3055, July 2017.
- [57] John C. Tully. Molecular dynamics with electronic transitions. *The Journal of Chemical Physics*, 93(2):1061–1071, July 1990.
- [58] Fruzsina Gajdos, Siim Valner, Felix Hoffmann, Jacob Spencer, Marian Breuer, Adam Kubas, Michel Dupuis, and Jochen Blumberger. Ultrafast Estimation of Electronic Couplings for Electron Transfer between -Conjugated Organic Molecules. *Journal of Chemical Theory and Computation*, 10(10):4653–4660, October 2014.
- [59] J. VandeVondele, J; Hutter. Gaussian basis sets for accurate calculations on molecular systems in gas and condensed phases. *The Journal of Chemical Physics*, 127(11).
- [60] J. Spencer, F. Gajdos, and J. Blumberger. FOB-SH: Fragment orbital-based surface hopping for charge carrier transport in organic and biological molecules and materials. *The Journal of Chemical Physics*, 145(6):064102, August 2016.
- [61] Joseph E. Subotnik. Augmented ehrenfest dynamics yields a rate for surface hopping. *The Journal of Chemical Physics*, 132(13):134112, 2010.
- [62] Steven L. Fiedler and Jussi Eloranta. Nonadiabatic dynamics by mean-field and surface-hopping approaches: energy conservation considerations. *Molecular Physics*, 108(11):1471–1479, 2010.
- [63] James Kirkpatrick. An approximate method for calculating transfer integrals based on the zindo hamiltonian. *International Journal of Quantum Chemistry*, 108(1):51–56, 2008.

- [64] Harald Oberhofer and Jochen Blumberger. Revisiting electronic couplings and incoherent hopping models for electron transport in crystalline c60 at ambient temperatures. *Phys. Chem. Chem. Phys.*, 14:13846–13852, 2012.
- [65] Alessandro Troisi and Giorgio Orlandi. Hole migration in dna: a theoretical analysis of the role of structural fluctuations. *The Journal of Physical Chemistry B*, 106(8):2093–2101, Feb 2002.
- [66] Adam Kubas, Felix Hoffmann, Alexander Heck, Harald Oberhofer, Marcus Elstner, and Jochen Blumberger. Electronic couplings for molecular charge transfer: Benchmarking cdft, fodft, and fodftb against high-level ab initio calculations. *The Journal of Chemical Physics*, 140(10):104105, 2014.
- [67] Antoine Carof, Samuele Giannini, and Jochen Blumberger. Detailed balance, internal consistency, and energy conservation in fragment orbital-based surface hopping. *The Journal of Chemical Physics*, 147(21):214113, December 2017.
- [68] Antoine Carof, Samuele Giannini, and Jochen Blumberger. Detailed balance, internal consistency, and energy conservation in fragment orbital-based surface hopping. *The Journal of Chemical Physics*, 147(21):214113, 2017.
- [69] Soumya Ghosh, Samuele Giannini, Kevin Lively, and Jochen Blumberger. Nonadiabatic dynamics with quantum nuclei: simulating charge transfer with ring polymer surface hopping. *Faraday Discuss.*, 221:501–525, 2020.
- [70] Antoine Carof, Samuele Giannini, and Jochen Blumberger. How to calculate charge mobility in molecular materials from surface hopping non-adiabatic molecular dynamics – beyond the hopping/band paradigm. *Phys. Chem. Chem. Phys.*, 21:26368–26386, 2019.
- [71] J. Spencer, F. Gajdos, and J. Blumberger. Fob-sh: Fragment orbital-based surface hopping for charge carrier transport in organic and biological molecules and materials. *The Journal of Chemical Physics*, 145(6):064102, 2016.

- [72] Jacob Spencer, Laura Scalfi, Antoine Carof, and Jochen Blumberger. Confronting surface hopping molecular dynamics with marcus theory for a molecular donor–acceptor system. *Faraday Discuss.*, 195:215–236, 2016.
- [73] Samuele Giannini, Orestis George Ziogos, Antoine Carof, Matthew Ellis, and Jochen Blumberger. Flickering polarons extending over ten nanometres mediate charge transport in high-mobility organic crystals. *Advanced Theory and Simulations*, 3(9):2000093, 2020.
- [74] Samuele Giannini, Antoine Carof, and Jochen Blumberger. Crossover from hopping to band-like charge transport in an organic semiconductor model: Atomistic nonadiabatic molecular dynamics simulation. *The Journal of Physical Chemistry Letters*, 9(11):3116–3123, Jun 2018.
- [75] Orestis George Ziogos, Samuele Giannini, Matthew Ellis, and Jochen Blumberger. Identifying high-mobility tetracene derivatives using a non-adiabatic molecular dynamics approach. *J. Mater. Chem. C*, 8:1054–1064, 2020.
- [76] Fruzsina Gajdos, Siim Valner, Felix Hoffmann, Jacob Spencer, Marian Breuer, Adam Kubas, Michel Dupuis, and Jochen Blumberger. Ultrafast estimation of electronic couplings for electron transfer between π -conjugated organic molecules. *Journal of Chemical Theory and Computation*, 10(10):4653–4660, Oct 2014.
- [77] Adam Kubas, Fruzsina Gajdos, Alexander Heck, Harald Oberhofer, Marcus Elstner, and Jochen Blumberger. Electronic couplings for molecular charge transfer: benchmarking cdft, fodft and fodftb against high-level ab initio calculations. ii. *Phys. Chem. Chem. Phys.*, 17:14342–14354, 2015.
- [78] Biswajit Ray, Aditya G. Baradwaj, Bryan W. Boudouris, and Muhammad A. Alam. Defect characterization in organic semiconductors by forward bias capacitance–voltage (fb-cv) analysis. *The Journal of Physical Chemistry C*, 118(31):17461–17466, Aug 2014.
- [79] W. S. Hu, Y. T. Tao, Y. J. Hsu, D. H. Wei, and Y. S. Wu. Molecular orientation of

- evaporated pentacene films on gold: alignment effect of self-assembled monolayer. *Langmuir*, 21(6):2260–2266, Mar 2005.
- [80] Tatsuo Hasegawa and Jun Takeya. Organic field-effect transistors using single crystals. *Science and Technology of Advanced Materials*, 10(2):024314, 2009.
- [81] John E. Anthony, James S. Brooks, David L. Eaton, and Sean R. Parkin. Functionalized pentacene: improved electronic properties from control of solid-state order. *Journal of the American Chemical Society*, 123(38):9482–9483, Sep 2001.
- [82] John E. Anthony, David L. Eaton, and Sean R. Parkin. A road map to stable, soluble, easily crystallized pentacene derivatives. *Organic Letters*, 4(1):15–18, Jan 2002.
- [83] A. D’Angelo, B. Edgar, A. P. Hurt, and M. D. Antonijević. Physico-chemical characterisation of three-component co-amorphous systems generated by a melt-quench method. *Journal of Thermal Analysis and Calorimetry*, 134(1):381–390, Oct 2018.
- [84] Wanderlā L. Scopel, Antônio J. R. da Silva, and A. Fazzio. Amorphous hfo_2 and $\text{hf}_{1-x}\text{si}_x\text{O}$ via a melt-and-quench scheme using ab initio molecular dynamics. *Phys. Rev. B*, 77:172101, May 2008.
- [85] Seth S. Berbano, Inseok Seo, Christian M. Bischoff, Katherine E. Schuller, and Steve W. Martin. Formation and structure of $\text{na}_2\text{s}+\text{p}_2\text{s}_5$ amorphous materials prepared by melt-quenching and mechanical milling. *Journal of Non-Crystalline Solids*, 358(1):93 – 98, 2012.
- [86] Pranav Karmwar, Kirsten Graeser, Keith C. Gordon, Clare J. Strachan, and Thomas Rades. Investigation of properties and recrystallisation behaviour of amorphous indomethacin samples prepared by different methods. *International Journal of Pharmaceutics*, 417(1):94 – 100, 2011. Advanced characterization techniques.
- [87] Min-Jin Ko, Joel Plawsky, and Meyer Birnboim. Fabrication of cds/ag hybrid quantum dot composites using a melt/quench method. *Journal of Non-Crystalline Solids*, 203:211 – 216, 1996. Optical and Electrical Propertias of Glasses.

- [88] Steve Plimpton. Fast parallel algorithms for short-range molecular dynamics. *Journal of Computational Physics*, 117(1):1 – 19, 1995.
- [89] Steve Plimpton. Lammps software. <http://lammps.sandia.gov>, 1995. [Online; accessed 21-Jan-2021].
- [90] Steve Plimpton, Roy Pollock, and Mark Stevens. Particle-mesh ewald and rRESPA for parallel molecular dynamics simulations. In In Proceedings of the Eighth SIAM Conference on Parallel Processing for Scientific Computing, 1997.
- [91] Christopher I. Bayly, Piotr Cieplak, C, and Peter A. Kollman. A well-behaved electrostatic potential based method using charge restraints for deriving atomic charges: the resp model. *The Journal of Physical Chemistry*, 97(40):10269–10280, Oct 1993.
- [92] M. J. Frisch, G. W. Trucks, H. B. Schlegel, G. E. Scuseria, M. A. Robb, J. R. Cheeseman, G. Scalmani, V. Barone, G. A. Petersson, H. Nakatsuji, X. Li, M. Caricato, A. V. Marenich, J. Bloino, B. G. Janesko, R. Gomperts, B. Mennucci, H. P. Hratchian, J. V. Ortiz, A. F. Izmaylov, J. L. Sonnenberg, D. Williams-Young, F. Ding, F. Lipparini, F. Egidi, J. Goings, B. Peng, A. Petrone, T. Henderson, D. Ranasinghe, V. G. Zakrzewski, J. Gao, N. Rega, G. Zheng, W. Liang, M. Hada, M. Ehara, K. Toyota, R. Fukuda, J. Hasegawa, M. Ishida, T. Nakajima, Y. Honda, O. Kitao, H. Nakai, T. Vreven, K. Throssell, J. A. Montgomery, Jr., J. E. Peralta, F. Ogliaro, M. J. Bearpark, J. J. Heyd, E. N. Brothers, K. N. Kudin, V. N. Staroverov, T. A. Keith, R. Kobayashi, J. Normand, K. Raghavachari, A. P. Rendell, J. C. Burant, S. S. Iyengar, J. Tomasi, M. Cossi, J. M. Millam, M. Klene, C. Adamo, R. Cammi, J. W. Ochterski, R. L. Martin, K. Morokuma, O. Farkas, J. B. Foresman, and D. J. Fox. Gaussian[®]16 Revision C.01, 2016. Gaussian Inc. Wallingford CT.
- [93] Junmei Wang, Romain M. Wolf, James W. Caldwell, Peter A. Kollman, and David A. Case. Development and testing of a general amber force field. *Journal of Computational Chemistry*, 25(9):1157–1174, 2004.

- [94] Makoto Yoneya, Masahiro Kawasaki, and Masahiko Ando. Molecular dynamics simulations of pentacene thin films: The effect of surface on polymorph selection. *J. Mater. Chem.*, 20:10397–10402, 2010.
- [95] Makoto Yoneya, Masahiro Kawasaki, and Masahiko Ando. Are pentacene monolayer and thin-film polymorphs really substrate-induced? a molecular dynamics simulation study. *The Journal of Physical Chemistry C*, 116(1):791–795, Jan 2012.
- [96] Makoto Yoneya. Simulation of crystallization of pentacene and its derivatives from solution. *The Journal of Physical Chemistry C*, Jan 2021.
- [97] Ryan A. Miller, Amanda Larson, and Karsten Pohl. Novel surface diffusion characteristics for a robust pentacene derivative on au(111) surfaces. *Chemical Physics Letters*, 678:28 – 34, 2017.
- [98] Dong Wang, Ling Tang, Mengqiu Long, and Zhigang Shuai. Anisotropic thermal transport in organic molecular crystals from nonequilibrium molecular dynamics simulations. *The Journal of Physical Chemistry C*, 115(13):5940–5946, Apr 2011.
- [99] Florian Steiner, Carl Poelking, Dorota Niedzialek, Denis Andrienko, and Jenny Nelson. Influence of orientation mismatch on charge transport across grain boundaries in tri-isopropylsilylethynyl (tips) pentacene thin films. *Phys. Chem. Chem. Phys.*, 19:10854–10862, 2017.
- [100] Ida Bagus Hendra Prastiawan, Jingxiang Xu, Yusuke Ootani, Yuji Higuchi, Nobuki Ozawa, Shingo Maruyama, Yuji Matsumoto, and Momoji Kubo. Molecular interactions between pentacene and imidazolium ionic liquids: A molecular dynamics study. *Chemistry Letters*, 47(9):1154–1157, 2018.
- [101] EPA DSSTox. Epa dsstox. <https://comptox.epa.gov/dashboard/DTXSID7059648>, 2021. [Online; accessed 25-Jan-2021].
- [102] Stefan Schiefer, Martin Huth, Alexander Dobrinevski, and Bert Nickel. Determination of the crystal structure of substrate-induced pentacene polymorphs

- in fiber structured thin films. *Journal of the American Chemical Society*, 129(34):10316–10317, Aug 2007.
- [103] Martin Ester, Hans-Peter Kriegel, Jörg Sander, and Xiaowei Xu. A density-based algorithm for discovering clusters in large spatial databases with noise. pages 226–231. AAAI Press, 1996.